Photo-physical Properties of Lead-Tin Binary Perovskite Thin Films

By

Floyd Lionel Mabiala

Dissertation submitted in fulfilment of the requirements for the degree of

Magister Scientiae

In the Department of Physics and Astronomy, University of the Western Cape

March 2021

Supervisors:

Prof Christopher J. Arendse, Department of Physics, University of the Western Cape

Prof. Malik Maaza, Materials Research Department, iThemba LABS-NRF

Co-supervisor:

Dr. Lebogang Kotsedi, Materials Research Department, iThemba LABS-NRF

ABSTRACT:

Organic-inorganic lead-based perovskite has exhibited great performance in the past few years. However, the lead (Pb) embedded in those compounds is a significant drawback to further progress, due to its environmental toxicity. As an alternative, tin (Sn) based-perovskites have demonstrated promising results in terms of electrical and optical properties for photovoltaic devices, but the oxidation of tin ion- from stannous ion (Sn^{2+}) to stannic ion (Sn^{4+}) presents a problem in terms of performance and stability when exposed to ambient conditions. A more feasible approach may be in a Pb-Sn binary metal perovskite in pursuit of efficient, stable perovskite solar cells (PSCs) with reduced Pb-content, as compared to pure Pb- or Sn-based PSCs. Here, we report on the deposition of a Pb-Sn binary perovskite by sequential chemical vapor deposition. Firstly, the binary metal iodide $Pb_{(1-x)}Sn_xI_2$ was annealed at the eutectic temperature (220 ºC) that was obtained from real-time RBS. Secondly, the perovskite $CH_3NH_3Pb_{1-x}Sn_xI_3$ film was converted at 190 ºC after the reaction of $Pb_{(1-x)}Sn_xI_2$ with CH_3NH_3I under N_2. X-ray diffraction revealed new diffraction peaks characteristic of Pb-Sn binary perovskite, EDS microscopy confirmed the chemical composition of the material, and UV-VIS spectroscopy was used to probe optical properties of the material which demonstrated that the addition of Sn nanoparticles in Pb-based perovskite reduces the optical bandgap.

KEYWORDS:

Organic-inorganic perovskite, Pb/Sn-based PSC, Binary metal Alloy, Chemical vapour deposition (CVD), RBS-analysis, X-ray diffraction (XRD), UV-VIS spectroscopy.

DECLARATION:

I, the undersigned, hereby declare that the work contained in this Master thesis is my original work, that it has not been previously submitted for any degree or examination in any other university, and that all the sources I have used or quoted have been indicated and acknowledged by complete references.

Floyd Lionel MABIALA

Signature: …… 

Date: …03/11/2020

I Know the Price of Success: Hard Work, Dedication, and an Unremitting Devotion to the Things You Want to See Happen—

Unknown.

ACKNOWLEDGEMENTS:

Je voudrai remercier le tres Haut, la force Transcendante, pour m'avoir eclaire, me donner la force, le courage et la sagesse pour accomplir ce chemin du succes qui m'est reserve.

I would also like to thank the following people and organisations without whose assistance and guidance, this thesis would not have been possible.

My supervisors Prof. Malik Maaza, Prof. Christopher Arendse, and Dr. Lebogang Kotsedi for their help, support, encouragement, and availability during my study.

NRF is acknowledged for its financial support as well as the MaNus-MatSci program.

To all my friends and colleagues, both at iThemba and at UWC (especially Dr. Chris Mtshali, Dr. Remy Bucher, Dr. Aline Simo, Dr. Juliet Sacky, Dr. Saleh Khamlich, Jadvy Kouka, Boitumelo Mabakachaba, Steven Magogodi, and Dr. Ninon Etsassala) who have helped me, supported me and encouraged me through this. Thank you so much.

I am thankful to the UWC Division for Postgraduate Studies (DPGS) with the help of Alechine Emmanuel Ameh as a writing coach.

Stephen Klue, Lionel Furie, Siphesihle Magubane, and Dr. Siphelo Ngqoloda for their help in the deposition of the perovskite films.

A special thanks to all the staff and students of iThemba at large and MRD in particular, for their support.

I am grateful to my parents; my two dear Moms Odette Ngounou and Jeanne Moungouya for their prayer, my two Dads Maurice Boukete and Hilaire Mabiala, and to all my siblings for their support.

To my partner Pozisa Lucia Manisi and my big boy Nkosinathi Lionel Mabiala, for the trust and understanding.

TABLE OF CONTENTS

TABLE OF FIGURES

CHAPTER 1

INTRODUCTION

1.1 ENVIRONMENTAL IMPACT OF CURRENT ENERGY SYSTEMS

Burning of fossil fuels such as coal and diesel, for power generation, has been identified as the major contributors to climate change, due to their emission of greenhouse gases. The effects of climate change have proven to have catastrophic effect on the earth's ecosystem (National Planning Commission, 2010; Reinman, 2012; UNFCCC, Paris agreement 2015). According to the US Energy Information Administration (EIA), in 2016 an approximation of 65% of the global power was generated from fossil fuels, and about 20% was from nuclear energy, while only 15% was from renewable energy sources (EIA, 2019.). With a growing population, these numbers are expected to escalate dramatically as the demand for energy increases, meaning more and more greenhouse gases will be discharged to the atmosphere. Figure 1.1 illustrates the world's fuel shares of global total primary energy supply (TPES), electricity generation, total final consumption, and resulting CO_2 emissions (Dincer and Acar, 2015).

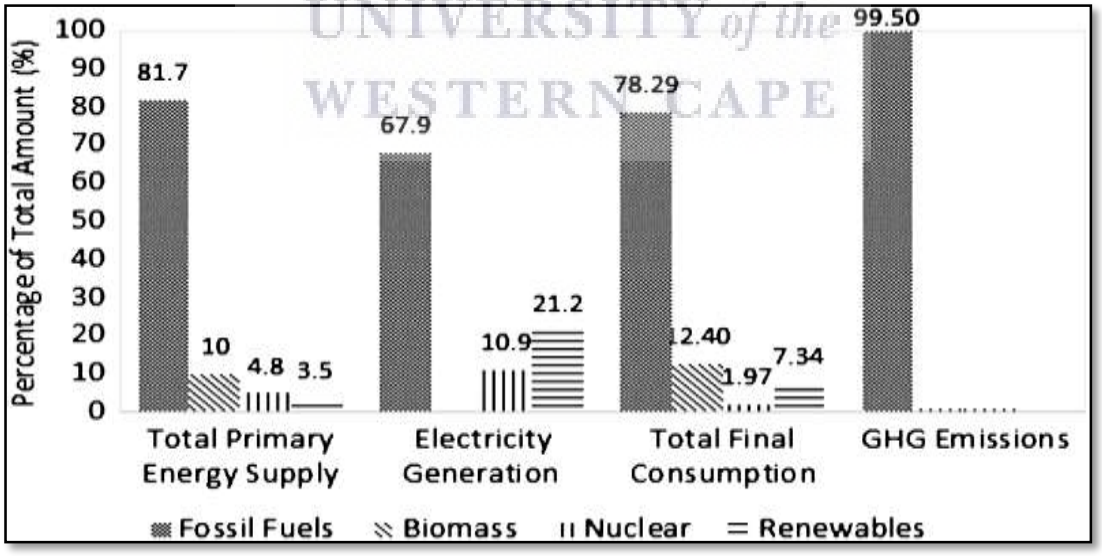

Figure 1.1: Fuel shares of global total primary energy supply, electricity generation, total final consumption, and greenhouse gasses (GHG) emissions (Dincer and Acar, 2015.).

Additionally, 81.7% of the global TPES, 67.9% of global electricity generation, and 78.29% of global total final consumption were met by fossil fuels. However, fossil fuels have limited nature; they are not expected to keep up with the increase in energy demand (Dincer and Acar, 2015). Also, fossil fuel reserves are decreasing due to huge consumption, and the prices are expected to increase because of the unavailability and political uncertainties of the countries holding the worlds' fossil fuel supplies. Greenhouse gasses (mainly CO_2) (Dincer and Acar, 2015) emissions as a result of fossil fuel burning and their negative impact on the environment and human health have been raising serious concerns (Fig 1.1 shows 99.5% of global GHG emissions caused by fossil fuels) (Jakob et al., 2015). In South Africa for instance, the production of energy is still dominated by the burning of coal (Fig 1.2). Wright et al. reported that the electricity system relies heavily on coal, and in 2016 coal accounted for 74% of total electricity capacity compared to hydro, nuclear, and renewables (Centre for Environmental Rights, 2017). Hence, there is a need to lower the use of fossil fuel to manage the economic crisis as well as the impacts on the climate.

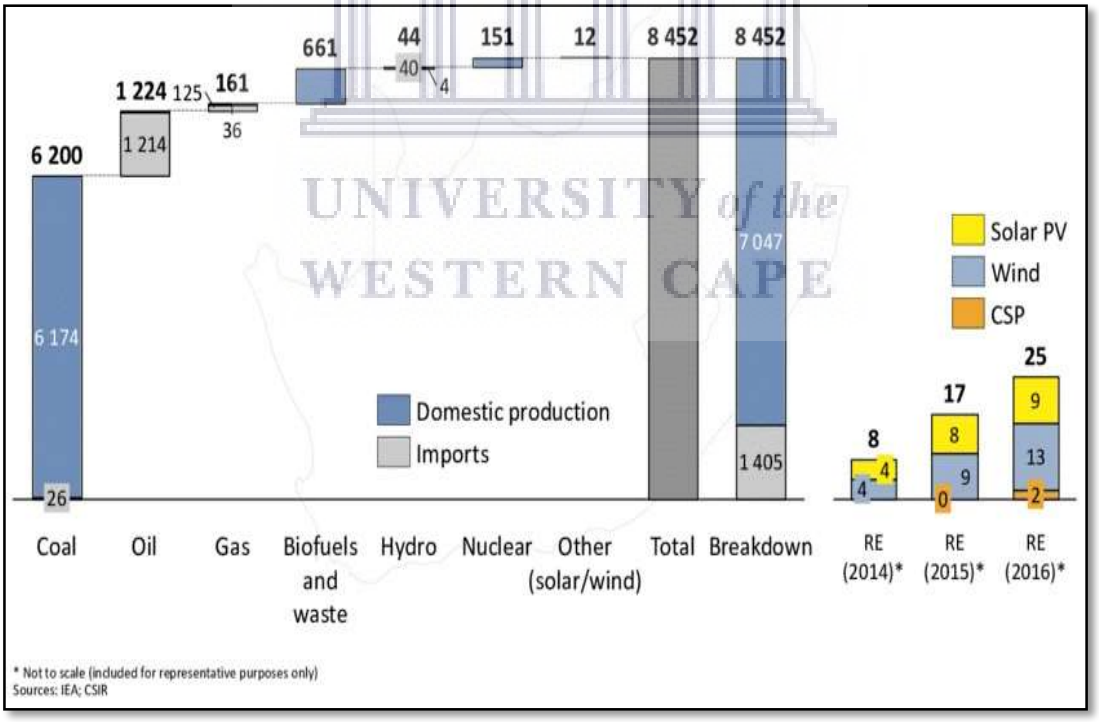

Figure 1.2: Primary energy supply in South Africa (2014) showing showing significant reliance on coal as a primary energy supplier (Centre for Environmental Rights, 2017).

This chapter will describe the need for a transition from fossil fuels to a clean energy source and succinctly present the limitations of semiconductor materials used to convert sunlight into electrical power. Also, it will highlight the importance of improving the new semiconductor absorber material, that is, perovskite, for its significant potential. Finally, it will describe the aim and objectives of the study, which will subsequently be followed by a brief outline of the remainder of the thesis chapters.

1.2 THE NEED FOR CLEAN ENERGY

There are several alternative sources of energy production that does not emit greenhouse gases. Among the alternatives source of energy, there are geothermal, wind, hydropower, and solar energy. Since the sun is one of the most abundant renewable energy resources, providing 1.5×10^{18} kW h years' worth of energy, and by comparison, the known reserves of oil, coal, and gas are 1.75×10^{15} kW h, 1.4×10^{15} kW h, and 5.5×10^{15} kW h, respectively (Sum et al., 2014). Thus, a year's worth of sunlight provides more than a hundred times the energy of the world's entire known fossil fuel reserves (Sum et al., 2014). Hence, it will be interesting to use solar energy as an energy source in various systems such as the production of hydrogen fuel from water-splitting technology, the generation of heat from solar thermal systems, or by directly generating electric power via the use of photovoltaic cells or solar cells. The solar cells will absorb photons directly from the sunlight and convert them into electricity (Becquerel E. 1839). Considering that, it may be concluded that solar energy could play a major role in changing the design of our modern energy system by producing cheaper, renewable, and reliable electric power. These solar cells can be fabricated on flexible materials, this can be achieved using various techniques.

1.3 SOLAR ENERGY

Solar energy can be harnessed using either solar cell devices, concentrated solar power CSP (for solar heating), or artificial photosynthesis to generate thermal heat or electricity ("Becquerel E. 1839.). A solar cell is described as a device that converts photons into electricity by the principle of photovoltaic effect. The photovoltaic effect can take place in solid, liquid, or gaseous materials (Becquerel E. 1839; Chapin et al., 1954; Verlag et al., 2016). For instance, in the liquid phase, water (H_2O) is split into hydrogen (H_2) and oxygen (O_2) by the absorption of photons. Then hydrogen and oxygen gases are collected separately by a membrane. On the

contrary in a solid-state material—see fig 1.3 a), there is a charge separation, when photons are absorbed by the material, resulting in electrons-hole pair generation (Verlag et al., 2016). Nevertheless, the efficient conversion of sunlight into electricity is proven to be effective in solids state such as semiconductor materials. Hence solid-state solar cells are of interest in this research study.

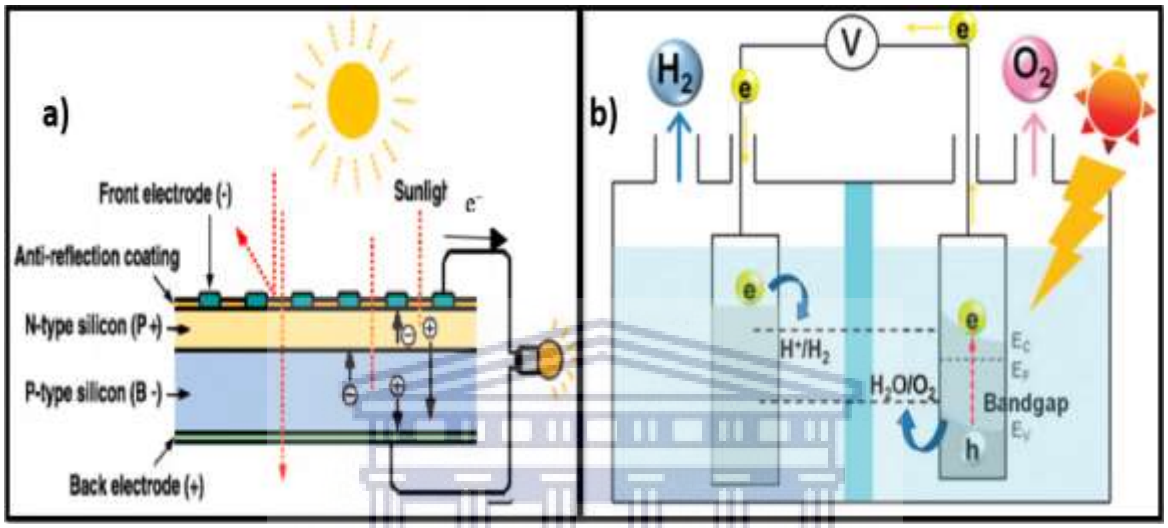

Figure 1.3**:** Working principle of a) semiconductors PN junction—type Si, b) water splitting (Carlos D Gallegos et al, 2015; Yang et al., 2015).

1.4 PHOTOVOLTAIC MATERIALS

There are several types of photovoltaic cells with silicon-based being a well-known one. Silicon-based cells are currently the most efficient on the market (Kanda et al., 2018) and are heavily used in residences and commercial buildings. They account for more than 80 % of all the solar panels sold around the world (Imamzai et al., 2011). There are different types of silicon-based cells such as (i) single crystal Silicon Cells: the most popular and efficient cells made from micrometre thin wafers of silicon. Relative to the other types of silicon-based solar cells, they have higher efficiency (up to 24.2%) (Imamzai et al., 2011). However, growing high purity single crystal silicon is difficult, and energy-intensive process, which makes their manufacturing cost expensive. (ii) Polycrystalline silicon solar cells are made from polycrystalline silicon, instead of a single crystal, see fig 1.3 a), but they are slightly less efficient (19.3%.) as compared to the single crystal. (iii) Amorphous silicon cells are usually fabricated from hydrogenated amorphous silicon (Imamzai et al., 2011).

Unlike the crystalline solar cells, a very thin layer of hydrogenated amorphous silicon is deposited onto a backing substrate such as metal, glass, or even plastic. They are usually utilized in calculators and many small electronic devices due to their low efficiency which can be up to 10%, this is due to many defects in the material. Generally, silicon-based solar cells are longer lasting than non-silicon-based cells and operate in the PN junction system. However, the processing technique is expensive and the cells are more at risk to lose some of their efficiency at higher temperatures (hot sunny days) (Imamzai et al., 2011; Kanda et al., 2018; Meier et al., 2004). Different families of material have been used for multi-junction cell fabrication such as the germanium/ GaAs / InGaP. They provide a large spectrum of available bandgaps covering the sun spectrum which allows high performances (up to 41.6%) (Almosni et al., 2018). Nevertheless, there are some limitations, such as the requirement of current matching, meaning that the current produced is too high per unit cell area, as the germanium bandgap is small, and the cell generates a current almost twice the size of the limiting sub-cell current. And the materials' high cost prevents the application of solar cells as flat panels (Almosni et al., 2018). The other class of solar cells are cadmium sulfide/telluride (CdS/Te) (Rimmaudo et al., 2017) and copper indium gallium di-selenide (CIGS), they also form part of semiconductor (second generation: thin films), yet the large scale application of CdS/Te solar cells, is not very attractive as cadmium is highly toxic. While Indium and gallium are rare and expensive, the use of abundant materials such as the combination of copper, zinc, tin, and sulfur to form CZTS is being explored (Foster et al., 2009; Rimmaudo et al., 2017). Another type of semiconductor material used in photovoltaic cells is called third-generation materials, comprising of organic solar cells (OSCs), dye-sensitized (DSS); quantum dot-sensitized (QDs), and perovskite (Luo and Daoud, 2015). They all operate in a multi-junction/ heterojunction system and the production of this type of photovoltaic materials can be done at a relatively cheap cost, because of their easy processing techniques and they are abundant on earth (Mingsukang et al., 2017).

Organic solar cells (OSCs) use organic materials to absorb light from the sun. Since the development of the bulk heterojunction concept—see fig 1.4 a), the common acceptor materials in OSC devices are fullerenes and their derivatives (Mingsukang et al., 2017). They have been used to improve the absorption coefficient and the open-circuit voltage. A High efficiency, up to 11.7-13% has been reached including with non-fullerene acceptor. However, these materials present drawbacks such as poor absorption in the visible range, energy losses (Scharber et al., 2016), solvent toxicity, and the instability induced in the bulk heterojunction (Bertho et al.,

2008). Besides, most attempts to the replacement of these solvents come at the cost of efficiency (Almosni et al., 2018). Dye-sensitized solar cells (DSSCs) on the other hand, employ oxide semiconductors with wide band gaps and sensitizers that absorb electromagnetic (EM) waves in the visible light—see fig 1.4 b). The dye molecules are bound to TiO_2 (mesoporous), and the porous network is then infiltrated by either an electrolyte or a conducting polymer. But the performance of the cell is still poor and mainly dependent on a dye used as a liquid sensitizer (Scharber et al., 2016). Similarly, quantum dot sensitized solar cells (QDSSCs) such as Pb-based QD heterojunction, are typically formed by depositing the PbS/PbSe QD layer on top of the flat ZnO layer.

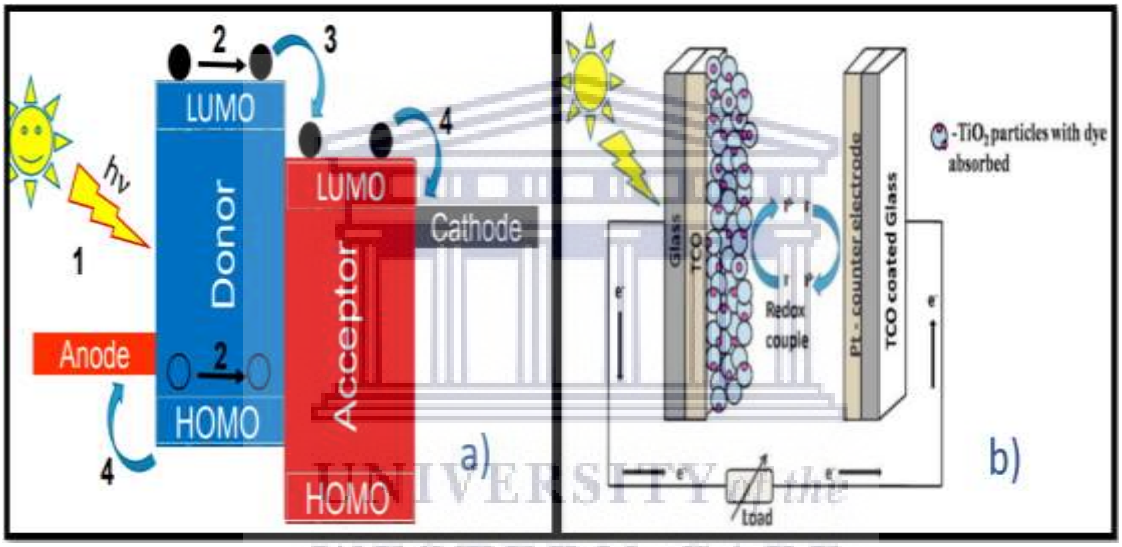

Figure 1.4**:** Working principle of a) Organic heterojunction cells—polymers: number from 2-4 is the movement of electrons, b) Dye-sensitized cells(Gopi et al., 2015; Yang et al., 2015).

They are nano-dimensional structures with a narrow bandgap suitable to excite electrons to the conduction band. But the recombination process of electron-hole pairs in the electrolyte is disadvantageous to the performance. And the solid-state electrolytes also suffer from low ionic conductivity (Mathew et al., 2014; Meier et al. 2004; Mingsukang et al., 2017; Yoon et al., 2013). Interestingly, perovskite is the newly emerged efficient photovoltaic material. It is composed of rare earth, alkaline earth, alkali, and all compounds that crystallize in the same structure as $CaTiO_3$. These semiconductor materials have attracted intense interest in many applied and fundamental areas of solid-state chemistry, physics, advanced materials light-emitting diodes (LEDs), and others (Tejuca and Fierro, 1992). One of the advantages is due to

their flexibility and the significant tolerance in their partial substitution and non-stoichiometry while still maintaining the perovskite structure. Most importantly they have the potential of using non-scarce and non-toxic elements. That's why they have become prospective candidates for the next generation of low cost and flexible solar cells (Jung and Park, 2015; Saliba et al., 2018; Tejuca and Fierro, 1992; Wong et al., 2019; Yang et al., 2015; Yun et al., 2019). Hence, they have the capability of changing the energy system into a more sustainable one.

1.4.1 THE EVOLUTION OF PEROVSKITE

The evolution record of power conversion efficiencies (PCE) of solar cells is illustrated on the graph published regularly by the National Renewable Energy Laboratory (NREL) (focus mainly on the third generation materials) (National Renewable Energy Laboratory, 2017). It clearly shows how in a very short period the organic lead (Pb) perovskite solar cells have made an incredibly strong climb in terms of power conversion efficiency (Fig1.5).

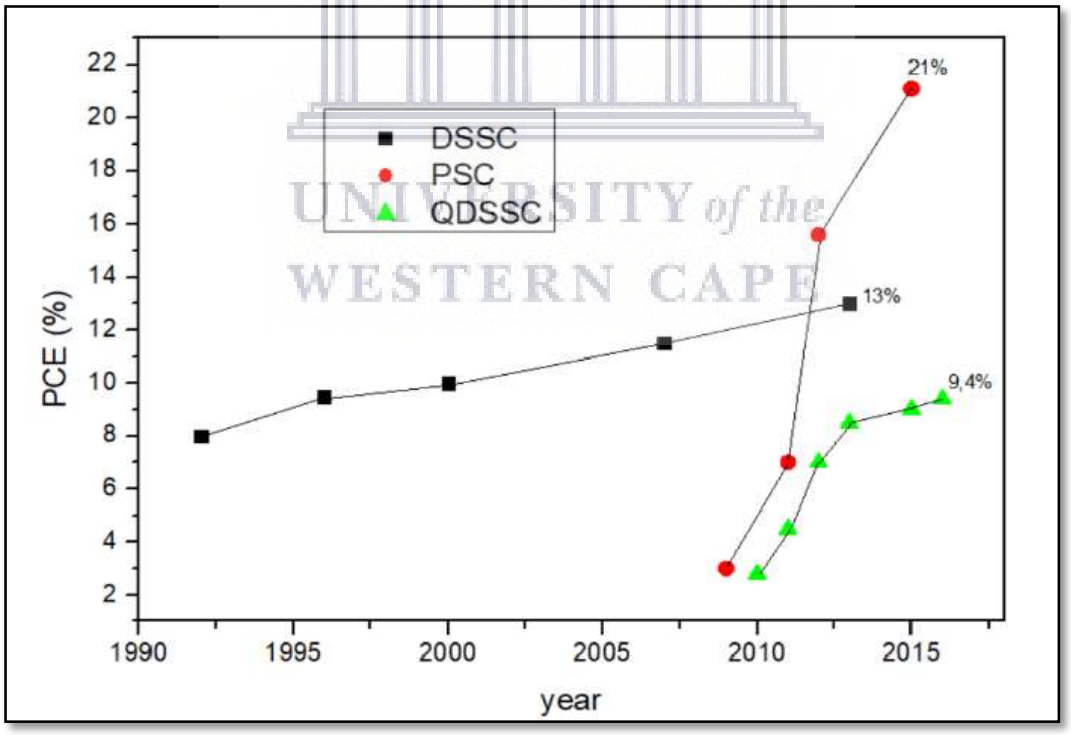

Figure 1.5**:** Graphs showing the progress of third-generation photovoltaics, NREL (National Renewable Energy Laboratory 2017; Gong et al., 2017)

The organic lead halide perovskite, studied as a light absorber for the first time in 2009 by Kojima and the power conversion efficiency of the perovskite cell reported was about 3.8% (National Renewable Energy Laboratory, 2017). Since then, multiple improvements have been conducted by researchers and the efficiency has kept on increasing until it reached 21% of power conversion efficiency in 2015 (Yang et al., 2015). Dye-sensitized solar cells (DSSC) however, have been known since the seventies but only around 1991, the period of its breakthrough as it is shown on the graph, which attracted the attention of solar cell researchers (Kim et al., 2013; Mingsukang et al., 2017). Despite the enhancement of the dye-sensitized, the power conversion efficiency of perovskite has slowly increased over the years. And after twenty-five years, the efficiency of DSSC has not yet exceeded 15% (Gong et al., 2017). On the other hand, quantum dots solar cells (QDSSC) (aimed to replace the dye-sensitized) had displayed good optical properties. But, despite some improvements recorded lately in 2009 (Chuang et al., 2014; Kim et al., 2013; Yang et al., 2015), the highest efficiency of QDSSC) reported is around 12% (Yuan et al., 2016). In comparison to these three materials, it could be understood why perovskite material has drawn so much attention over other materials such as DSSC and QDSSC (Yang et al., 2015).

Although organic lead (Pb) perovskite was unknown in the photovoltaic community a few years ago, it has now captivated attention as the best suitable semiconductor materials for the future of photovoltaics (Vidyasagar et al., 2018). This is due to its magnificent performance which is attributed to the outstanding intrinsic photovoltaic properties such as high absorption coefficient, long electron, and hole diffusion lengths, tunable bandgap, extended charge carrier lifetime, high open-circuit voltages which can reach up to 1.2V as well as low-cost fabrication (Abate, 2017; Pérez-del-Rey et al., 2016; Vidyasagar et al., 2018).

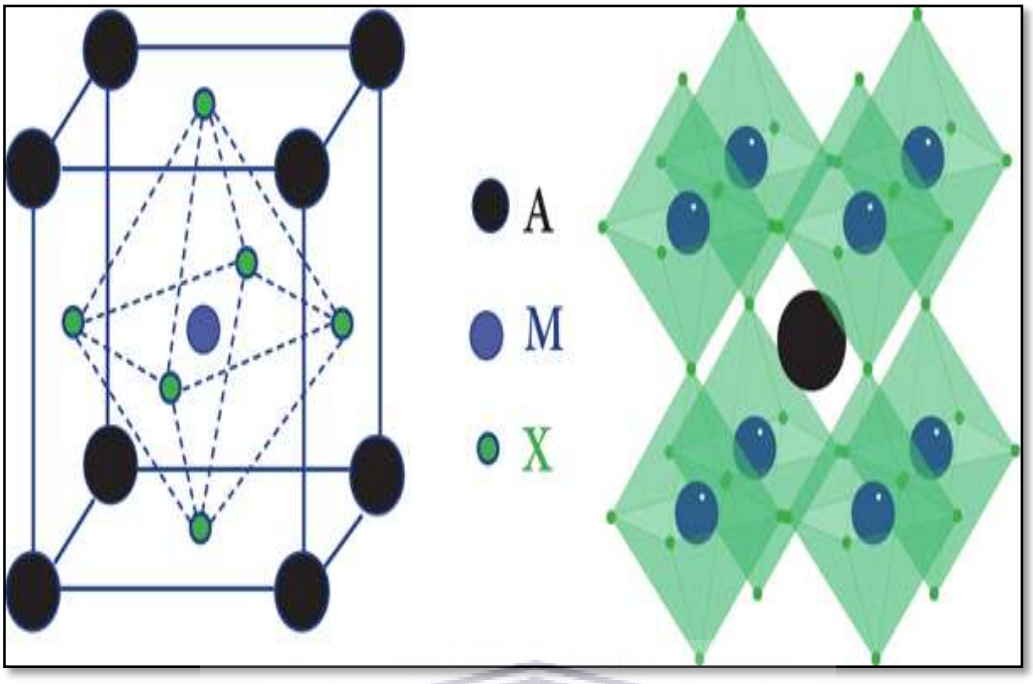

Figure 1.6**:** Unit-cell of an organic-inorganic perovskite structure (Yun et al., 2019).

It is worth It is worth noting that the name perovskite was first given to the mineral calcium titanate ($CaTiO_3$) in 1839 and thereafter to all compounds that carry the general chemical formula of $CaTiO_3$ (Pérez-del-Rey et al., 2016). Most perovskites of interest as a light absorber for photovoltaic applications are halide perovskites and have monovalent and divalent cations, though the main perovskite $CaTiO_3$, is a type of oxide and has divalent and tetravalent cations. Nevertheless, the organic lead perovskite (OLP) compounds based on metal halides adopt the structure of AMX_3 perovskite which has a simple cubic crystal structure at room temperature as shown in Figure 1.4. This structure consists of a network of corner-sharing MX_6 octahedral with an M–X–M bond angle of 180 ºC and ions in the interstices, where:

- A is a monovalent cation selected to balance the total charge, in most cases an organic molecule is used such as methyl-ammonium (MA) $CH_3NH_3^+$ or formamidinium (FA) $HC(NH_2)_2^+$.
- M is a metallic divalent cation and usually Pb^{2+} or Sn^{2+}
- X is a site occupied by a halogen anion either iodine (I^-), chloride (Cl^-), or Bromide (Br^-) is used; and these atoms are often mixed to tune the bandgap (Abate, 2017).

In general, organic lead (Pb) perovskite might be in orthorhombic phases by distortion of the MX_6 octahedral at lower temperatures. The transition from orthorhombic to tetragonal to cubic perovskite structures was also found to be a function of temperature. The organic lead

perovskites with mixed A cation and/or mixed halide composition are frequently used to manipulate the properties of the material. Moreover, methyl-ammonium lead halide perovskite can be produced either by a solution process or by vacuum deposition (Chuang et al., 2014; Vidyasagar et al., 2018; Yuan et al., 2016). Also, different techniques are used to control the morphology of the perovskite film (Abate, 2017; Vidyasagar et al., 2018).

1.4.2 WORKING PRINCIPLE OF PEROVSKITE LEAD (Pb) IODIDE

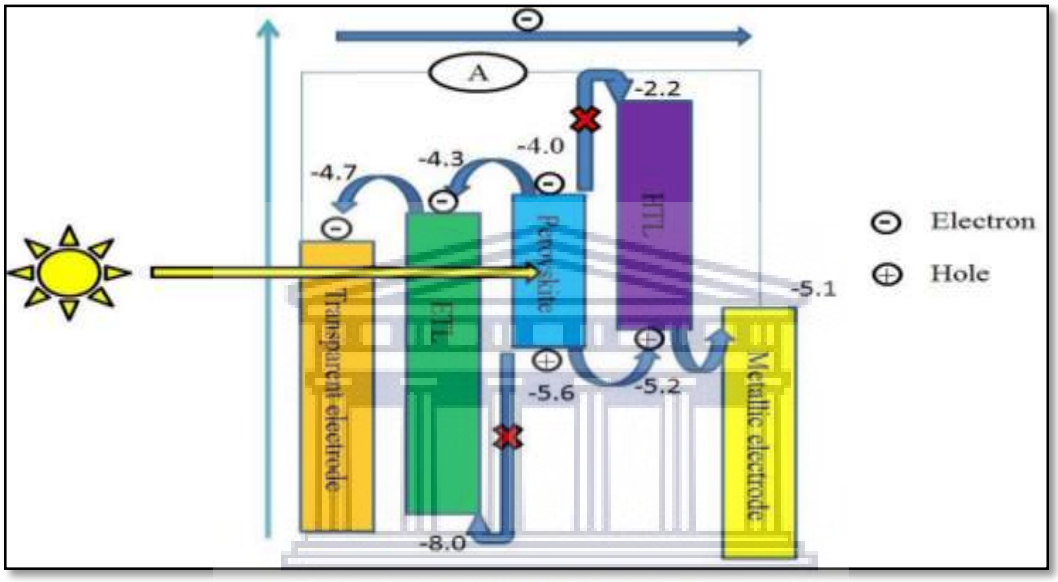

Figure 1.7: Schematic energy band diagram of perovskite solar cells. The blue arrow represents the energy. The lowest value for each layer is the energy at HOMO and the highest value is the energy at LUMO. The blue arrows show the charge carriers move, arrows with a cross are a blocked path (Park, 2014).

First, photons First, photons from a light source, shown as a sun (yellow arrow Fig 1.7), pass through the glass and the transparent electrode (FTO) to the perovskite layer. The photon is absorbed in the active perovskite layer and excites an exciton if the energy of the photon is greater than the perovskite energy gap. Then the exciton is separated to free charge carriers due to the internal potential created from the work function difference between the two electrodes (transparent and metallic), see fig 1.7. While the electrons are transported by the electron-transfer layer (ETL), the holes are transported by the hole transfer layer (HTL). From there, Electrons are collected at the electrode and the hole at the metallic electrode (Au, Al). Then, the electron passes through the wire that links the two electrodes, and the moving electrons generate a current. The electron and the hole recombine in the metallic electrode. However, the

energy levels of each layer have to be carefully planned for the proper functioning of PSC, because the excited electrons and holes must recombine so the overall energy is minimized (Park, 2014). Thus, the right layer structure will block some recombination in the cell by allowing charge carriers to take another route. This is achieved by making the LUMO ETLs a little lower than the active LUMO layer, which gives the electron a more desirable path. The same applies to the HTLs HOMO which must be a little bit higher than the active HOMO layers, which gives holes a much more desirable way. It is the same for each layer in the cell, each of which has higher and lower HOMOs for the transport chain of charge carriers, as seen in figure 1.7 above (Park, 2014).

1.5 PROBLEM STATEMENT AND MOTIVATION

Despite the significant improvements of perovskite solar cell in terms of efficiency, the organic lead perovskite suffers from some limitations such as hysteresis in I–V curves, and cells instability (Imamzai et al., 2011; Pérez-del-Rey et al., 2016; Vidyasagar et al., 2018), which originate not only from perovskite compound but also from different components of the cell such as the hole and the electron transport layers, top and bottom contacts as well as the architecture of the cell (Imamzai et al., 2011; Meier et al., 2004). The instability also causes a fast degradation in normal atmospheric conditions due to their sensitivity to moisture and high-temperature environments. The eco-toxicity due to the presence of the soluble lead element in the molecule is the major issue facing the organic lead perovskite.

At present, one of the major challenges of perovskite solar cells is its eco-toxicity. Lead (Pb) (contains in perovskite) is an extremely toxic heavy metal that disturbs various plant physiological processes and unlike other metals, such as tin, zinc, copper, and manganese, which does not play any biological functions. Pb is a drawback for further progress of organic lead perovskite because it is a threat to the environment (Luo and Daoud, 2015). For example, it is observed that the cells in contact with moisture degrade, and that degradation could contaminate the atmosphere and pollute the field, leading to eco-toxicological problems (Abate, 2017). It is, therefore, necessary to develop a sustainable perovskite compound using an abundant metal which is less expensive, environmentally friendly (less toxic) as well as ensuring good optical functions. Hence the suitable element capable of substituting lead tested among others so far has been tin (Sn). As a result of incorporating tin (Sn) for the replacement of lead (Pb), is being successfully carried out by researchers because of several reasons: tin

(Sn) happens to be the convenient divalent metal cation and has similar ionic radii (Sn^{2+} 1.35Å and Pb^{2+} 1.49Å) (Zuo et al., 2014). This ionic radius is proven to have a small perturbation in the lattice. Therefore, it does not affect the hexagonal structure when bound with iodine**.** It also belongs to the same group (IV) as lead and demonstrates high charge mobility as well as a narrow bandgap when compared to lead. However, the oxidation of tin ion—from stannous ion (Sn^{2+}) to stannic ion (Sn^{4+}) occurs when it is exposed to high temperature, resulting in poor performance and instability which limits the lifetime of a cell (Luo and Daoud, 2015b; Tavakoli et al., 2018; Yoon et al., 2013). Consequently, a more feasible approach may be in a Pb-Sn binary metal alloy perovskite, in pursuit of efficient and stable perovskite solar cells (PSCs) with reduced Pb-content, as compared to pure Pb or pure Sn-based PSCs (Tavakoli et al., 2018).

This study utilized the vapour deposition technique, it is appropriate to produce large-area thin-film devices with good uniformity and it does not require solvents. Additionally, the vapour deposition method is cost-effective because it uses less material. Hence, it is convenient for the large-scale production and possibly commercialization of perovskite solar cells.

1.6 AIM AND OBJECTIVES

The research describes in this thesis introduces the perovskite material as a semiconductor for solar cell applications. Furthermore, the aim is to minimize lead content in perovskite—$CH_3NH_3Pb_{1-x}Sn_xI_3$ compound, this will be achieved as follows.

From the precursor PbI_2, a thin film of pure Sn will be added to form a lead-tin binary iodide alloy—$Pb_{1-x}Sn_xI_2$, while incrementally reducing lead. Moreover, the photovoltaic response such as absorption spectrum, bandgap will be studied.

The objective is to synthesize the Pb-Sn binary alloy thin film:

- Using both PbI_2 and Sn powder.
- CVD will be used to deposit lead iodide powder, and thermal evaporation technique for the deposition of tin powder. The films thickness was obtained using a profilometer.
- Real-time RBS will be employed to measure the eutectic temperature of the mixing (PbI + Sn)—element, their migration, the mixing time, and the composition of the film.
- Annealing of the obtained film for the total mixing of Pb + Sn
- Studying the microstructural and optical response of the obtained alloy using RBS, X-ray diffraction, EDX spectroscopy and UV-visible technique.
- Evaporating methyl-ammonium iodide **(**CH_3NH_3I) to form a complete perovskite layer.

- Determining film morphology and chemical composition using the scanning electron-microscopy and EDS.
- Evaluating the photo-response of the obtained perovskite film through the measurement of absorbance capability, calculation of the energy bandgap and the assessment of lattice structure using the UV-vis technique, photometer, and X-ray diffractometer.

1.7 THESIS OUTLINE

In chapter 2, an overview of the literature on perovskite material is given as well as more details regarding the physical properties of the material such as electronic, electrical, and optical and its chemical properties are emphasized.

Chapter 3 focuses on the methods of growth used for the metal alloy iodide and methyl-ammonium halide, followed by a description of CVD and thermal evaporation process.

Chapter 4 focuses on the discussion of all the experimental results obtained in comparison with the reported data.

Chapter 5 contains a summary/general conclusion of the work presented in this project and how they align with the objectives, as well as the outlook for future work.

1.8 REFERENCES

Abate, A., 2017. Joule 1, 659-664.

Almosni, S., Delamarre A., Jehl Z. 2018 Material challenges for solar cells in the twenty-first century: directions in emerging technologies Taylor Fr.

Bertho, S., Janssen, G., Cleij, T.,2008. Sol. Energy Mater. & Sol. Cells 92, 753-760

Becquerel E. 1841, Recherches sur les effets de la radiation Comptes Rendus Acad Sci. 1839;9:145–149.

Centre for Environmental Rights (CER), 2017. Csir.

Chapin, D.M., Fuller, C.S., Pearson, G.L., 1954. J. Appl. Phys. 25, 676.

Chuang, C.H.M., Brown, P.R., Bulović, V., Bawendi, M.G., 2014. Nat. Mater. 13, 796-801.

Carlos R. D. Gallegos, Manuel Alvarez S. A2015. Int. J. Comput. Appl. 127, 26-33.

Dincer, I., Acar, C., 2015. Int. J. Energy Res. 39, 585-606.

Foster, R., Ghassemi, M., Cota, A., Book 2009. SOLAR ENERGY Renewable Energy and the Environment.

Gong, J., Sumathy, K., Qiao, Q. et al, 2017. Renewable and Sustainable Energy Reviews 638, 234-246.

Gopi C., M Venkata-Haritha, Soo-Kyoung Kim, and Hee-Je Kim 2015. Dalton Trans. 44, 630-638.

Imamzai, M., Aghaei, M., Thayoob, Y.H., 2011. Proc. Natl. Grad. Conf. 2012, 8–10.

<https://www.iea.org/reports/global-energy-review> (accessed 2.28.20).

Jakob, M., 2015. Nature 517, 150-152

Jung, H.S., Park, N.G., 2015. Small 11, 10-25.

Kanda, H., Shibayama, N., Uzum, A., 2018. Materials Today Energy 7, 190-198

Kim, H.S., Lee, J.W., Yantara, N., Boix, P.P., Kulkarni, S.A., Mhaisalkar, S., Grätzel, M.,

Park, N.G., 2013. Nano Lett. 13, 2412-2417.

Luo, S., Daoud, W.A., 2015a. J. Mater. Chem. A Mater. Energy Sustain. 3, 8992-9010.

Luo, S., Daoud, W.A., 2015b. J. Mater. Chem. A Mater. Energy Sustain. 3, 8992-9010.

Mathew, S., Yella, A., Gao, P., Humphry-Baker, R., E Curchod, B.F., Ashari-Astani, N., Tavernelli, I., Rothlisberger, U., Khaja Nazeeruddin, M., Grätzel, M., 2014. Nat. Chem. 6, 242-247.

Meier, J., Spitznagel, J., Kroll, U., Bucher, C., 2004. Thin Solid Films 451-452, 518-524.

Mingsukang, M.A., Buraidah, M.H., Arof, A.K., 2017. Third-Generation-Sensitized Solar Cells, in: Nanostructured Solar Cells. InTech.

National Development Plan (2030) Dep. Presedency Repub. South Africa 70, 2011, ISBN 978-0-621-40475-3 RP270/2011.

Pérez-del-Rey, D., Forgács, D., Hutter, E.M., Savenije, T.J., Nordlund, D., Schulz, P., Berry, J.J., Sessolo, M., Bolink, H.J., 2016. Adv. Mater. 28, 9839-9845.

Michael Grätzel, 2003. Journal of Photochemistry and Photobiology C: Photochemistry Reviews 4, 145-153.

Rimmaudo, I., Salavei, A., Artegiani, E., Menossi, D., Giarola, M., Mariotto, G., Gasparotto, A., Romeo, A., 2017. Sol. Energy Mater. Sol. Cells 162, 127-133.

Saliba, M., Correa-Baena, J.P., Grätzel, M., Hagfeldt, A., Abate, A., 2018. Perovskite Solar Cells: From the Atomic Level to Film Quality and Device Performance. Angew. Chemie - Int. Ed.

Scharber, M.C., 2016. Adv. Mater. 28, 1994-2001.

Sum, T., Nripan Mathews , 2014. Energy Environ. Sci., 2014,7, 2518-2534.

Tavakoli, M.M., Zakeeruddin, S.M., Grätzel, M., Fan, Z., 2018. Adv. Mater. 30, 1–9.

Tejuca, L., Fierro, J., 1992. Properties and applications of perovskite-type oxides.

https://www.eia.gov/energyexplained/us-energy-facts/ (accessed 2.28.20).

https://unfccc.int/process-and-meetings/the-paris-agreement/the-parisagreement/key-aspects-of-the-paris-agreement (accessed 2.28.20).

Verlag GmbH, W., KGaA, C., 2016. Physics of Solar Cells From Principles to New Concepts.

Vidyasagar, C.C., Muñoz Flores, B.M., Jiménez Pérez, V.M., 2018. Recent Advances in Synthesis and Properties of Hybrid Halide Perovskites for Photovoltaics. Nano-Micro Lett. 10, 68.

Wong, L.H., Zakutayev, A., Major, J.D., Hao, X., Walsh, A., Todorov, T.K., Saucedo, E., 2019. J. Phys. Energy 1, 32001.

Yang, W.S., Noh, J.H., Jeon, N.J., Kim, Y.C., Ryu, S., Seo, J., Seok, S. Il, 2015. Science (80). 348, 1234-1237.

Yoon, W., Boercker, J.E., Lumb, M.P., Placencia, D., Foos, E.E., Tischler, J.G., 2013. Sci. Rep. 3, 1.

Yuan, M., Liu, M., 2016. Nature Energy 1, 16016.

Yun, A.J., Kim, J., Hwang, T., Park, B., 2019. ACS Appl. Energy Mater. 2, 3554-3560.

Zuo, F., Williams, S.T., Liang, P.W., Chueh, C.C., Liao, C.Y., Jen, A.K.Y., 2014. Adv. Mater. 26, 6454-6460.

<https://www.nationalgeographic.com/environment/article/fossil-fuels> (accessed3.03.19.)

<https://unfccc.int/process-and-meetings/the-paris-agreement/the-paris-agreement/key-aspects-of-the-paris-agreement> (accessed 02.02.19)

CHAPTER 2

PREPARATION METHODS AND OVERVIEW OF PHYSICAL PROPERTIES

2.1 INTRODUCTION

Solar energy is energy is considered one of the most promising, abundant, and attractive sources of renewable energy to replace fossil fuels. To harvest and convert solar energy effectively into electricity, various novel solar cell techniques have been developed over the years. The advancement of emerging solar cell technology such as perovskite has been rapid. The renaissance of organic-inorganic perovskite materials has set off a revolutionary journey in the history of photovoltaic research. Their intriguing physical and chemical properties offer scientists a fantastic possibility in the advancing solar cells field. Nevertheless, the toxicity of the precursors such as Pb in perovskite has become an urgent matter in the development of perovskite solar cells.

To deal with this issue, a partial substitution or complete substitution of Pb precursor with tin in perovskite solar cells has been suggested to reduce the toxicity in the fabrication (Shao et al., 2018). For example, a partial substitution of tin in perovskite has achieved a remarkable power conversion efficiency of 14%, which is among the highest efficiencies for Sn-enriched, as reported by Mohammad M. Tavakoli, Michael Grätzel et al. in 2018 (Tavakoli et al., 2018). Complete substitution of Pb precursor with elements such as Ge, Sb, Bi, and Sn is being investigated and has been reported with a low efficiency so far (Eperon and Ginger, 2017; Kojima et al., 2009). Furthermore, the vapour deposition technique is used to synthesise the material and that may prevent the presence of the soluble Pb element in the perovskite molecule and manufacture at a low cost as well (Mitzi et al., 2004).

2.2 OVERVIEW OF PEROVSKITE MATERIAL

Perovskite ($CaTiO_3$) was discovered in the Ural Mountains of Russia by Gustav Rose, who named it in honour of the Russian mineralogist Lev Perovski (Randall et al.,2009). In 1945, Helen Dick Megaw was the first to record the composition of perovskite materials. His study confirmed the previous work done by Goldschmidt, who discovered that various ranges of perovskite existed. Soon after, Topsöe showed that the mixing of the organic−inorganic halide compounds (such as methyl-ammonium and lead halide or formamidinium and lead halide) were in the same family as the discovered perovskite ($CaTiO_3$, $BaTiO_3$). Later, several synthetic perovskite compounds with the general formula AMX_3 perovskite were identified (where A= organic or inorganic cation, M= metal, and X= halogen or oxygen), such as $CH_3NH_3[Pb/Sn]I_3$, $HC(NH_2)_2PbX_3$, $Rb[Pb/Sn]X_3$, $Cs_2BiAgBr_6$, $CsPbI_3$ (Randall et al., 2009; Saparov and Mitzi, 2016). In 1978 Weber reported (Saparov and Mitzi, 2016) on metal M (Pb- and Sn)--based halide perovskite materials, and shown the stabilization of a cubic structure at ambient temperature (Randall et al., 2009). The 'A' atoms are larger than the 'M' atoms, and the ideal cubic structure of 'M' cation has 6-fold coordination, surrounded by an octahedron of anions formed by X, and while the 'A' cation has 12-fold cuboctahedra coordination. The 'A' type atom sits at cube-corner positions (0, 0, 0), the 'M' type atom at a body-centred position (1/2, 1/2, 1/2) and X (oxygen) atoms sit at face centred positions (1/2, 1/2, 0) for an oxide type (Chen et al., 2018).

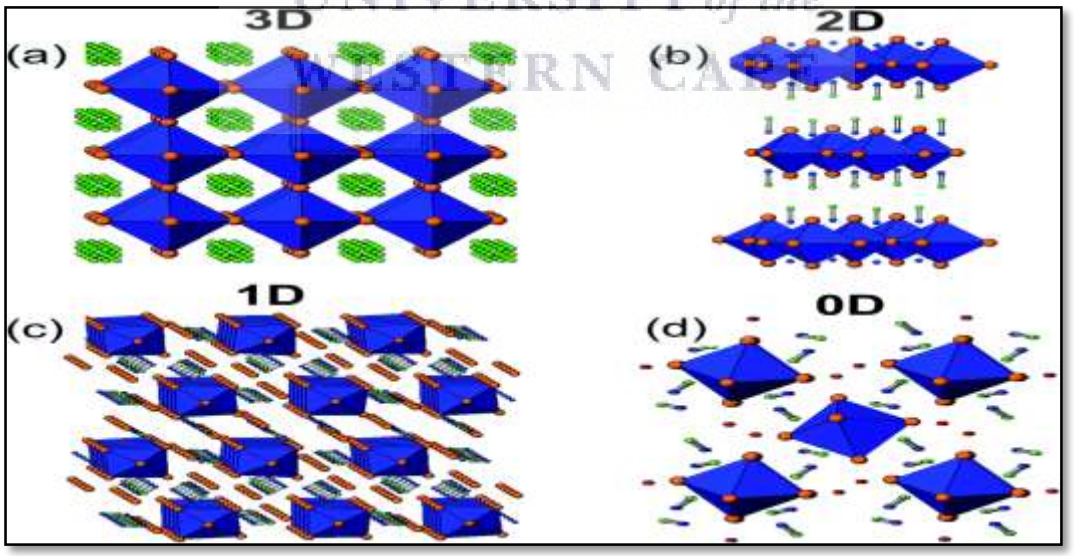

Figure 2.1 (a) $CH_3NH_3PbI_3$, (b) $(CH_3NH_3)_2PbI_4$, (c) $(C_{10}H_{21}NH_3)_2PbI_4$, & (d) $(CH_3NH_3)_4PbI_6{\cdot}2H_2O$, corresponding to 3D, 2D, 1D & 0D networks. The blue polyhedra represent the MX_6 (M ¼ ; X ¼) octahedra with the halogens in orange spheres (Sum and Mathews, 2014).

However, the class of halometallates perovskite materials such as iodometalates (group 14) is of special interest since they adopt perovskite structures that are receptive to the compositional variation structure of AMX_3 (Sum and Mathews, 2014). Furthermore, the dimension of the inorganic-organic perovskite (or halometalate perovskite) depends on the size of the A-cation. When a small cation is used, the three-dimension 3D is obtained and when a larger cation is used, there is either one dimension (1D), two-dimension (2D), or zero-dimension 0D, depending on the material (Fig2.1) (Sum and Mathews, 2014). The different perovskite dimensions obey to the following formula: AMX_3, A_2MX_4, A_3MX_5, and A_3MX_6, such as $CH_3NH_3PbI_3$, $(CH_3NH_3)_2PbI_4$, $(C_{10}H_{21}NH_3)_2PbI_4$, and $(CH_3NH_3)_4PbI_6{\cdot}2H_2O$, which belong to 3D, 2D/1D, 1D and 0D, respectively. For example, the $CH_3NH_3PbI_3$ (Fig2.1) perovskite belongs to a large family of organic-inorganic perovskites where the $[PbI_6]^{4-}$ octahedral can form three dimensional (3-D), two-dimensional (2-D), one-dimensional (1-D) or even zero-dimensional (0-D) networks, and possessing the same unit structure (Sum and Mathews, 2014). In a 3-D network (Fig2. 1(a)), each $[PbI_6]^{4-}$ octahedron relates to six neighbours– iodide. Moreover, according to Goldschmidt, the halide perovskites keep an optimum crystal symmetry by maintaining an allowable geometric tolerance factor (t) and has the stability distortion of the crystalline structures of a compound (Tavakoli et al., 2018). The tolerance factor (t) is determined from the radii sizes associated with a cubic symmetry as described by the formula below:

$$t = \frac{R_A + R_X}{\sqrt{2}\,(R_M + R_X)} \qquad Eq.\,1.1$$

Where R_A ,R_M ,R_X are the ionic radii of A, M, X, respectively.

Additionally, it gives an idea of whether the phase is cubic (t=1) or deviates like a tetragonal or orthorhombic phase (Hussain et al., 2018). Generally, an established tolerance factor value for halide perovskites lies in the range of $0.85 < t < 1.11$, and as such, non-perovskite structures are formed when the tolerance factor is out of the range (Hussain et al., 2018; Saparov and Mitzi, 2016), with the temperature being one of the variables that affect the tolerance factor. An efficient organic-inorganic perovskites have to have a compatible organic component that facilitates the self-assembly of the inorganic structure on a substrate, while the inorganic component offers the opportunity for higher mobility of electrons (Mitzi et al., 2004). The combination of the organic and inorganic components is more efficient compared to a single organic/or inorganic system. It is also based on the decomposition of soluble precursors that

enables the deposition of metal halide, known as a class of materials with potential use in solar cells (Mitzi et al., 2004).

2.3 TOXICITY OF PEROVSKITE AND Pb^{2+} CATION SUBSTITUTION

The use of lead (Pb) precursors in the perovskite compound severely limits their broad applications and commercialization because of the toxicity as mentioned previously, that might be hazardous to both humans and the environment. The development of Pb-free perovskite solar cells is highly desirable and has drawn significant attention (Aramaki and Kanatzidis, 2016). Theoretical studies have shown that the superior solar cell properties of Pb halide perovskites are partly attributed to the perovskite structure and the inactive outer shell—s Pb(6s) orbitals (Chung et al., 2012; Hao et al., 2014; Jiang et al., 2018). Therefore, it has been suggested that lead cation (Pb^{2+}) can be replaced with other cations that are environmentally friendly and also contain the inactive outer shell—s orbitals such as germanium (II) (Ge^{2+}) (Marshall et al., 2016), tin (II) (Sn^{2+}) (Chiarella et al., 2008; Even et al., 2014), antimony (III) (Sb^{3+}), and bismuth (III) (Bi^{3+}) to form Pb free perovskite solar cells (Kim et al., 2014; Zuo et al., 2014). So far, Kanatzidis et al. on one side and Snaith et al.in the other, have independently demonstrated methyl-ammonium tin iodide ($MASnI_3$) based as Pb-free PVSCs with PCEs of around 6% in 2014 (Chiarella et al., 2008; Even et al., 2014). These reports have stimulated considerable follow-up studies on Pb free by Sn-based perovskite solar cells (Aharon et al., 2014; Giles E. Eperon and Ginger, 2017; Mei et al., 2014; Pellet et al., 2014; Suarez et al., 2014; Zhao et al., 2017). Additionally, tin (Sn) is considered the best alternative to replace lead among the other metals. Because Sn-based perovskites have shown to exhibit outstanding electrical and optical properties such as high charge carrier mobility, high absorption coefficients, and low exciton binding energies (Chung et al., 2012; Marshall et al., 2016). Moreover, tin(II) is a less toxic divalent metal with the ionic radius of (Sn^{2+} 1.35Å), which is comparable to those of Pb^{2+} (1.49Å) (Giles E. Eperon and Ginger, 2017; Zuo et al., 2014). According to Even et al. and Chiarella et al. (Chiarella et al., 2008; Even et al., 2014) Sn perovskite has suitable band gaps and favourable effective mass. Conversely, the main disadvantage concerning the substitution of lead divalent cation (Pb^{2+}) with tin divalent cation (Sn^{2+}) in perovskite solar cells, is the sensitivity of Sn when exposed to air. It oxidizes easily from Sn^{2+} to Sn^{4+} (Ogomi et al., 2014), thus losing the perovskite structure and their physical function. Figure 2.2. shows the position occupies by the metal (Pb-Sn) and the organic cation.

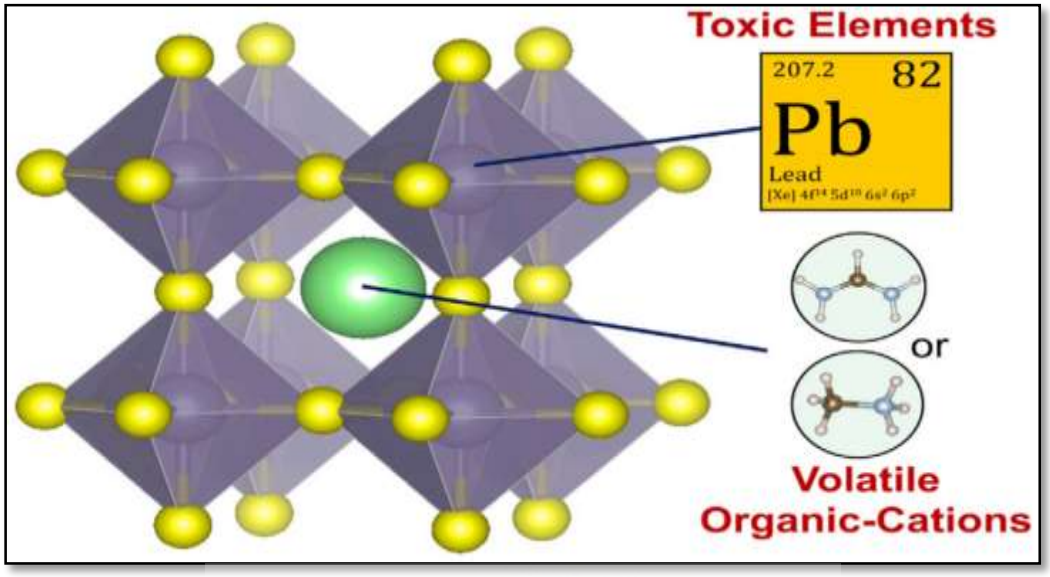

Figure 2.2: Schematic Illustration Showing the Crystal Structure of the Prevailing Pb-Based Organic-inorganic perovskite (Ju et al., 2018)

Consequently, the effectiveness of perovskite solar cells based on Sn^{2+} has been lower than those of Pb^{2+}. Hence, in an attempt to reduce its toxicity as well as maintain the stability, the alloying of Pb is of paramount importance (Zuo et al., 2014). So far research has been conducted for the Pb-Sn alloy perovskite ($CH_3NH_3Pb_{1-x}Sn_xI_3$) compound, whereby the calculated bandgap of the combination of Pb and Sn (variables dependent— where $x<0.8$), is interestingly smaller than that of both original compounds independently. Overall, the most likely candidate to this day appears to be Sn^{2+} and Ge^{2+} when seeking for lead (II) substitution in perovskite materials to reduce or even eliminate the toxicity. Even though the low performance and instability of perovskite restrain their application, due to the oxidation of the Sn^{2+} to Sn^{4+} and Ge^{2+} to Ge^{4+} (Giles E. Eperon and Ginger, 2017).

2.4 PROPERTIES OF INORGANIC-ORGANIC PEROVSKITE

The properties of organic-inorganic perovskites depend on factors such as phase transition, bandgap, electronic structure, absorption capability.

2.4.1 PHASE TRANSITION, LATTICE PARAMETERS OF 3-D PEROVSKITE

It is important to understand the influence the temperature has on the performance of the perovskite layer and a solar cell device, as solar cells are exposed to a wide range of climates (Djuri and He, 2017). Previous studies have shown that the crystallographic phases of perovskites are directly related to the temperature (Djuri and He, 2017; Ogomi et al., 2014). The effect of temperature on perovskite is due to the molecular motion of the cation along the crystal axis, causing the modification in rotation, hence undergoing a structural phase transition (Ogomi et al., 2014).

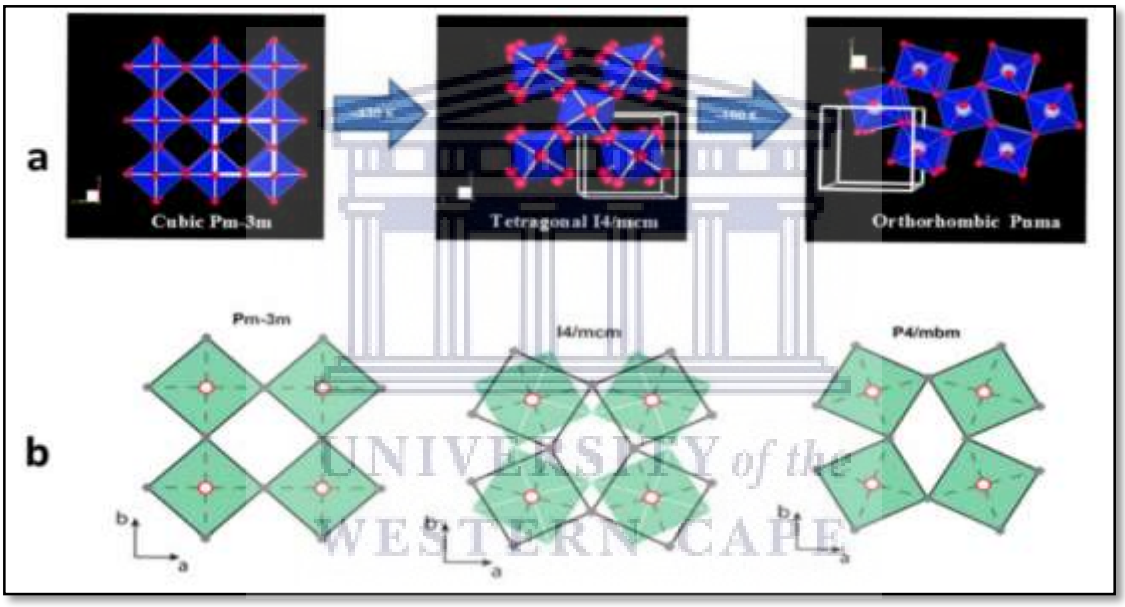

Figure 2.3: Crystal structures adopted by perovskite: α- $CH_3NH_3SnI_3$, $CH_3NH_3Pn_{1-x}Sn_xI_3$, β-$CH_3NH_3PbI_3$. (a) The $[PbI_6]^{4-}$ octahedra are blue and the iodine atoms are red. (b) The relative rotations of neighbouring layers of $[PbI_6]^{4-}$ octahedra along the c axis (Hao et al., 2014; Im et al., 2015; Saliba et al., 2016; Stoumpos et al., 2013; Whitfield et al., 2016).

There are three distinct structural modifications or phase transition, classified such as the high-temperature α-phase, the intermediate temperature β-phase, and the low-temperature γ-phase, while the non-perovskite yellow phase is termed the δ-phase (Jung and Park, 2015). The phase transitions are detected via the quenching of molecular motion, or by the first principle calculations based on the density functional theory (DFT), and the crystal structure and lattice expansion are investigated by X-ray diffraction XRD.

Generally, the perovskite phase transition undergoes a structure modification (Fig2.3) from cubic → tetragonal → orthorhombic as the temperature is lowered (Jung and Park, 2015). The inorganic-organic perovskites have a phase transit temperature range from 300K to 100K where the α-phase is converted to β-phase, except for $CH_3NH_3PbI_3$ where the conversion occurs at about 333K and the symmetry is reduced through the octahedral tilting (Stoumpos et al., 2013).

A pure octahedral tilting starts from an ideal cubic (with space group $Pm\bar{3}m$) structure which follows a specific sequence of descending symmetry and leading to a certain set of possible space groups. Also as the temperature decreases, further symmetry lowering occurs leading to the γ-phase, which is encountered close to 100k (Hao et al., 2014; Stoumpos et al., 2013; Whitfield et al., 2016). To put this into perspective, first, the **α-phase** of $CH_3NH_3SnI_3$ (1) perovskite is found at room temperature and consists of the pseudo-cubic unit cell with lattice parameter being $a = 6.2307(10)$ *Å* and volume $V=241.88(7)$ $Å^3$, while the α-phase for $CH_3NH_3PbI_3$ (3), also pseudo-cubic but forms after a phase transition has occurred at temperature >50°C with $a = 6.3130(2)$ *Å* and $V=251.60(2)$ $Å^3$. The crystal structures of $CH_3NH_3SnI_3$ (1) and $CH_3NH_3PbI_3$ (2) are non-centrosymmetric at room temperature. The observed space groups are then classified into the "ferroelectric distortion" category, which means that they are subgroups of the ideal cubic $Pm\bar{3}m$ space group (Stoumpos et al., 2013). The symmetry elements are lost as a result of the metal M cation displacement from the centre of the octahedron, though the ferroelectric displacement is the only marginal such that 0.08 Å along c-axis for $CH_3NH_3SnI_3$ (1) and 0.05 Å along c-axis for $CH_3NH_3PbI_3$ (3) from the ideal position (Stoumpos et al., 2013). Hence, the tetragonal P4mm space group is adopted at a higher temperature phase for both $CH_3NH_3SnI_3$ (1) and $CH_3NH_3PbI_3$, and the displacement occurs along the tetragonal c-axis. Similarly, like $CH_3NH_3SnI_3$, the α-phase of **$CH_3NH_3Pn_{1-x}Sn_xI_3$ (3)** is found at room temperature and the structure also consists of the pseudo-cubic unit cell. Conversely, a compound (where x=0.75) is unique in adopting a trigonal phase at room temperature with $a=b=8.9817(13)$ *Å*, $c = 11.0060(20)$ *Å*, and $V=768.9(2)Å^3$ (Ogomi et al., 2014; Stoumpos et al., 2013). Whereas another inorganic-organic perovskite such as $HC(NH_2)_2SnI_3$ adopts an orthorhombic structure, but at high temperature, and has space group Amm2, thus the metal-atom displacement occurs along the a and b axes (Stoumpos et al., 2013). Secondly, the **β-phase**, of both $CH_3NH_3SnI_3$ and $CH_3NH_3PbI_3$ distort similarly, showing out-of-phase tilting of the polyhedral that is combined with a ferroelectric type of off-centering along the c-axis and adopting the tetragonal structure. Therefore, the compound $CH_3NH_3SnI_3$

(1) changes to the β-phase (tetragonal phase) about 200K region with *a =b= 8.7577(15), c = 12.429(3) Å* and *V=953.2(3) Å*^{3}, followed by other transitions. Similarly, $CH_3NH_3PbI_3$, changes to β-phase at about 293 K. The $CH_3NH_3PbI_3$ perovskite has a tetragonal phase with space group I4/mcm, and the lattice parameters are *a=b= 8.849(2) Å, c = 12.642(2) Å,* and *V = 990.0(4) Å*^{3}. Conversely, compounds such as $HC(NH_2)_2SnI_3$ and $HC(NH_2)_2PbI_3$ perovskite form their β-phase below 200 K (Stoumpos et al., 2013). Additionally, the ferroelectric displacement component is microscopic and affects the polarization of the octahedral along the c-axis. Therefore, the tilting angle is about 17.4° and 16.4° for $CH_3NH_3SnI_3$ and $CH_3NH_3PbI_3$ which were measured at 150 K and 293 K, respectively (Stoumpos et al., 2013).

Table 2.1. Crystallographic Data of α, β-Phases (Stoumpos et al., 2013).

Characteristic	**Perovskite materials**				
	α,β-$CH_3NH_3SnI_3$	α,β-$HC(NH_2)_2SI_3$	.α,β-$CH_3NH_3PbI_3$	.α,β-$HC(NH_2)_2PbI_3$	β-$CH_3NH_3Sn_{0.46}Pb_{0.54}I_3$
T (°K)	293(2)K, 200(2) K	340(2)K, 180(2) K	400(2)K, 293(2) K	293(2)K, 150(2) K	293(2) K
Crystal system	pseudo cubic/ tetragonal	Orthorhombic	pseudo cubic /tetragonal	Trigonal	Tetragonal
space group	P4mm/ I4cm	Amm2	P4mm/ I4cm	P3m1	I4cm
crystal size (mm^{-3})	3.561×10^{-5} and 1.560×10^{-3}	3.901×10^{-3} and 1.26×10^{-6}	1.309×10^{-5} and 3×10^{-8}	2.238×10^{-5} and 2.622×10^{-5}	3.3311×10^{-3}
θ range	3.27-28.94° & 4.65-24.94°	3.22-29.11° & 2.30-29.15°	3.23-24.92° & 3.26-29.03°	1.85-29.19° & 1.87-25.00°	2.82 - 29.01°

Thirdly, the **γ-phase** of $CH_3NH_3SnI_3$ (1) is observed around 130 K and of $HC(NH_2)_2SnI_3$ is at 110 K, while the one of the $CH_3NH_3PbI_3$ (3) adopts a γ-phase at about 162.2K which is

orthorhombic with a space group Pna2. However, for all inorganic perovskite such as $CsSnI_3$/ $CsPbI_3$, the phase transition is at about ~425K to the tetragonal structure–P4/mbm (double cell volume), before obtaining an orthorhombic structure–Pnma (quadruple cell volume) below 351 K. Such a sequence is described by considering a pure perovskite tilting model, and by ignoring ferroelectric type displacement (Stoumpos et al., 2013). And lastly, the **δ-phase** is a non-perovskite phase. The δ-phase of the organic-inorganic perovskite such as $HC(NH_2)_2PbI_3$, is different from all-inorganic perovskite (e.g. in $CsSnI_3$ and $CsPbI_3$). In the former, the structure consists of face-sharing octahedral propagating along the (001) direction forming single chains, with the cations occupying the space between the chains, thus adopting a nearly hcp-lattice (P63mc). In the latter case, the structure comprises of a double chain of $[MI_6]^{4-}$ octahedral. The intra-chain linking of the polyhedral in the individual chains is affected by edge-sharing of square pyramidal units. While the octahedral coordination occurs by inter-chain bonding by a relatively longer M−I bond with an iodide occupying a basal position of the square pyramid, overall adopting the NH_4CdCl_3-type structure (Stoumpos et al., 2013).

2.4.2 METAL ALLOYING: CASE of $(Pb_{1-x}Sn_x)I_2$ in $CH_3NH_3Pb_{1-x}Sn_xI_3$

The alloying of lead with a metal such as tin (Sn) reduces not only the toxicity in perovskite, but also decreases the energy bandgap, which has a positive effect on the absorption capability. This can be achieved by two processes: (i)wet chemistry-based and (ii)physical evaporation method. When alloying Pb with Sn, various physical quantities such as diffusion temperature, spin-orbital coupling (SOC) strength, bandgap as well as positions of metal (Pb/Sn) and iodine (I) atoms can be affected (Kim et al., 2014b). The temperature effects on the crystal size of the material, leading to a change in phases. For example, when $MASnI_3$ (pure Sn-based) perovskite crystallises in β-phase, the SOC strength is reduced, while the off-centering of Sn is slightly larger than β-phase of $MAPbI_3$ (pure Pb-base) perovskite (Kim et al., 2014a, 2014b). In the case of alloyed metal— $[Pb_{1-x}Sn_x]I_2$, the metal iodide adopts the type of corner-sharing $[Pb_{1-x}Sn_xI_6]^{-4}$ octahedral in which the metal site is randomly occupied by either Sn or Pb atoms throughout the reaction. Given the fact that both $CH_3NH_3SnI_3$ and $CH_3NH_3PbI_3$ crystallize at ambient conditions in the pseudo-cubic P4mm (α-phase) and tetragonal I4cm (β-phase) space groups, respectively, but at elevated temperatures (about 330 K), $CH_3NH_3PbI_3$ undergoes a reversible structural phase transition to the P4mm space group becoming isostructural to its Sn analogue. The same structural transition is realized in the $CH_3NH_3Pb_{1-x}Sn_xI_3$ (near x = 0.5) and

switching from the P4mm space group (characteristic of Sn-rich compositions) to I4cm space group (characteristic of Pb-rich compositions) (Zhao et al., 2017). The change in the space group is then induced by a rotation of the $[MI_6]^{4-}$ octahedral (Zhao et al., 2017). Additionally, the diffraction patterns from the X-ray display two peaks within the range between 22°–25° 2θ ($x < 0.5$), indexed to (211) and (202) planes in the tetragonal (I4cm space group), which can gradually merge to a single peak (113)—corresponding to the plane in the P4mm space group (cubic)—when the variable x becomes greater than half ($x>0.5$) (Zhao et al., 2017).

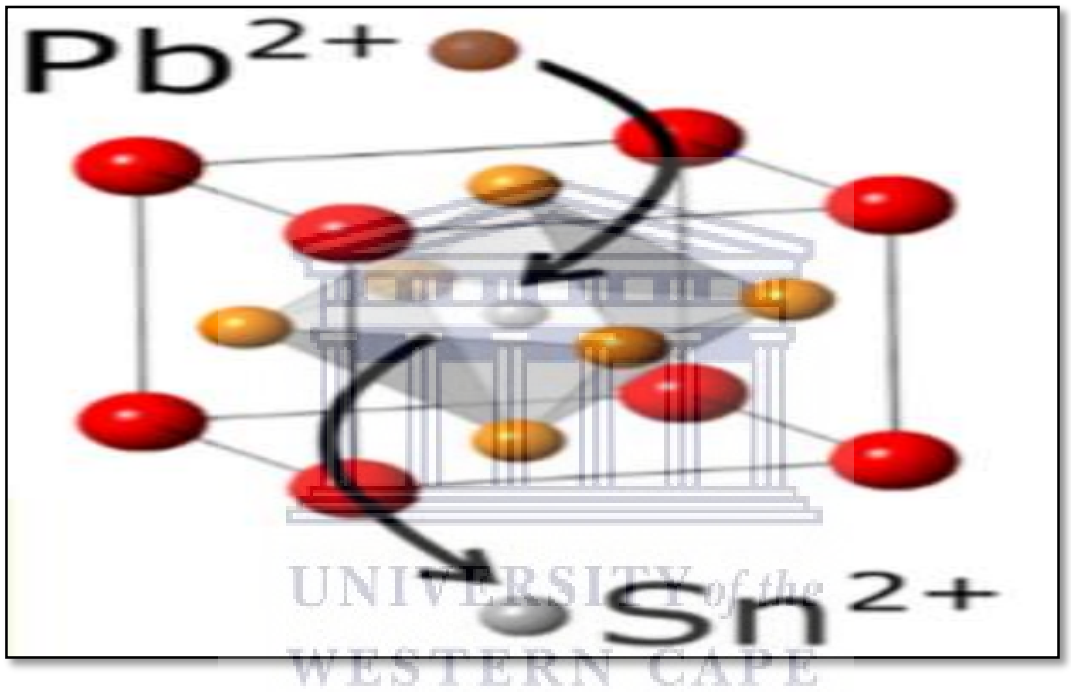

Figure 2.4: Shows metal cation alloying or substitution in organic-inorganic perovskites. Red is CH_3NCH_3, grey is Sn/Pb and yellowish is iodine. (Giles E. Eperon and Ginger, 2017).

Such transition involves a distortion of the relative positions of the octahedral about the 4-fold crystallographic c-axis. Furthermore, in the ideal case of $CH_3NH_3SnI_3$, the tilting angle between Sn—I atoms in the $[SnI_6]^{4-}$ octahedral is 177.43^o (1) ° slightly deviating from the ideal angle. Whereas, in $CH_3NH_3PbI_3$ the tilting angle between Pb—I atoms becomes larger at 163.55° significantly distorting the (PbI_3) framework (Im et al., 2015). Thereby reducing the symmetry of the unit cell. Again in a specific ratio between Pb and Sn of methyl-ammonium metal alloyed iodide— $CH_3NH_3Pb_{1-X}Sn_XI_3$ composition, the tetragonal (I4cm) structure is adopted, whereby the corresponding angle (Sn-I-Pb) is about 169.43° (Im et al., 2015). Thus,

the deviation from the ideal cubic (Pm3m) structure arises from the orientational ordering of the $CH_3NH_3^+$ cation along the crystallographic c-axis. The crystallography of P4mm and I4cm unit cells are related to one another. This is a distinctive feature of the organic cation $CH_3NH_3^+$-based perovskites over the inorganic Cs+ based (P4/mbm) or the organic HC-$(NH_2)_2$+ based (Amm2) (Hao et al., 2014; Im et al., 2015; Kim et al., 2014b).

2.4.3 ELECTRONIC PROPERTIES OF PEROVSKITE

The electronic structure of a semiconductor comprises a valence band (VB) and conduction bands (CB), which are the highest occupied energy band and the lowest unoccupied energy band, respectively. The bandgap energy (Eg) is the minimum energy required to excite an electron from the VB to the CB. Semiconductors are characterized by the energy gap values, and the band structure can be either direct or indirect (Wells, 2015). The top of the VB to the bottom of the CB can be found at the same k-value for a direct bandgap semiconductor, whereas the location is at a different k-values in the case of an indirect bandgap semiconductor as depicted in Fig 2.5.

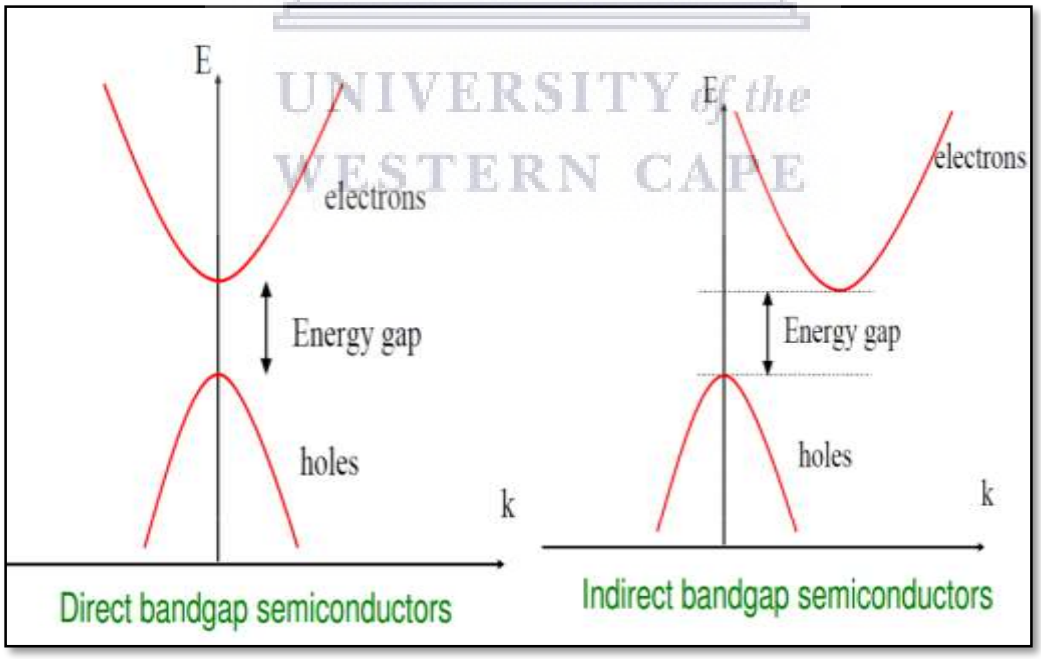

Figure 2.5: Schematic representation of direct and indirect electronic transitions (Wells, 2015).

Inorganic-organic perovskite as a semiconductor material is preferably direct bandgap materials, which allows strong optical transitions between the valence and conduction band (Aharon et al., 2015; Zhang et al., 2017). In inorganic-organic compounds, the conduction and the valence bands are also called lowest occupied molecules (LUMO) and highest occupied molecules—(HOMO), respectively. Moreover, the conduction band (CB) of the inorganic layer is lower than the organic layer, while the valence band (VB) of the inorganic is above the organic layer. Therefore, the inorganic part acts like a well, both for holes and electrons (Ahmad et al., 2018). The bandgap energy of organic and inorganic molecules may be offset by choosing appropriate components of both organic and inorganic materials (Ahmad et al., 2018). The electronic structure is maintained due to electronic liaisons or bonds. The inorganic perovskite layer interacts either ionically or by a hydrogen bond with the organic layer. The ammonium head(s) of the CH_3-NH_3 or NH_3-CH_3-NH_3 cations can make hydrogen bond to any of the eight halogens (four bridging and four terminals) within the holes formed by the corners sharing with MX_6 octahedral. Generally the NH_3 group links either to one terminal halogen and two bridging halogens (bridging halogen configuration) or to one bridging halogen and two terminal halogens (terminal halogen configuration) to form hydrogen bonds (see Fig 2.6.) (Ahmad et al., 2018).

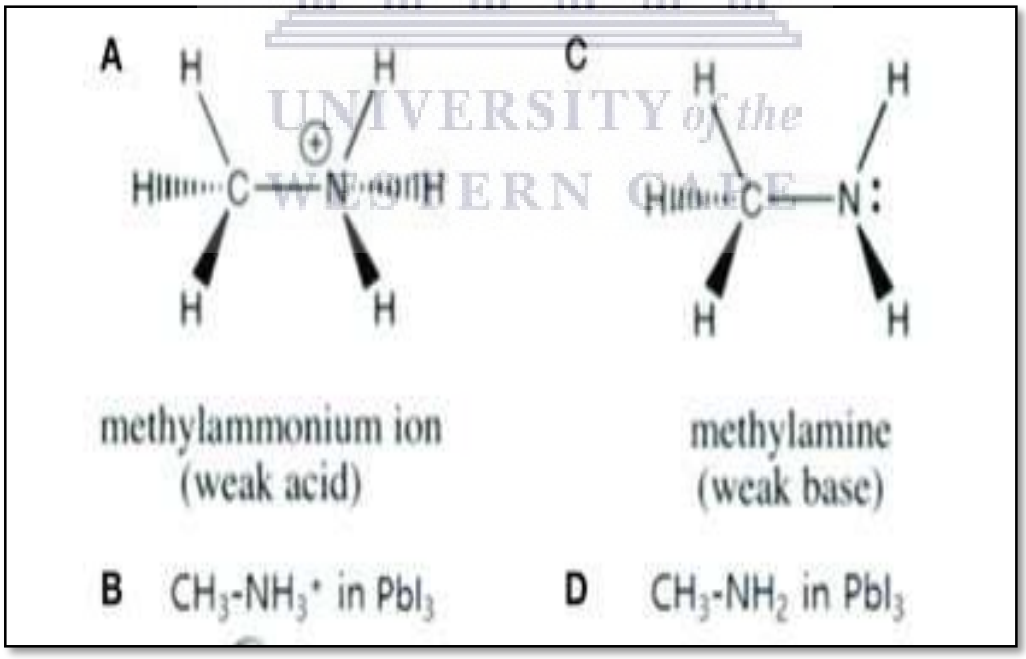

Figure 2.6: Chemical structure of the bonding organic methyl ammonium (Ahmad et al., 2018).

Furthermore, in the inorganic-organic perovskite, the metal halide MX_6 is responsible for the conduction and the valence band. Hence, at the conduction band minima (CBM), for example, the electronic structure of $CH_3NH_3PbI_3$ perovskite compound is formed from antibonding of PbI_6, which is I(5p)–Pb(6p) orbitals with the predominant character of the Pb(6p) atomic orbital, while the valence band maximum (VBM) is formed from antibonding I(5p)–Pb(6s) orbital interactions (Yang et al., 2015). Theoretical studies have demonstrated that firstly, the filled Pb(6s) state at the valance band maximum (VBM) is hybridized with the I(5p) states, and the conduction band minimum (CBM) is largely contributed by the Pb(6p) states (Yin et al., 2015). Consequently, the intra-atomic Pb(6s) to Pb(6p) transition probability is high, which is beneficial to the optical absorption (White et al., 2019; Yin et al., 2015). Secondly, the hybridization of Pb(6s) and I(5p) states significantly increases the VBM level. Additionally, the iodine-iodine (I—I) interactions in organic lead iodide perovskites are weak during the formation of defects due to their large ionic radius (White et al., 2019; Yin et al., 2015). Therefore, the antibonding (p- p σ*) state induced by I—I interactions are deeper than the VBM level, which can minimize the defect impacts on the performance of light absorption. Finally, the s-states are more diffusive than the other states (Fig2.7.) with the bonding (s- s*) orbitals). As such, the existence of s-states in the VBM can effectively lower the effective mass of holes, which will benefit the migration and separation of the photo-induced electrons and holes (White et al., 2019). Similarly, in the band structure of Sn-based $CH_3NH_3SnI_3$, consisting of Sn p-orbital states at the conduction band minimum (CBM), and the hybridized state is composed of Sn-s and I-p orbitals ($|5s\ Sn>$, $|5pI_x>$, $|5pI_y>$, $|5pI_z>$) at the valence band maximum (VBM) with a direct optical transition at a lower 5sp energy level (Im et al., 2015). The hybridized state at VBM has the zero angular momentum ($l = 0$) because of the Sn s-orbital, but the three Sn-p (x,y,z) orbital state at CBM has its own angular momentum $l = 1$. (Ansari et al., 2018; Im et al., 2015).

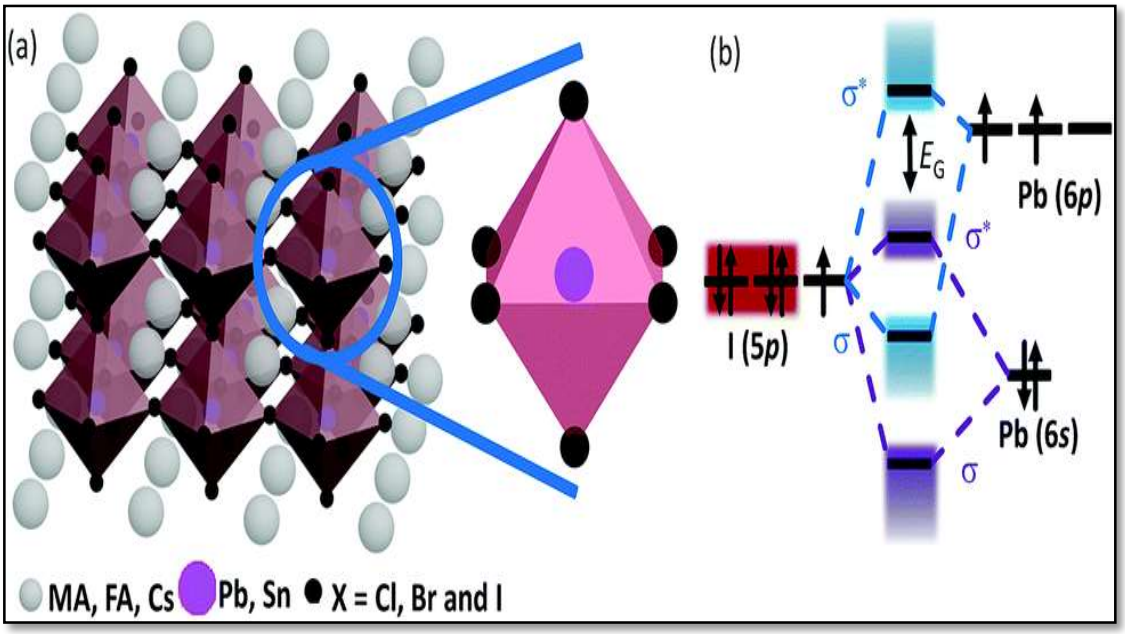

Figure 2.7: (a) Halide perovskite crystal structure(b) The bonding (s) and anti-bonding (s*) orbitals in $CH_3NH_3PbI_3$, the energy gap E_g, the conduction and the valence band (Chen and Schu, 2018).

2.4.4 CHARGE GENERATION MECHANISM

The magnitude of the bandgap determines which photons energies can be absorbed by the material. The photons with energy less than the bandgap will not be absorbed (Tanaka et al., 2001). When the photon energy is higher/equal to the bandgap, an electron is excited from the HOMO to the LUMO. The negatively charged electron (e−) in the LUMO leaves behind a positively charged hole (h+) in the HOMO. Since the electron and hole are strongly bound by Coulomb interaction due to a low permittivity, the electron-hole pair is called an exciton. Hence, the excitons produced by light absorption have weak-binding energy of about 26 meV at room temperature, which means that most of them dissociate very rapidly into free carriers at room temperature (Zhou H et al., 2014). The electrons and holes produced in the material, in our case perovskite layer, exhibit a small effective mass resulting in high carrier mobility of about 7.5 $cm^2\ V^{-1}\ s^{-1}$ for holes and 12.5 $cm^2\ V^{-1}\ s^{-1}$ for electrons. These have several direct implications in the operation of methyl-ammonium Pb-based perovskite solar cells, such that (1) The mobility of electrons and holes are at least 100 times higher than in organic solar cells ($\mu e = 0.005\ cm^2\ V^{-1}\ s^{-1}$, $\mu h = 0.02\ cm^2\ V^{-1}\ s^{-1}$) allowing a faster and more efficient extraction of charges to the electrodes; (2) The difference in the mobility between electrons and holes is within a factor of two. Because of this, electrons reach the electrodes as soon as the holes reach

the counter electrode, which means, the transport temperature balanced (Zhou H et al., 2014). Figure 2.8. shows the photoexcited electrons and holes dynamics in $MAPbI_3$.

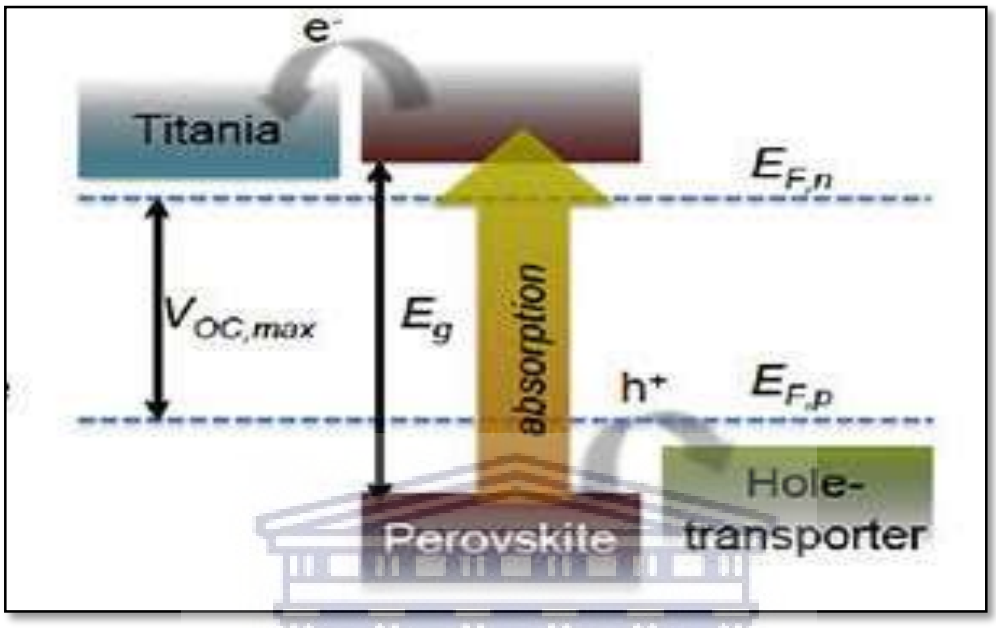

Figure 2.8: Schematic illustration of the photoexcited charge carrier (electrons and holes) dynamics in $MAPbI_3$ with spiro-OMeTAD as an HTM (Qing et al., 2016).

2.4.5 OPTICAL PROPERTIES OF PEROVSKITE

The light-harvesting capabilities of materials can be confirmed by their light absorption coefficient **α(ω).** The refractive index **n(ω)** of the light absorbers also has a strong influence on the light trapping (e.g. the Yablonovitch limit of $4n^2$ in solar cells with the isotropic emission pattern) (White et al., 2019.). Both α(ω) and n(ω) are calculated using the formula below. Firstly, the complex dielectric function $\varepsilon(\omega) = \varepsilon_1(\omega) + i\varepsilon_2(\omega)$ is calculated using the HSE06 hybrid functional, where ε_1 and ε_2 are the real part and the imaginary part of the dielectric function, respectively (White et al., 2019). After that, the absorption α(ω) is given by:

$$\boldsymbol{\alpha(\omega) = \frac{\sqrt{2\,\omega}}{c}\{\left[\,\varepsilon_1^2(\omega) + \varepsilon_2^2(\omega)\right]^{\frac{1}{2}} - \varepsilon_1(\omega)\,\}^{1/2}} \qquad \boldsymbol{Eq.2.1}$$

And the refractive index is given by:

$$\boldsymbol{n(\omega) = \frac{1}{\sqrt{2}}\{\left[\,\varepsilon_1^2(\omega) + \varepsilon_2^2(\omega)\right]^{\frac{1}{2}} + \varepsilon_1(\omega)\,\}^{1/2}} \qquad \boldsymbol{Eq.2.2}$$

Where ω = frequency of light and ε = dielectric function.

Equally, the absorption (A) of light, and thin film can also be defined using the equation below:

$$\boldsymbol{A = \alpha l} \qquad \boldsymbol{Eq.2.3}$$

Where $\boldsymbol{l}$ = thickness and $\boldsymbol{\alpha}$ = absorption coefficient.

And the absorption coefficient $\boldsymbol{(\alpha)}$ of a thin film can be used to estimate the direct energy gap (Eg) and by using the following equation:

$$\boldsymbol{\alpha(h\nu) = \left(E_g - h\nu\right)^{\frac{1}{2}}} \qquad \boldsymbol{Eq.2.4}$$

The absorption capability of perovskite can be enhanced by modifying the compound either by replacing/alloying the metal cation element (M-site), by replacing/substituting the organic cation element (A-site) or replacing/substituting the halide (X-site). In this chapter, we will not be discussing the substitution of the organic cation or the halide as it is not part of our research. However, we mentioned the crystallographic modification effect of alloying metal, which also affects the absorbance capacity of the perovskite material, since the bandgap is directly related to the metal halide.

The perovskite absorption is modified to certain wavelengths by incorporation a dopant in the metal cation. These substitution helps to tune the bandgap because they change the M–X–M bond length (Luo and Daoud, 2015). According to Junke Jiang (Jiang et al., 2018), the optical band gaps of $CH_3NH_3PbI_3$ evaluated theoretically are 1.66 eV with tetragonal structure and 1.57 eV with cubic structure, which are close to the experimental data. Also, research conducted by Hyun Suk Jung (Jung and Park, 2015), showing that the bandgap decreases from 1.55 eV to 1.17 eV when partially replacing the Pb(2+) by Sn(2+) in $CH_3NH_3Pb_{1-x}Sn_xI_3$ (see Fig2.9). On the contrary, the complete substitution of lead into tin shows a thorough increase in the bandgap as shown in Fig2.9. The change in metal halide modifies automatically the absorption capability of inorganic-organic perovskites (Liu et al., 2013; Ponseca et al., 2014). With a specific ratio (example between $0.25<x<1.0$), the alloying perovskite can be tuned and thus allowing the shift of the absorption edge in terms wavelength from 1000 nm to 1200 nm.

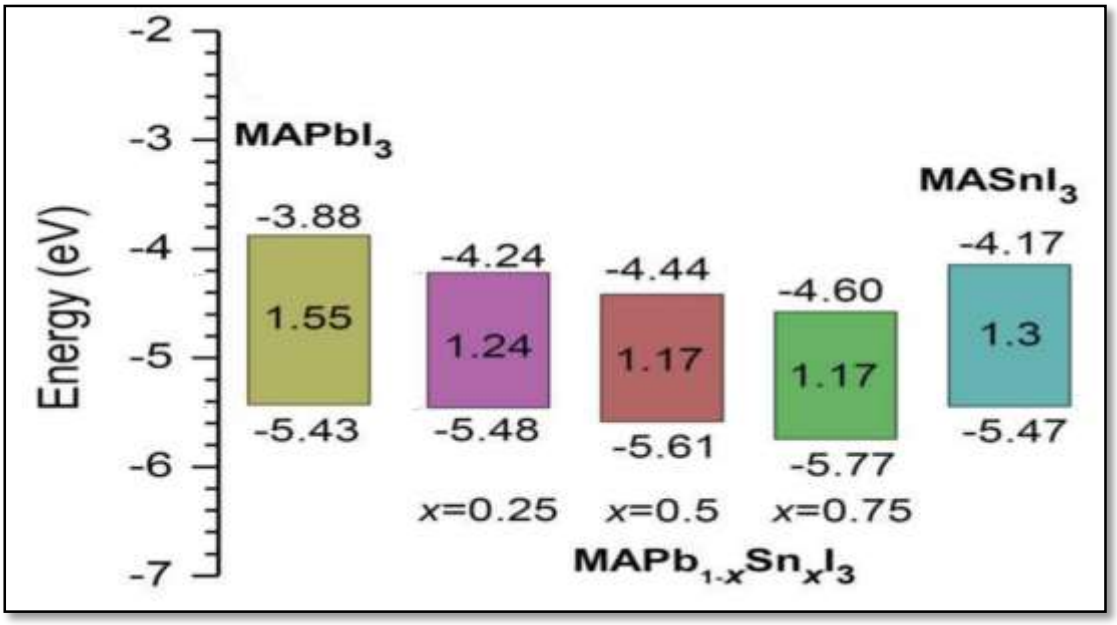

Figure 2.9: Schematic diagram of energy level of MAPbI3, $CH_3NH_3Pb_{1-x}Sn_xI_3$, and MASnI3. MA stands for methylammonium (CH_3NH_3). Data for $CH_3NH_3Pb_{1-x}Sn_xI_3$ (x = 0.25, 0.5, 0.75 and 1) (Jung and Park, 2015)

According to Yuhei Ogomi et al. observation, the valence band shift is larger than the conduction band shift on x change, standing from 5.12 eV to 4.73 eV for the VB and from 3.81 eV to 3.63 eV for CB (Ogomi et al., 2014), leading to the coverage of the entire visible spectrum and reaching up to the IR. This change is attributed to a possible anomaly in the bandgap modification of $CH_3NH_3Pb_{1-x}Sn_xI_3$ compositions, which is a function of variable **x** (Hao et al., 2014; Jung and Park, 2015; Ogomi et al., 2014). Figure 2.10 shows how the spectra of metal alloy perovskite are modified when varying Sn concentrations.

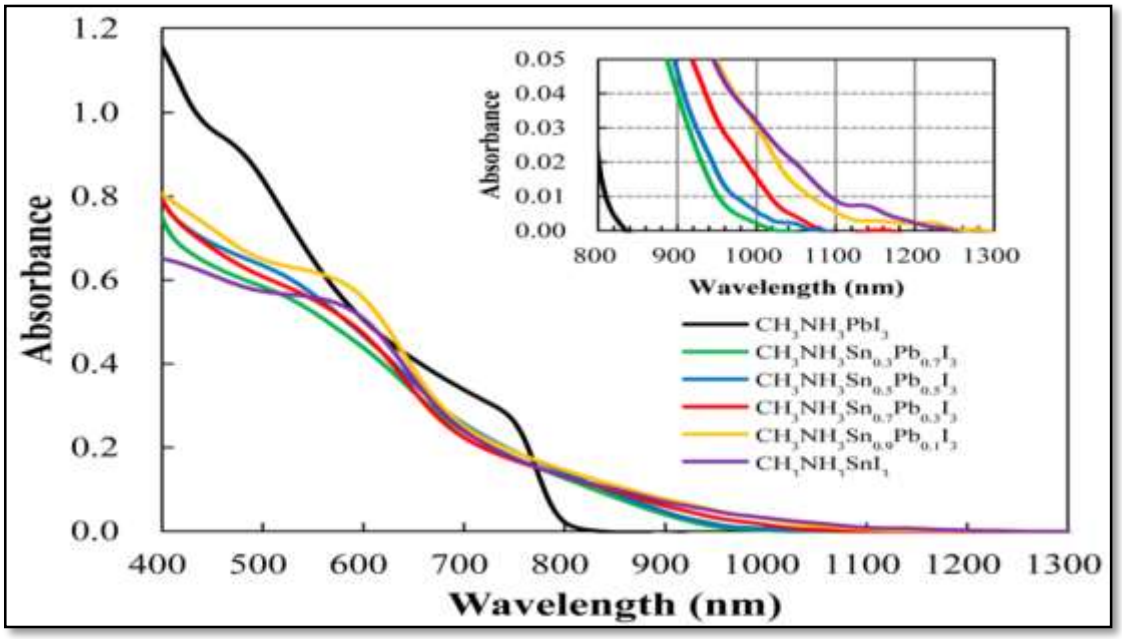

Figure 2.10: Electronic absorption spectra of $CH_3NH_3Pb_{1-x}Sn_xI_3$ perovskite (Ogomi et al., 2014).

2.5 ARCHITECTURE

There are mainly two architecture designs, the mesoscopic architecture and planar architecture.

- **The mesoscopic architecture**

It is the dominating device architecture of perovskite solar cells. In this design nanoparticles (NPs) are sintered on the electron transporting materials (ETM) such as TiO_2 to make it porous and then the perovskite layer is self-assembled within the interstice of mesoporous TiO_2 layer. This mesoporous TiO_2 network is necessary to assist the electron transferral through perovskite layer and the Fluorine-doped Tin Oxide (FTO) electrode (Grätzel et al., 2013). This configuration can be either conservative (n-i-p) or inverted (p-i-n) conformations relying on the order of depositing layers (see Fig2.11). Recently, Miyasaka's research group has created $CH_3NH_3PbI_{3-x}Cl_x$ perovskite solar cells built on plastic film utilising amorphous SnO_x and mesoporous TiO_2 layers as electron collectors (Kogo et al., 2017). Later on, Park et al. reported the highest efficiency of 17.3% with mesoscopic p-i-n solar cells employing a different porous metal oxide film (Park et al., 2015).

- **The planar architecture**

It is an evolution of the mesoscopic, where the perovskite layer (harvesting layer) is sandwiched between the electron transporting materials (ETM) and the holes transporting materials (HTM).

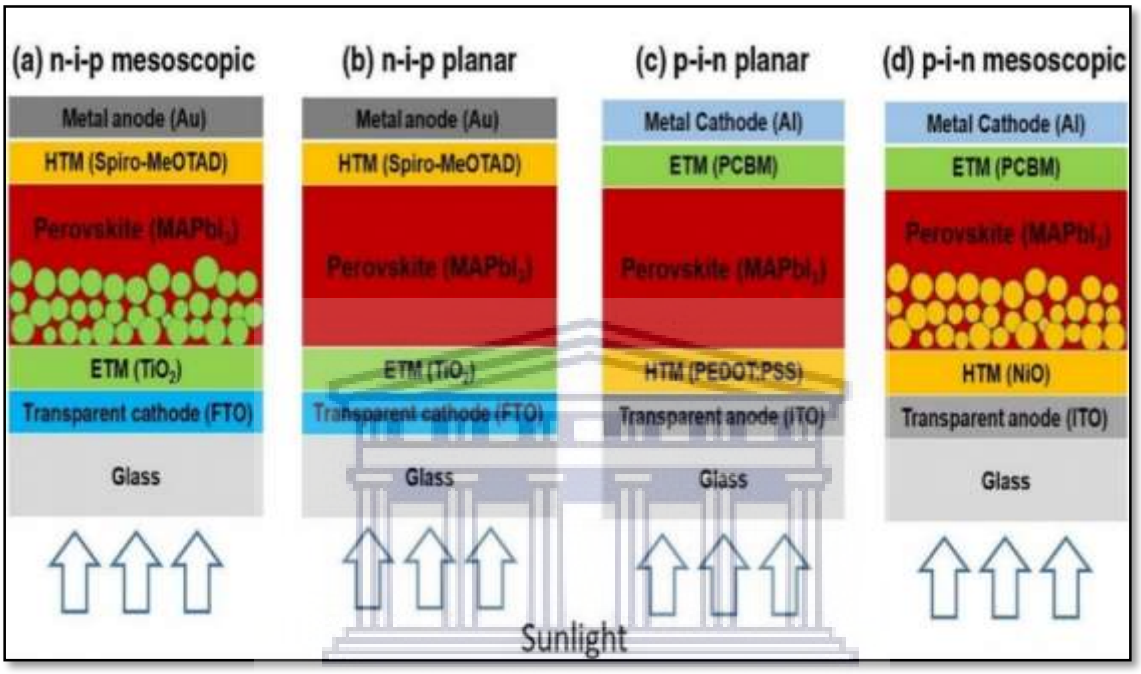

Figure 2.11: Schematics of architectures of perovskite SC in n-i-p and p-i-n configurations: (a) mesoscopic n-i-p, (b) planar n-i-p, (c) planar p-i-n, and (d) mesoscopic p-i-n. Reprinted with permission from (Ansari et al., 2018).

The absence of a mesoporous metal oxide layer leads to an overall simpler configuration. This type of architecture has the closest similarity with the conventional silicon-based cells (Yan et al., 2014). Planar architecture perovskites are essentially classified into conservative (n-i-p) and the inverted (p-i-n) conformations depending on the order of depositing layers as seen in Fig2.11. The efficiency of the planar n-i-p device has been recorded by Zhou et al. whereby they accurately optimized the electron specific interfaces of indium tin oxide (ITO) and demonstrated a power conversion efficiency of 19.3% (Zhou et al., 2014). The standard planar layout is glass/TCO/ETL/perovskite/HTL/metal, whereas the inverted architecture depositing order is glass/TCO/HTL/perovskite/ETL/metal. In general, ETL/HTL acts as a selective carrier

extraction channel (Ansari et al., 2018). In brief, a planar n-i-p perovskite solar cell shows increased open-circuit voltage and short-circuit current density compared to a mesoscopic perovskite solar cell device. However, the planar configuration has also more severe current-voltage hysteresis which calls into questions of the accuracy of the reported efficiencies (Ansari et al., 2018; Kogo et al., 2017).

2.6 PREPARATION METHODS OF PEROVSKITE FILM

Manufacturing high-quality perovskite is essential to achieving the superior performance of perovskite solar cells. Several research groups have therefore made considerable efforts in producing perovskite films with modulated crystalline structures, morphologies, and optoelectronic functions. The optoelectronic characteristics of perovskite films rely substantially on the development of the film morphology (Q. Chen et al., 2015), meaning that the morphology has an impact on the effectiveness of charge dissociation, diffusion lengths, and charge recombination dynamics in the resulting perovskite films (Q. Chen et al., 2015). There are several parameters to consider improving the film morphology, such as a deposition technique, temperature conditions during the film growth, substrate temperature, annealing temperature, initial material proportion, solvents/additives used. It has been demonstrated that by meticulously engineering the film morphology and controlled processing, one can boost perovskite conversion efficiency of the perovskite solar cells (Zhou et al., 2014). Several techniques have been developed so far for manufacturing hybrid perovskite primarily: 1) solution processing (one-step and two-step deposition), 2) hybrid vapour-solution processing (or vapour assisted solution processing), and 3) vapour deposition. Note that all techniques are combined and illustrated in Fig2.12 under section 2.6.3.

2.6.1 SOLUTION METHODS

Perovskite film deposition by solution processing technique is a prominent method since it is facile, and the production cost involved is lower. There are two (2) solution methods available, that is, one-step and two-step coating deposition methods. Perovskite forms either by spin-coating of a mixed organic compound (e.g. (CH_3NH_3I)) and of the metal halide-- inorganic (e.g. PbI_2) solution (one-step coating) as shown in Fig2.12 a), or by spin-coating of the organic compound after coating with metal halide, also called two-step coating (Fig12 b). For the one-step coating method, the organic compound (CH_3NH_3I) and metal halide (PbI_2) are dissolved

in an appropriate solvent such as a polar aprotic solvent like N, N –dimethyl-formamide (DMF), gamma-butyrolactone (GBL), or dimethyl sulfoxide (DMSO), and then use as a coating solution. For the two-step coating method, a metal halide (PbI_2) solution is first coated on the substrate to form a PbI_2 film and then a solution of organic compound (CH_3NH_3I) is spun on the PbI_2 film. To prepare high-quality perovskite films, it is important to adjust coating parameters such as spinning rate and time, temperature, solution wettability, and viscosity, etc. Compared to one-step spin-coating, two-step spin-coating was found to exhibit better photovoltaic performance due to better morphology and interfaces (Leyden et al., 2014), which indicates that morphology control of perovskite film is crucial in achieving high-efficiency perovskite solar cells. Perovskite prepared by the two-step coating method shows cuboid-like crystals, whereas the one-step solution method of CH_3NH_3I and PbI_2 produced a random morphology (Leyden et al., 2014; Leyden et al., 2015)

2.6.2 VAPOUR-ASSISTED SOLUTION PROCESS

Vapour assisted solution process (VASP) is proved to be beneficial for the formation of a highly uniform and compact film. Like in Spin coating an annealed metal halide films react with the organic halide (such as MAI) vapours in a similar way (Liao et al., 2016; Pazoki et al., 2016; Wang et al., 2016). In this process, the reaction time plays a crucial role in yielding a highly crystalline film with low defect concentration. Suppressing the metallic constituents in solution-processed films is beneficial to reduce the carrier concentration in the films. The VASP process is therefore particularly suitable for light-absorbing materials that are sensitive to reduction and synthesis conditions (Wang et al., 2016). Yang et al. demonstrated a hybrid low temperature-based perovskite film (VASP), which builds up perovskite layers through a chemical reaction of an as-coated film of PbI_2 with CH_3NH_3I vapour (Fig2.12d). The resulting perovskite film manifests complete surface coverage, smoother surface with micrometre-sized grains, and complete precursor solution transformation.

2.6.3 VAPOUR DEPOSITION METHOD

Perovskite films can also be prepared by the thermal evaporation of chemicals, whereby materials (solid or powder) are heated up to their vaporizing point. Snaith et al. to construct $CH_3NH_3PbI_{3-x}Cl_x$ perovskite planar SCs by co-evaporation of the organic (CH_3NH_3I) and the lead chloride $PbCl_2$ through dual sources (Fig. 2.12c) (Liu et al., 2013b). Co-evaporation of

CH_3NH_3I and $PbCl_2$ leads to a $CH_3NH_3PbI_3$ phase, and the uniformity of the film was much better than that of the solution-processed films (Docampo et al., 2013; Liu et al., 2013b). Most research stated that the low-pressure deposition method seems to be better for thickness control, compared to the solution process (Tran et al., 2018). However, there is a limitation associated with this technique; thermal evaporation calls for evacuation of the chamber at higher vacuum levels which involves high cost, and thus mass production is not feasible (Cui et al., 2015). Moreover, in chemical vapour deposition (CVD), the chemical reaction takes place inside a chamber. In this technique, precursor molecules are vaporized and followed by the transport of the aerosol in an inert carrier gas like nitrogen to a substrate surface where the precursors are thermally decomposed. The group of Qi successfully synthesizes perovskite films using hybrid CVD, where thermal evaporation of $PbCl_2$ is followed by vapour phase deposition of MAI (Fig 2.12e) (Leyden et al., 2014.). These cells were remarkably stable and highly reproducible (Leyden et al., 2015; Luo et al., 2015).

Besides CVD, spray-coating is a viable processing protocol towards large-area, low-cost manufacture of perovskites. Figure 2.13f shows the schematic illustration of the spray process (Luo et al., 2015). It allowed us to manufacture a flexible perovskite layer (Das et al., 2015; Gamliel et al., 2015). Additional methods like blade-coating and slot-die were also implemented effectively, paving the way for low-cost and large-scale solar energy implementation (Fig 2.12g) (Hwang et al., 2015). This allows reaching very fine thicknesses.
In summary, vapour deposition of perovskite film turns out to be a simpler and tractable method. The obtained films are fine, smooth, and of superior quality films as compared to the solution-based method. The film is highly uniform with full surface coverage, whereas solution-based technique coats the perovskite on the substrate partially, with crystalline platelets (Ansari et al., 2018). As an economical means of reaching the manufacturing level, Chemical vapour deposition (CVD) is effectively applied to deposit perovskite films.

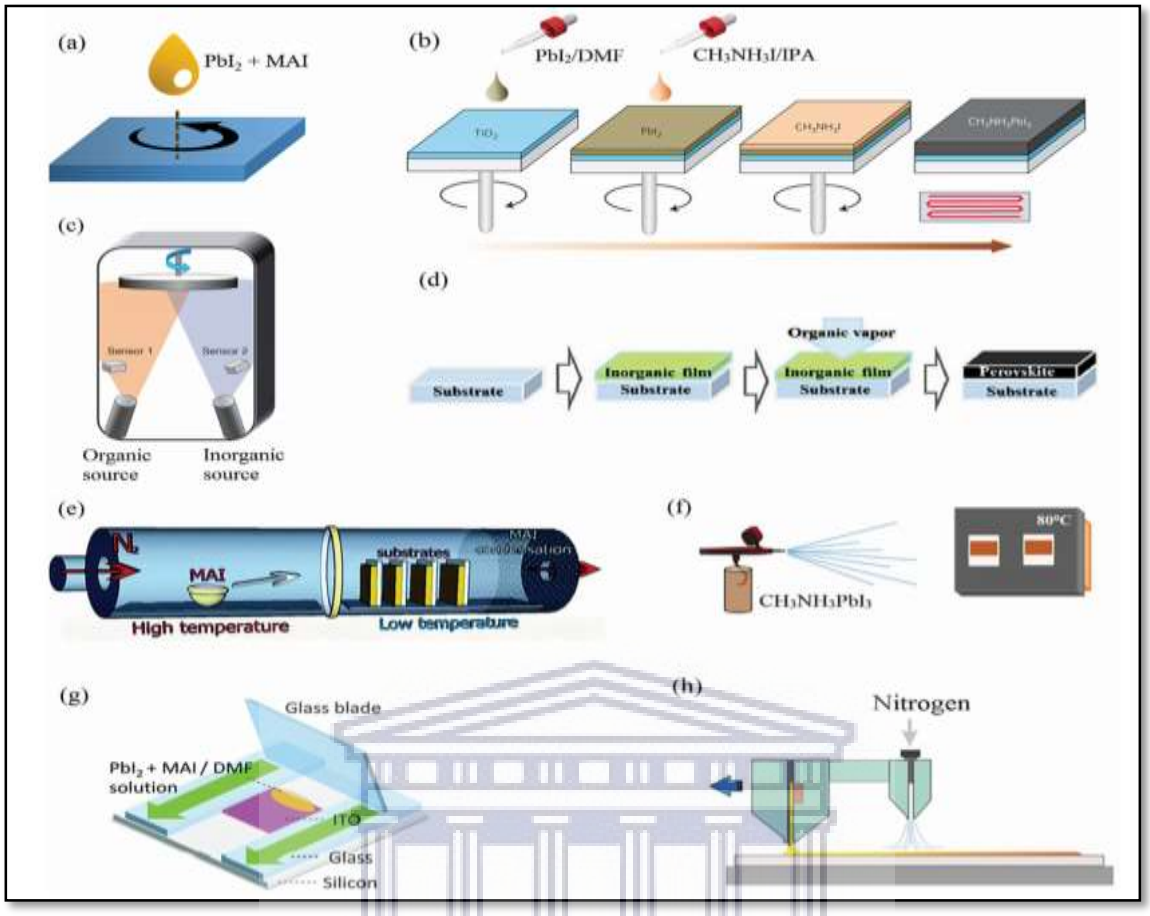

Figure 2.12: Deposition methods: a)One-step b)Two-step spin-coating c)Dual-source thermal evaporation d) Vapour-assisted solution process e)vapour deposition-based perovskite f)Spray deposition g) Doctor-blading h) Slot-die coating (Ansari et al., 2018; Q. Chen et al., 2015; Hwang et al., 2015).

2.7 MORPHOLOGY CONTROL

The majority of the above deposition techniques require a morphology control of the film to remove residual solvents (Hwang et al., 2015). Hence, two main processes are selected here for a better crystallization of perovskites. There are thermal annealing or additives in the growth process.

2.7.1 THERMAL ANNEALING

The thermal annealing process is arguably found to have a crucial effect on the formation and photovoltaic performance of perovskites. It can induce chemical and structural changes in the perovskite layer. According to the work of Wiesner et al., the solution-processed perovskite

films undergoes the evolutions between three distinct crystalline structures during thermal annealing (Chen et al., 2016). Crystalline precursors go through a solid-solid phase transformation to the 3D perovskite structure at 80 °C. This transition is consistent with Ostwald′s 'Rule of Stages' in which a metastable precursor is first formed and then transformed into a more stable product(Chen et al., 2016). But, thermal annealing of a mixed film of $MAPbI_3$ and $FAPbI_3$ is shown to have affected both bandgap and stability of the layers (Tan et al., 2014). Niwano and colleagues later found that by annealing, both $CH_3NH_3PbCl_3$ and $CH_3NH_3PbI_3$ crystals in mixed-halide perovskite layer, an amorphous phase are initially formed (Tan et al., 2014). Such amorphous phase and $MAPbCl_3$ crystals may be serving as ions supply for the growth of $MAPbI_3$ crystals when the MA and chloride ions are evaporated, resulting in a thin layer composed of large $MAPbI_3$ grains. Hence, the annealing temperature is of main significance in the formation of good or bad perovskite films. The study shows that the impact of the morphology and structure are linked with photovoltaic efficiency and operating processes. Annealing at temperature low leads to the removal of solvents. Yet the incomplete conversion of $CH_3NH_3PbI_3$ crystals perovskite is referred to as an endothermic reaction between PbI_2 and CH_3NH_3I. On the other hand, too high temperature has led to the formation of PbI_2, which is detrimental to the performance of the device. The optimal annealing temperature is thus determined in the range of 80−100°C, giving rise to the film morphology, which has consisted of an interconnected network of perovskite crystallites without additional PbI_2 (Aharon et al., 2015; Dualeh et al., 2014). However, longer time annealing results in a decomposition of perovskite into the PbI_2 stage, regardless of the annealing temperature. Controllable annealing might replace the traditional annealing method, where annealing temperature is increased gradually with time and which favours the formation of highly crystalline perovskite films (Hwang et al., 2015)

2.7.2 ADDITIVES

The additive-assisted growth methods are generally effective at controlling the shrinkage and volume expansion of precursor films in the deposition process (solution method) of perovskites. In general, the additives used in solution methods form smooth additive-containing intermediates before the final perovskite films are developed. These intermediates can effectively control perovskite crystallization kinetics and modify the film shrinkage during the perovskite film formation process. It has been demonstrated that chlorides such as HCl, NH_4Cl, MACl, FACl, TPPCl, and 4-ABPACl play an important role in the formation of the

highly uniform film (Hwang et al., 2015), although the question whether the chloride ions enter into perovskite crystal lattices is still under hot debate. Moreover, given the use of HI, MAI, EAI, TPPI, 1,4- DIB, 1,10-DID, and DIO, it seems reasonable that iodide ion, to some extent, aids to form high-quality perovskite film. Moreover, the volatility of additives should be considered for their selection, as seen from the examples of NH4Cl, $CaCl_2$, MACl, and FACl. Lastly, in addition to DIO and CN, other additives can be employed to regulate the crystallization of perovskites film (Hwang et al., 2015). Tin fluoride (SnF_2) has also been introduced to address the following issues (Liao et al., 2016b). Although the performance of tin-based PSCs is below the lead analogue, mainly due to the uncontrollable crystallization during the solution process and tin-based perovskite film shows significant instability in its Sn^{2+} oxidation states when exposed to air. This inevitable process leads to p-type carrier doping, which limits the carrier diffusion length (Hwang et al., 2015). Therefore, it is believed that the addition of SnF_2 can increase the formation energy of tin vacancy, leading to the decreased concentration of this kind of defect and can improve the morphology (Liao et al., 2016a; Saliba et al., 2014). Recently Shuyan Shao et. al. used SnF_2 as a reducing agent in a planar p–i–n device structure, showing considerable improvement of the stability of the materials. Hence the addition of SnF_2 with appropriate concentration can enable tin-based perovskite film with full coverage and improved crystallinity and reduced carrier recombination (Saliba et al., 2014; Xiao et al., 2018).

2.8 SUMMARY

Over 100 years that organic–inorganic perovskites have been known, some highly interesting structural, magnetic, electrical, and optical properties have arisen, primarily because of distinct properties of the organic or inorganic component. In addition, the transport properties have confirmed the semiconducting nature of the perovskite compounds showing additional strong dependence upon structural changes. These structural properties strongly resemble the behaviour of the perovskite oxides by undergoing reversible, temperature-dependent phase transitions. Therefore, the entire family featured direct energy gaps spanning the range between 1.1 to 1.7 eV. This makes them highly relevant as possible light absorbers in energy conversion or detector devices. Although the organic-inorganic perovskites offer fascinating and exceptional properties suitable for photovoltaic applications, various crucial challenges such as the toxicity of Pb atoms and long-term stability still hinder their commercialization in the PV market. Yet, little progress has been achieved to replace Pb with environment-friendly

components and the improvement of the controlled morphology of the film which is dependent on the deposition technique and the annealing process. In this regard, nontoxic Sn has been successfully introduced in organometal halide perovskites and should theoretically yield higher conversion efficiency. However, due to the highly oxidizing nature of Sn (II), alloying with lead, an additive or an encapsulation technique is amongst the options needed to overcome this issue.

2.9 REFERENCES

Aharon, S., Dymshits, A., Rotem, A., Etgar, L., 2015. J. Mat. Chem A. 3, 9171-9178.

Aharon, S., Gamliel, S., Cohen, E., Etgar, L., 2014. Phys. Chem. Chem. Phys.16, 10512-10518 .

Ahmad, S., Letters, Guo X., 2018. Chinese Chemical Letters 29, 657-663.

Ansari, M., Qurashi, A., and Nazeeruddin M., 2018. Journal of Photochemistry and Photobiology C: Photochemistry Reviews 35, 1–24.

Yokoyama, T., Cao, D.H., Stoumpos, C.C., Song, T.B., Sato, Y., Aramaki, S., Kanatzidis, M.G., 2016. J. Phys. Chem. Lett. 7, 776–782

Chen, K., Schünemann, S., Song, S., Tüysüz, H. 2018, Chem. Soc. Rev. 47, 7045-7077

Chen, Q., Marco, N. De, Yang, Y., 2015. Nano Today 10, 355-396.

Chen, Y., He, M., Peng, J., Sun, Y., Liang, Z., 2016. Adv. Sci. 3, 1500392.

Chiarella, F., National, I., Zappettini, A., National, I., Cantele, G., National, I., Ninno, D., 2008. Phys. Rev. B 77, 045129

Chung, I., Lee, B., He, J., Chang, R.P.H., Kanatzidis, M.G., 2012. Nature 485, 486–489.

Cui, J., Yuan, H., Li, J., Xu, X., Shen, Y., Lin, H., Wang, M., 2015. Sci. Technol. Adv. Mater. 16, 036004.

Das, S., Yang, B., Gu, G., Joshi, P.C., Ivanov, I.N., Rouleau, C.M., Aytug, T., Geohegan, D.B., Xiao, K., 2015. ACS Photonics 2, 680–686.

Djuri, A.B., He, Z.B., 2017. Progress in Quantum Electronics 53, 1–37.

Docampo, P., Ball, J.M., Darwich, M., Eperon, G.E., Snaith, H.J., 2013. Nat. Commun. 4, 2761.

Dualeh, A., Gao, P., Seok, S. Il, Nazeeruddin, M.K., Grätzel, M., 2014. Chem. Mater. 26, 6160–6164.

Moerman, D, Eperon, GE, Precht, JT, Ginger, DS, 2017. Chem. Mater. 29, 5484–5492.

Eperon, Giles E., Ginger, D.S., 2017. ACS Energy Lett. 2, 1190–1196.

Even, J., Pedesseau, L., Jancu, J.M., Katan, C., 2014. Phys. Status Solidi - Rapid Res. Lett. 8, 31–35.

Gamliel, S., Dymshits, A., Aharon, S., Terkieltaub, E., Etgar, L., 2015. J. Phys. Chem. C 119, 19722–19728.

Grätzel, C., Today, S.Z.-M., 2013, Materials Today 16, 11-18.

Hao, F., Stoumpos, C.C., Chang, R.P.H., Kanatzidis, M.G., 2014. J. Am. Chem. Soc. 136, 8094–8099.

Hussain, I., Tran, H.P., Jaksik, J., Moore, J., Islam, N., Uddin, M.J., 2018. Emergent Mater. 1, 133–154.

Hwang, K., Jung, Y.S., Heo, Y.J., Scholes, F.H., Watkins, S.E., Subbiah, J., Jones, D.J., Kim, D.Y., Vak, D., 2015. Adv. Mater. 27, 1241–1247.

Im, J., Stoumpos, C.C., Jin, H., Freeman, A.J., Kanatzidis, M.G., 2015. J. Phys. Chem. Lett. 6, 3503–3509.

Jiang, J., Onwudinanti, C.K., Hatton, R.A., Bobbert, P.A., Tao, S., 2018. J. Phys. Chem. C 122, 17660–17667

Ju, M.G., Chen, M., Zhou, Y., Dai, J., Ma, L., Padture, N.P., Zeng, X.C., 2018. Joule 2, 1231–1241.

Jung, H.S., Park, N.G., 2015. Small 11, 10-25.

Kim, M., Im, Jino, Freeman, A.J., Ihm, Jisoon, Jin, H., Im, J, Ihm, J, Designed, H.J., Performed, H.J., 2014. Natl. Acad Sci. 111.

Kogo, A., Iwasaki, S., Ikegami, M., Miyasaka, T., 2017. Chem. Lett. 46, 530–532.

Kojima, A., Teshima, K., Shirai, Y., Miyasaka, T., 2009. J. Am. Chem. Soc. 131, 6050–6051.

Leyden M, Lee M, Raga S 2015. J. Mater. Chem. A 3, 16097-16103.

Leyden, M., Ono, L., Raga, S. et al. 2014, J. Mater. Chem. A 2, 18742-18745

Liao, W., Zhao, D., Yu, Y., Grice, C.R., Wang, C., Cimaroli, A.J., Schulz, P., Meng, W., Zhu, K., Xiong, R.-G., Yan, Y., 2016a. Adv. Mater. 28, 9333–9340.

Liao, W., Zhao, D., Yu, Y., Grice, C.R., Wang, C., Cimaroli, A.J., Schulz, P., Meng, W., Zhu, K., Xiong, R.G., Yan, Y., 2016b. Adv. Mater. 28, 9333–9340.

Liu, M., Johnston, M.B., Snaith, H.J., 2013a. Nature 501, 395–398.

Luo, P., Liu, Z., Xia, W., Yuan, C., Cheng, J., Lu, Y., 2015. ACS Appl. Mater. Interfaces 7, 2708–2714.

Luo, S., Daoud, W.A., 2015. J. Mater. Chem. A 3, 8992–9010.

Marshall K, Walker M, Walton R, Hatton R, 2016. Nat Energy 1, 16178

Mei, A., Li, X., Liu, L., Ku, Z., Liu, T., Rong, Y., Xu, M., Hu, M., Chen, J., Yang, Y., Grätzel, M., Han, H., 2014. Science 18, 295-298.

Mitzi D B, Watson I B M T J, Box P O, Heights Y and Mitzi D 2004. J. Mater. Chem. 14, 2355-2365.

Ogomi, Y., Morita, A., Tsukamoto, S., Saitho, T., Fujikawa, N., Shen, Q., Toyoda, T., Yoshino, K., Pandey, S.S., Ma, T., Hayase, S., 2014. J. Phys. Chem. Lett. 5, 1004–1011.

Park, J.H., Seo, J., Park, S., Shin, S.S., Kim, Y.C., Jeon, N.J., Shin, H.W., Ahn, T.K., Noh, J.H., Yoon, S.C., Hwang, C.S., Seok, S. Il, 2015. Adv. Mater. 27, 4013–4019.

Pazoki, M., Johansson, M.B., Zhu, H., Broqvist, P., Edvinsson, T., Boschloo, G., Johansson, E.M.J., 2016. J. Phys. Chem. C 120, 29039–29046.

Pellet, N., Gao, P., Gregori, G., Yang, T.Y., Nazeeruddin, M.K., Maier, J., Grätzel, M., 2014. Angew. Chemie - Int. Ed. 53, 3151–3157.

Ponseca, C.S., Savenije, T.J., Abdellah, M., Zheng, K., Yartsev, A., Pascher, T., Harlang, T., Chabera, P., Pullerits, T., Stepanov, A., Wolf, J.P., Sundström, V., 2014. J. Am. Chem. Soc. 136, 5189–5192.

Qing, S., Yuhei, O., Taro, T., Kenji, Y., Shuzi, H., 2016. Optical Absorption, Charge Separation and Recombination Dynamics in Pb and Sn/Pb Cocktail Perovskite Solar Cells and Their Relationships to the Photovoltaic Properties, in: Perovskite Materials - Synthesis, Characterisation, Properties, and Applications. InTech.

Randall, C.A., Newnham, R.E., Cross, L.E., 2009. History of the First Ferroelectric Oxide, BaTiO 3, ceramics.org.

Saliba M, Matsui T, Seo J 2016. Energy Environ. Sci. 9, 1989-1997.

Saliba, M., Tan, K.W., Sai, H., Moore, D.T., Scott, T., Zhang, W., Estroff, L.A., Wiesner, U., Snaith, H.J., 2014. J. Phys. Chem. C 118, 17171–17177.

Saparov, B., Mitzi, D.B., 2016. Chem. Rev. 2016, 116, 7, 4558–4596.

Shao, S., Liu, J., Portale, G., Fang, H., Blake, G.R., Brink, G.H., Koster, L.J.A., Loi, M.A., 2018. Advanced Energy Materials 8, 1702019.

Stoumpos, C.C., Malliakas, C.D., Kanatzidis, M.G., 2013. Inorg. Chem. 52, 9019–9038.

Suarez, B., Gonzalez-Pedro, V., Ripolles, T.S., Sanchez, R.S., Otero, L., Mora-Sero, I., 2014. J. Phys. Chem. Lett. 5, 1628–1635.

Sum, T.C., Mathews, N., 2014. Energy Environ. Sci. 7, 2518-2534

Tan, K.W., Moore, D.T., Saliba, M., Sai, H., Estroff, L.A., Hanrath, T., Snaith, H.J., Wiesner, U., 2014. ACS Nano 8, 4730–4739.

Tanaka H, Misono M. 2001. Current Opinion in Solid State and Materials Science 5, 381-387.

Tavakoli, M.M., Zakeeruddin, S.M., Grätzel, M., Fan, Z., 2018. Advanced Materials 30, 1705998.

Tran V, Pammi S, Dao V 2018 Journal of Alloys and Compounds 747, 703-711

Wang, Y., Yang, D., Zhou, X., Alshehri, S.M., Ahamad, T., Vadim, A., Ma, D., 2016. J. Mater. Chem. C 4, 7415.

Wells, B., 2015. Bandgap measurements of nonspecular materials using a bifurcated fiber optic method of diffuse reflectance.

White J, Liu J, Wang Y. 2019 Computational Materials Science 156, 246-251

Whitfield, P.S., Herron, N., Guise, W.E., Page, K., Cheng, Y.Q., Milas, I., Crawford, M.K., 2016. Nat. Publ. Gr. 1–16.

Xiao, M., Gu, S., Zhu, P., Tang, M., Zhu, W., Lin, R., Chen, C., Xu, W., Yu, T., Zhu, J., 2018. Adv. Opt. Mater. 6, 1700615.

Yan J, Advances B S-R, 2014. RSC Adv. 4, 43286-43314.

Yang, L., Barrows, A.T., Lidzey, D.G., 2015. Sci. Technol. Adv. Mater 16, 36004.

Yin W-J, Yang J-H, Kang J, Yan Y and Wei S-H, 2015. J. Mater. Chem. A 3, 8926-8942 Zhang, Y., Yin, J., Parida, M.R., Ahmed, G.H., Pan, J., Bakr, O.M., Brédas, J.L., Mohammed, O.F., 2017. J. Phys. Chem. Lett. 8, 3173–3177.

Zhao, B., Abdi-Jalebi, M., Tabachnyk, M., Glass, H., Kamboj, V.S., Nie, W., Pearson, A.J., Puttisong, Y., Gödel, K.C., Beere, H.E., Ritchie, D.A., Mohite, A.D., Dutton, S.E., Friend, R.H., Sadhanala, A., 2017. Adv. Mater. 29, 1604744.

Zhou H, Chen Q, Li G, Luo S, Song T 2014, Science 345, 542-546

Zuo, F., Williams, S.T., Liang, P.W., Chueh, C.C., Liao, C.Y., Jen, A.K.Y., 2014. Adv. Mater. 26, 6454–6460.

CHAPTER 3

SAMPLE PREPARATION AND CHARACTERISATION TECHNIQUES

3.1 INTRODUCTION

This chapter aims to give details of the methods used to prepare samples for the deposition of a Pb-Sn binary perovskite which is sequentially chemical vapour deposited and to describe the growth mechanism. Furthermore, we will be discussing in detail the different analytical techniques used to characterize the Pb-Sn binary perovskite absorber layer.

3.2 DEPOSITION METHODS

Numerous schemes can be devised to categorize coating processes, none of which are very satisfactory since several processes will overlap different categories. For example, Chapman and Anderson provided a list and definitions of various deposition processes including the Conduction and Diffusion processes, Chemical processes, Wetting processes, and Spraying processes (Bunshah, 1994). Here, the Chemical Vapour Deposition process falls under the chemical processes, and the Physical Vapour Deposition Process (Evaporation, etc.) falls under the spraying processes or the way around. Hence, they were used to deposit sequentially the alloy Pb-Sn and the methyl-ammonium iodide to form perovskite thin film.

3.2.1 CHEMICAL VAPOUR DEPOSITION

First developed in 1880, as stated in the pioneering work of Powell, Oxley, and Blocher, Chemical vapour deposition (CVD) is not a new process. Its practical use was in the production of incandescent lamps to improve the strength of filaments by coating them with carbon or metal and after, the carbonyl process was developed by Ludwig Mond and others for the production of pure nickel (Hugh O. Pierson 1999). CVD is a process whereby a solid material

is deposited from vapour on a heated substrate. The solid material is obtained as a coating, a powder, or as single crystals. By varying the experimental conditions—substrate material, substrate temperature, the composition of the reaction gas mixture, total pressure gas flows, etc.—materials with different properties can be grown (Bunshah, 1994). A characteristic feature of the CVD technique is its excellent throwing power, enabling the production of coatings of uniform thickness and properties with a low porosity even on substrates of complex shape. Another characteristic feature is the possibility of localized, or selective deposition, on patterned substrates. It is therefore employed in many thin-film applications (Bunshah, 1994; Hugh O. Pierson 1999). Some of the CVD applications are the preparation of high-temperature materials (tungsten, ceramics, etc.) and the production of solar cells, with high-temperature fibre composites, as well as particles of well-defined sizes. The term CVD was introduced to distinguish from other evaporation techniques like physical vapour deposition (PVD) in the sixties. Since then a variety of other vapour deposition processes were developed such as Thermal CVD, Plasma assisted/Plasma enhanced chemical vapour deposition (PACVD/PECVD), Metal-organic chemical vapour deposition (MOCVD), Laser chemical vapour deposition (LCVD), Photochemical vapour deposition (PCVD), Chemical vapour infiltration (CVI), and Chemical beam epitaxy (CBE) (Hugh O. Pierson 1999).

The thermal chemical vapour deposition (TCVD) is described as a process in which energy necessary is applied to activate the chemical vapour deposition reaction. Generally, thermal CVD requires high temperature in the range of 800 ºC - 2000 ºC, generating by high-frequency induction, resistance, and a hot plate or radiant heating or maybe a combination of them. Thermal CVD comprises two basic systems: the hot-wall reactor and cold-wall reactor. The hot-wall reactor is an isothermal furnace often heated by resistance elements. In this process, where the substrate is loaded inside the reactor, and the carrier gas may be introduced in a case of a deposition- or coating, and the temperature is monitored at the desired level. As the deposition occurs in the chamber on the wall inside, which often necessitates the cleaning of the chamber. The cold-wall reactor, in contrast, remains cooler. The principle is called endothermic, and only the substrate is heated by the phenomena of induction or radiant heating, and unlike in the hot-wall, here the deposition is localized and the chamber remains cleaned (Hugh O. Pierson 1999).

Metallo-organic chemical vapour deposition (MOCVD) is used to deposit indium phosphide and indium antimonide. It demonstrated that the deposition of critical semiconductor materials could be obtained at a lower temperature than conventional thermal CVD and that epitaxial

growth could be successfully achieved. But nowadays, MOCVD is used on a large scale, particularly in the semiconductor and optoelectronic applications(Hugh O. Pierson 1999). However, the equipment and chemicals used in MOCVD are indeed all available commercially but are expensive. It is therefore considered in applications where high quality is essential.

Laser chemical vapour deposition (LCVD) is based on photon activation, which produces a coherent and monochromatic high-energy beam of photon capable of activating a reaction in a CVD. The process occurs because of the thermal energy from the laser beam which heats the absorbing substrate by coming directly in contact with it. The laser wavelength is so small to the point that less energy is absorbed by the gas molecules. As in a cold-wall reactor, the substrate is locally heated, and the deposition is limited to the heating area. Though the mechanism is almost the same. While photochemical CVD is a chemical reaction of photo CVD activated by the action of photons as in laser CVD. However, the energy required must be enough to break the chemical bonds in the atoms or molecules. The radiation used is mainly ultraviolet (UV). The UV radiation easily excites the compounds which have a large electronic absorption band. The deposition in photochemical CVD can occur at room temperature, for it does not require any heat. There is no limitation on the kind of substrate (opaque, absorbent, or transparent). However, photochemical CVD has a low rate deposition which often restricts some applications (Hugh O. Pierson 1999).

Plasma-enhanced chemical vapour deposition (PECVD): was developed for the deposition of silicon nitride. PECVD has significantly expanded the number of applications since then. Also called plasma-assisted-CVD, the reaction process is activated by plasma and the deposition temperature is substantially lower. A convenient way of obtaining plasma is with electrical energy by lowering the frequency discharge and increasing the electrical energy in a fixed amount of gas. This eventually allows molecules to disassociate, and a complete ionization can be achieved. For example, a diatomic gas of hydrogen can be heated above a given temperature, and molecules are disassociated into atoms ($H_2 \rightarrow 2H$). By so doing, most of the atoms become ionized and are stripped of their electrons. The plasma is then formed, consisting of ions positively charged and electrons negatively charged and maybe non-ionized atoms neutral. Moreover, a great amount of thermal energy is required (>5000K) for ionization (Hugh O. Pierson 1999). It is classified into two types: glow-discharge plasma (non-isothermal) which is generated in a gas by a high-frequency electric field, such as microwave (2.45 GHz) which operates at a lower frequency (1 MHz). Therefore, the electrons and ions require both energy and high temperature.

Chemical vapour infiltration (CVI) is a process in which gaseous reactants infiltrate a porous structure which in turn, acts as a substrate and can either be an inorganic open foam, a fibrous material, or a weave. The deposition occurs on the fibre or foam by slowly solidifying to form a composite. The reactants must inwardly diffuse through the porous structure, whereas the by-products must outwardly diffuse. However, CVI operates at low pressure and high temperatures than required, the potential damage is considerably reduced for the sintering of ceramics or the melting of metals. But the disadvantage of CVI is the necessity of inter-diffusion of reactants and reaction products through relatively long, narrow, and tortuous channels (Hugh O. Pierson 1999).

3.2.2 SELECTION OF TCVD

Unlike many other deposition methods, TCVD is a dynamic technology that is expanding in countless of applications not only in the research field but also in the industrial. Nowadays the applications are mostly developed in the semiconductor and optical industry in the manufacturing of electronic components as well as in the metallurgical-coating industry and others. In the photovoltaic domain, the choice is made on important following factors: Cost-effective, reproducibility, the capability of scaling up, type of the substrate, nature of the chemical (powder) to deposit, adhesion of layers on the substrate as well as the possibility to control the morphology of the film.

3.2.3 THE TCVD 3-ZONE FURNACE SYSTEM

The thermal chemical vapour deposition system used during the growth of Pb-Sn methyl-ammonium iodide was an XD 1600MT 3-zone tube furnace system and manufactured by Zhengzhou Brother Furnace Co.LTD. A schematic diagram is shown in Fig3.1 (a).

The XD 1600MT 3-zone tube furnace is made up of double-layer steel and has a three-fan cooling system that maintains the set temperature and furnace surface at a lower temperature than inside the chamber. The system consists of three different box-shaped heating chambers/zones, and each zone is 20x20x20 cm long which is separated by an insulating material of 4 cm thick.

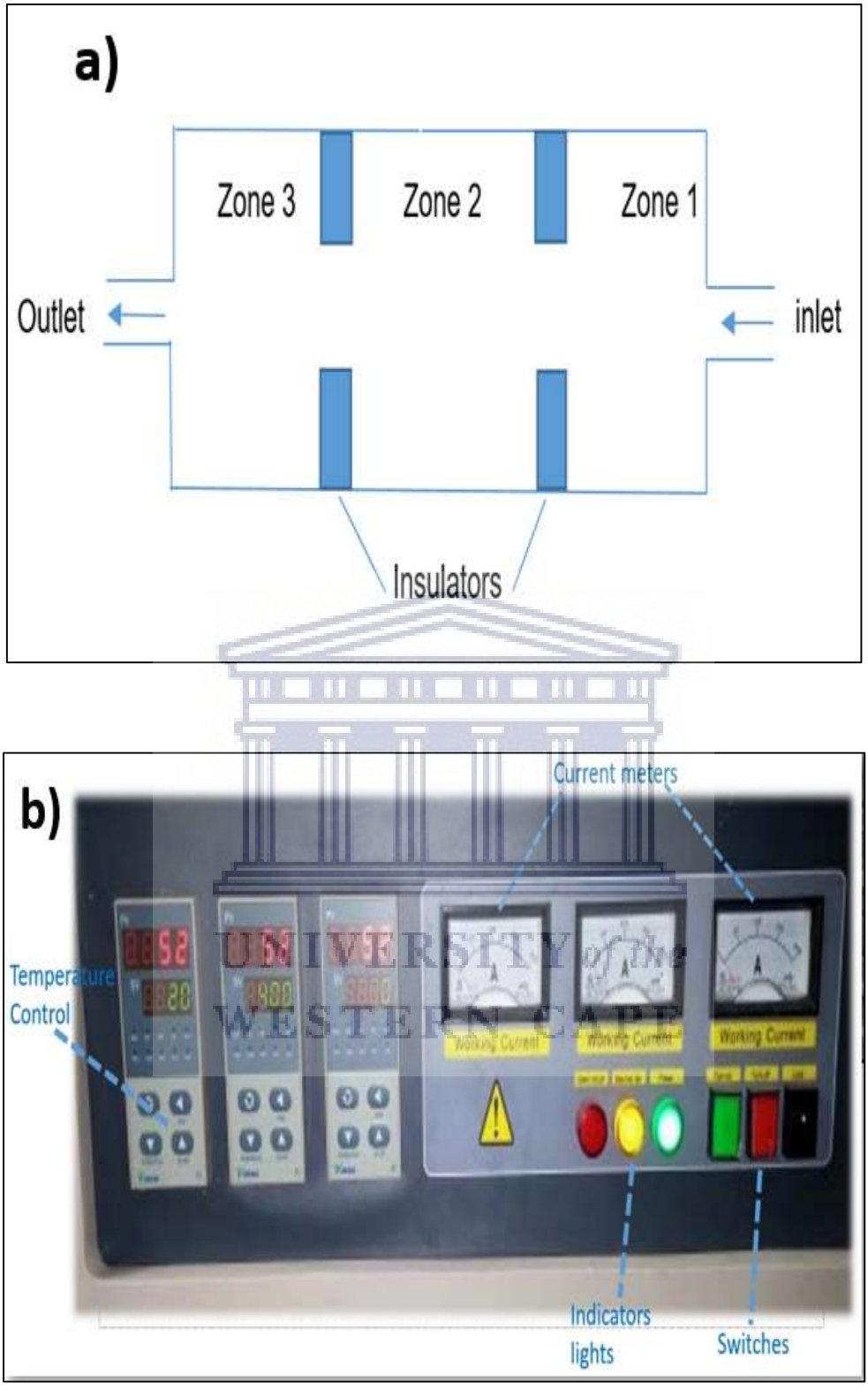

Figure 3. 1: (a) The schematic diagram of the XD-1600MT, and (b) photographic image of the temperature control and display.

The temperature inside each heating zone is monitored using the thermocouple. The current temperature is shown in the 708P temperature control display system alongside the set

temperature (SV) for each zone as shown in Fig3.1(b). Additionally, the system has a ceramic tube 120cm long with an external and internal diameter of respectively 6 cm and 5 cm. A gas-flow meter on the gas intake side was used to adjust the gas flow in the system. The gas flow in the system was regulated using a gas-flow meter mounted on the gas intake side. As the Vacuum system is not included, the KF25 Flexible Vacuum hose of two stainless steel flanges with the vacuum gauge and valves are adapted and installed. For easy operation, the system was mounted on a wooden top trolley. The 3-zone XD-1600MT tube furnace is a high precision bench-top furnace that utilizes high-quality ceramic rods and high resistance wires as heating elements. The maximum achievable operating temperature inside the tube furnace under vacuum or with the gas flow is 1600 °C and the temperature profile can be set up by 30 segments and run automatically by the 708P advanced temperature controller. The temperature accuracy of the controller is about ± 1 °C making the system ideal for various materials research to develop new materials. The technical specifications and operating conditions of the system are summarised in Table 3.1 (Sfiso zwelisha khanyile, 2015)

Table 3.1: Technical specifications of the XD-1600MT tube furnace

Name	**Units**	**Parameters**
Working power	KW	9 KW
Voltage	V	AC 380V, 50 Hz, 3 phases
Max. Temperature	°C	1600 °C
Continuous working temperature	°C	1500 °C
Heating rate	°C	< 10 °C
Heating element	--	MoSi2 heater
Connection of heating element	--	Series connection
Thermal couple heat capacity inside	--	B type
The dimension of the inside chamber	Mm	Dia 60x200x200x200
Net weight	Kg	165

3.2.4 FACTORS CONTROLLING CVD PROCESS

The deposition of thin film using the CVD process can be controlled by adjusting the following parameters: the pressure, temperature, gas flow rate, substrate position and temperature, deposition time as well as the exhaustion system. **The pressure** controls the thickness of the boundary layer, therefore the degree of diffusion. It dictates the mean free path. By lowering the pressure, the surface kinetics can regulate the deposition rate and the diffusion process can be minimized as well. **The temperature** is a crucial parameter since it can directly affect the rate at which the source powder is vaporized. It is relatively high since most of the reactants are solid at room temperature and must be heated to evaporate. **Gas flow rate** contributes to the transport of material from one spot to the other. **The substrate position** and **substrate temperature** help to control the morphology of the film. It must be distinguished from the insulators or the zones. Too close or too far from the source may prevent it from heating at the same temperature as the source and regulate the amount of material being depositing. **The deposition time** allows controlling the thickness or amount of the material needed**. The exhaustion system** helps to pull out the undesirable molecules in the reaction (Hugh O. Pierson, 1999; Mattox, 2010)

3.2.5 TCVD OPERATORY MODE

In the laboratory, the XD-1600MT TCVD furnace is used during the deposition of PbI_2/ MAI film and was powered using an AC 380 V, 50 Hz, 3 phase power supply. The end of the tube furnace was connected to the nitrogen (N) gas supply by the N gas flow meter and flanges, whereas the other end related to an exhaust tube, to exhaust the N which is used as a carrier gas. The substrates samples are placed on a flat horizontal sample holder and then loaded into the ceramic tube furnace by opening the flange on the intake side and pushing them into the tube using a calibrated metal rod such that they are 53 cm into the tube. The depth of the metal rod into the tube indicates the position of the samples along the tube relative to the zone dimensions which can be linked to the temperature calibration study of the furnace. A schematic representation of the TCVD set up is shown below (Fig3.2).

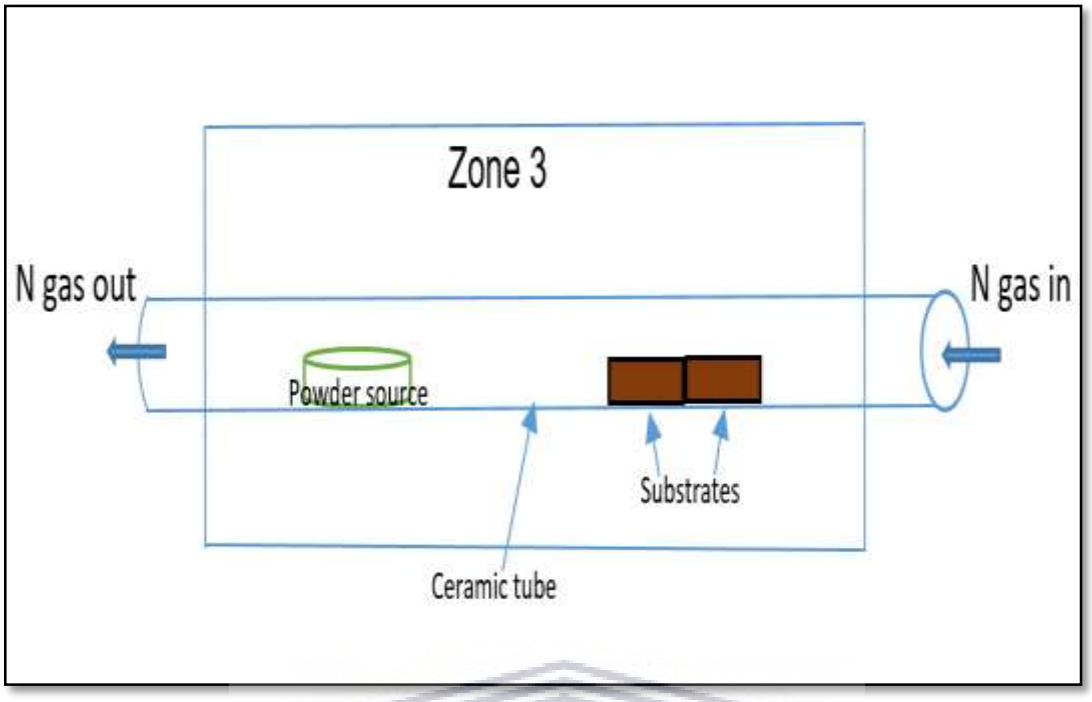

Figure 3. 2: Schematic representation of the set up in a typical TCVD.

A source is placed in a ceramic boat and placed at a specific position (about 39 cm in the tube). where it is heated to its vaporization temperature. Based on their geometry, the effective distance between the substrate holder and the source ceramic boat was found to be 7 cm. After loading the samples, the connecting flange is restored, and the system is purged with a high flowing N gas (100 cm3 /min) before heating the system. The system is then switched on after loading the samples, and a temperature profile is created through the 708P temperature control interface (Fig 3.1 a). During segmented heating up, the system is heated at a steady rate of 10 °C per minute from room temperature to the deposition temperature—360 °C in our case (Sfiso zwelisha khanyile, 2015), then the system is allowed to stabilize. It is programmed to remain at this temperature for the entire deposition time. After, it automatically starts cooling down until room temperature. During this automatic heating up and cooling, the N gas flow in the system is maintained at the 100 cm3 /min. After cooling down, the samples are removed from the system for characterization.

3.3 VACUUM EVAPORATION OF TIN (Sn)

Vacuum evaporation or vacuum deposition vacuum deposition is a vapour deposition process like CVD, but in a vacuum where the process occurs in a chamber by thermally vaporizing atoms or molecules source, and which reach the substrate without colliding with residual molecules in the process. This process is also called physical vapour deposition (PVD) because there are no chemical reactions. Therefore, the difference with CVD is that, in PVD, the deposition is by condensation—and exothermic, whereas in CVD the deposition occurs by chemical reaction, usually endothermic (Mattox, 2010). It was used by Edison to evacuate the carbon-filament incandescent lamps, and later Nahrwold performed the first vacuum evaporation, for the deposition of metallic thin films (Mattox, 2010). Since then, this technique has extensively been used to produce thin films. In essence, a vacuum evaporation system requires a better vacuum, to prevent undesirable potential residual gases on the substrate that may contaminate the film.

The principle of evaporation is relatively simple. The coating element also known as the source is heated at low pressure (less 10^{-3} Pa) and above its boiling point. The atoms or molecules are sent through a cosine distribution of trajectories in a straight line to the substrate (as it is shown in Figure 3.3.), where they are condensed to form a thin layer. The mean-free path is large in comparison to the distance between the source and substrate at low pressure and few collisions occur before the species condense on the substrate. The method used to evaporate the source material was resistance heating. The tin (Sn) source powder evaporated (in our case) was put on a hot surface of a metal holder that is heated by passing a current through—also known as resistively heated.

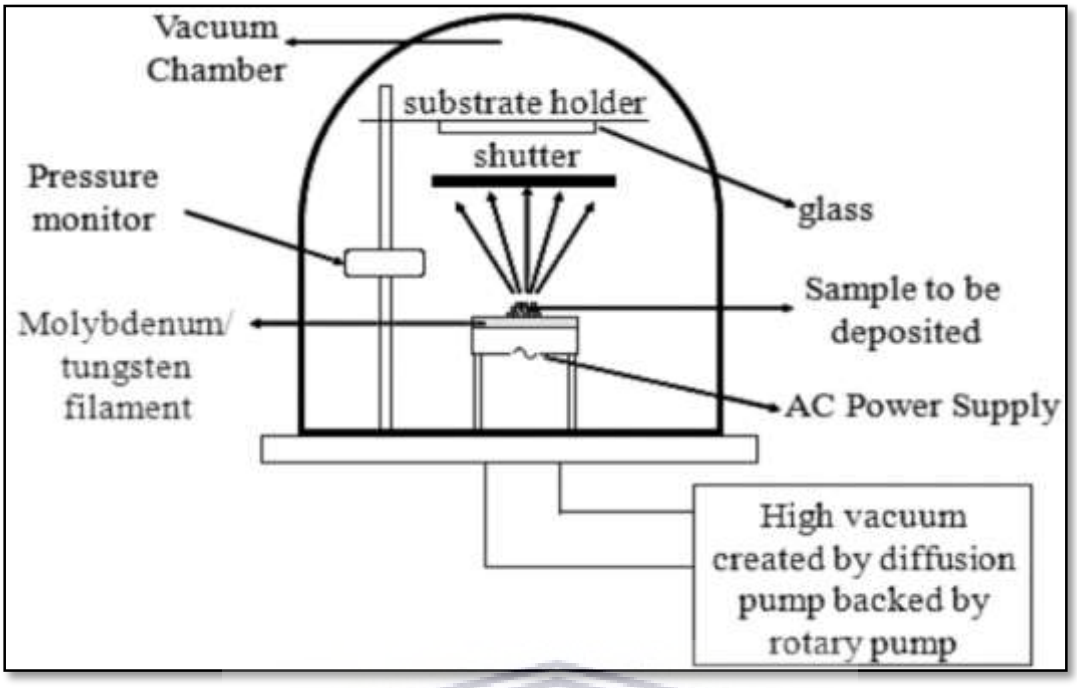

Figure 3. 3: Schematic representation of the thermal evaporator.

3.3.1 FACTORS CONTROLLING VACUUM EVAPORATION

The factors controlling the vacuum evaporation are the deposition pressure, deposition time, deposition rate, current, as well as the tooling factor. As in CVD, the deposition pressure is a mean free path, therefore it controls the degree of diffusion. Furthermore, the deposition time allows us to stop the deposition when the desired thickness is reached. Another factor is the deposition rate, which regulates the amount of the material being deposited. Conversely, input such as current, is an important factor in PVD, because it monitors the evaporation temperature of the material. While the tooling factor is a correction needed between the thickness of the layer deposited on the crystal monitor and the thickness of the film deposited on the substrate. The tooling factor depends factor depends on the geometry of the chamber, substrate position, the position of the crystal monitor, and the material deposited (Bunshah, 1994; Mattox, 2010).

3.4 SAMPLES PREPARATION PROCEDURE

The thin film of methyl-ammonium metal iodide $CH_3NH_3Pb_{1-x}Sn_xI_3$ perovskite was made in two sequential depositions of (1) Lead-tin iodide $(Pb\text{-}Sn)I_2$ and (2) converted to perovskite by evaporation of methyl-ammonium iodide (CH_3NH_3I).

A thermal CVD system at the University of the Western Cape (UWC), Department of Physics and Astronomy was used to deposit a perovskite $CH_3NH_3Pb_{1-x}Sn_xI_3$ thin films. Samples were prepared by cutting the glass substrate into 1cm x 1cm. The substrates were then carefully numbered on the backside to distinguish them from each other. A clean substrate surface free from oxides and other contaminants is a prerequisite condition for good adhesion. Therefore, glass substrates were rinsed with deionized water and subsequently bathed in acetone (*for 10 minutes*) and isopropanol (*10 minutes)* inside an ultrasonic. They were then dried by blowing them with nitrogen. The surface of the sample becomes completely free of all kinds of organic impurities and dust particles. The substrates were then mounted onto a ceramic boat of the three-zone TCVD furnace which was placed horizontally, then loaded inside the CVD furnace chamber. Before heating, the system was purged with high flowing nitrogen gas for 10 minutes to provide an inert growth environment. Then 20 mg of a 99% pure lead iodide (PbI_2) powder from Aldrich was placed in a ceramic holder, and then loaded inside the furnace chamber of TCVD and placed at a 39 cm into the tube, where it is heated. The PbI_2 thin film was deposited on many substrates, and the film thickness was monitored by varying the time such that whenever the desired film thickness was reached, the system will stop the process via a thickness crystal monitor. The pressure and the temperature were kept at $3x10^{-2}$ mbar and 360˚C, respectively. The carrier gas nitrogen flow rate was kept at 100 Sccm and the experiment was carried out. After the deposition, the system was cooled down to the room temperature and the substrates coated of PbI_2 were taken out. Moreover, the film thicknesses were confirmed by mechanical profile-meter measurements. Furthermore, these samples were then taken into the thermal evaporation system to be coated with an Sn thin layer of different thicknesses (see Table 3.2). The deposition was conducted by evaporation of Sn powder under vacuum to minimize any contamination. A resistively heated filament of thermal evaporation chamber was used to heat a metal--Sn on a boat. At a high vacuum, the vapor materials reach the substrate without reacting with or scattering against other gas-phase atoms in the chamber. The film thickness is monitored by a crystal monitor, which allows the system to display the thickness being deposited. The deposition parameters were such that the deposition rate and pressure, were approximately 0.5 angstroms/second and $2.5x10^{-5}$ mbar, respectively. The current was set around 75 Amps, and the experiment time was dependent on the desired thickness (Table 3.2).

Table 3.2: Deposition parameters of Perovskite thin film

MATERIAL	Temperature (Tº)	Pressure (mbar)	Time (min)	Current (Amps)	Flow rate (Sccm)
PbI_2	360 º C	$3x10^{-2}$	20		100
Sn		$2.5x10^{-5}$	4.4; 6.3; 9.20	70-75	Vacuum
CH_3NH_3I	190 º C	$3x10^{-2}$	60		100

Then the obtained films of Sn/PbI_2 were annealed to form an alloy. To completely fuse Sn-PbI layers, the samples were heated in a nitrogen ambient to avoid contamination at 220˚C for one-hour (1h) annealing. Finally, methyl-ammonium (CH_3NH_3I) was evaporated for the conversion of the perovskite compound using TCVD. The perovskite film was formed as a result of the reaction between an $(Sn/Pb)I_2$ metal iodide and CH_3NH_3I methylammonium iodide inside a furnace under nitrogen atmosphere. The parameters investigated during the growth of perovskite conversion are summarized in Table 3.2 and Table 3.3, and they were chosen based on previous successful perovskite synthesis by our group and are to be considered as the standard conditions unless otherwise stated.

Table 3. 3: Summary of the thickness dimensions.

Materials	PbI_2	Sn	$CH_3NH_3Pb_{1-x}Sn_xI_3$	$CH_3NH_3PbI_3$	$CH_3NH_3SnI_3$
Thickness (nm)	100	20 **(A1)**	240 **(S1)**	300	250
	100	35 **(A2)**	255 **(S2)**		
	100	85 **(A3)**	360 **(S3)**		

3.4.1 FORMATION OF (Sn-Pb)I_2 AND $CH_3NH_3Pb_{1-x}Sn_xI_3$

During the two-step synthesis of PbI_2 and CH_3NH_3I through TCVD, firstly the metal nanoparticles are deposited in a form of vapour. Then the organic CH_3NH_3I is fused in metal iodide also in the form of vapour.

The formation of nuclei deposited on the substrate has higher electronic activity than the substrate atoms, hence the substrate constantly supplies electrons for (Pb+ 2I-) which subsequently results in the formation of PbI_2 nucleates. Furthermore, the Sn is deposited on the coated PbI_2 film in the same process equation (2). Simultaneously, the substrate underneath the Sn-PbI_2 begins to be oxidized due to O from H_2O molecules as an oxidant in the atmosphere, since the Sn easily oxidizes to tin dioxide (SnO_2). The obtained film goes to the annealing (equation (3)) process, resulting in equation (2) and (3). After the formation of the alloy Sn-PbI_2 alloy (product Eq3), the CH_3NH_3I is evaporated on the film-coated Sn/PbI_2 under the nitrogen atmosphere. And the reaction is shown in the equation (4), (5), and (6).

- PbI_2 (s) $\overset{360℃}{=}$ PbI_2 (g) (1)
- $PbI_2 + Sn + O_2 = PbO_2 + SnI_2$ (2)
- $PbO_2 + SnI_2 \overset{220℃}{=} PbSnI_4 + O_2$, (3)

The obtained $PbSnI_4$ is equivalent to $Pb_{0.5}Sn_{0.5}I_2$ or $Pb_{(1-x)}Sn_xI_2$ and can also be written $PbSnI_2$ (Leijtens et al., 2017). Then perovskite films are formed as a result of these following equations:

- $PbI_2 + CH_3NH_3I \rightarrow CH_3NH_3PbI_3$ (4)
- $Sn + 3CH_3NH_3I \rightarrow CH_3NH_3SnI_3 + 2CH_3NH_2 + H_2$ (Tavakoli et al., 2018). (5)
- $Pb_{(1-x)}Sn_xI_2 + CH_3NH_3I \rightarrow CH_3NH_3Pb_{(1-x)}Sn_xI_3$ (6)

3.5 SAMPLES CHARACTERIZATION TECHNIQUES

Samples were characterised using X-ray diffraction (XRD), Rutherford backscattering spectrometry (RBS), mechanical profile-meter, scanning electron microscope (SEM), Energy-dispersive X-ray spectroscopy (EDS), ultra-violet visible spectroscopy (UV-vis).

3.5.1 X-RAY DIFFRACTION-XRD

X-ray diffraction (XRD) is a non-destructive process that provides detailed information on the structure, crystal orientation, and spacing between atomic planes of particles and thin films. X-rays are electromagnetic radiation like light, but with smaller wavelengths. They are generated by an x-ray tube in a vacuum. The tube uses a high voltage to accelerate electrons released by a hot cathode at a high velocity. The electrons produced, collide with a metal target at the anode, creating x-rays (Vinila et al., 2014; Wagner, 1978). When a monochromatic beam of X-ray photons falls onto a given specimen three basic phenomena may result, namely, absorption, scatter, or fluorescence. The coherently scattered photons may undergo subsequent interference leading in turn to the generation of diffraction maxima. These three basic phenomena form the bases of three important X-ray methods such as the absorption technique, which is the basis of radiographic analysis; the scattering effect, which is the basis of X-ray diffraction; and the fluorescence effect, which is the basis of XRF spectrometry ("Ron Jenkins, 2012.). The focus here is on scatter and fluorescence. Because the fluorescence and diffraction techniques are to a certain extent complementary since one allows accurate quantitation of elements to be made and the other allows qualitative and semi-quantitative estimations in a way in which the matrix elements are combined to make up the phases in the specimen. Thus, a combination of the two techniques will often allow the accurate determination of the material balance of a sample. When a high-energy electron beam is an incident upon a specimen, one of the products of the interaction is an emission of a broad-wavelength band of radiation called continuum, also referred to as white radiation or bremsstrahlung. The white radiation is produced as the impinging high-energy electrons are decelerated by the atomic electrons of the elements (specimen). The intensity/wavelength distribution of this radiation is typified by a minimum wavelength (λ_{mini}) which is inversely proportional to the maximum accelerating potential (V) of the electrons. It worth noting that not all vacancies result in the production of characteristic X-ray photons since there is a competing internal rearrangement process known as the Auger effect (Ron Jenkins, 2012.). The ratio of the number of vacancies resulting in the production of characteristic X-ray photons to the total number of vacancies created in the excitation process is called the fluorescent yield. Fluorescent yield values are several orders of magnitude less for the very low atomic numbers (Ron Jenkins, 2012). Nevertheless, diffraction is a phenomenon that occurs when waves interfere with a structure whose repeat distance is about the same as that of the incident wavelength. During these interactions, constructive and destructive interference patterns are formed because of the scattering of the incoming wave

fronts by the structure of the material. The wavelength range of x-rays is close to the interatomic spacing found in three-dimensional crystalline structures, meaning that x-rays can be diffracted by these crystalline structures with each atom in the crystalline structure serving as scattering centres for the incoming wave fronts (Madiba,2012). Since XRD is only sensitive to crystalline structures, it can, therefore, be applied for both homogeneous and inhomogeneous samples, which is suitable for the structural characterization of nanomaterials such as $CH_3NH_3Pb_{1-x}Sn_xI_3$.

3.5.1.1 THEORY OF X-RAY DIFFRACTION

The arrangement of atoms in materials can be either random, making the material amorphous or be arranged in a three-dimensional periodic pattern resulting in a crystalline material.

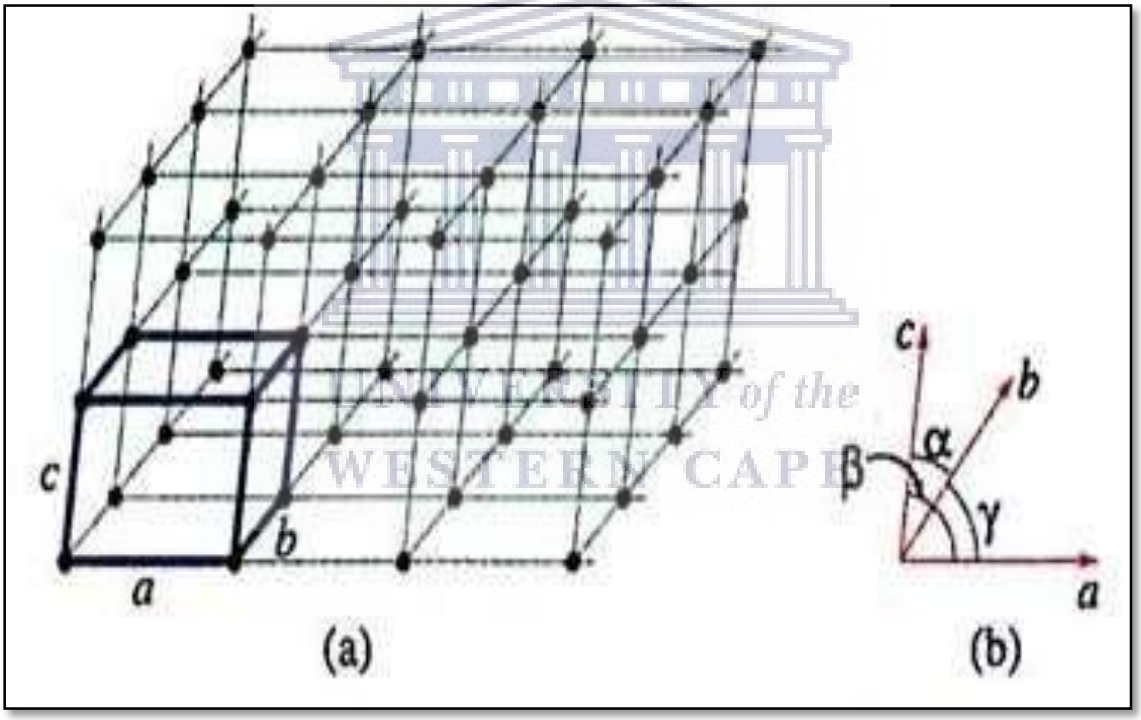

Figure 3. 4: (a) three-dimensional crystal lattice. The unit cell is shown in bold line. (b) The angles between the translation vectors (<https://opentextbc.ca/chemistry/chapter/10-6-lattice-structures-incrystalline-solids>).

The arranged atoms in a crystal are a series of imaginary points with a fixed relation in space as Figure 3.4 shows the above concept, and known as a point lattice, which is characterized as a sequence of space points, arranged identically (Cullity, 1978).

The three vectors, $\vec{a}$, $\vec{b}$, $\vec{c}$ are drawn from the corner of any lattice point and formed the unit cell. Such vectors are known as the unit cell crystallography but can also be defined in terms of lengths (**a, b**, and **c**) and angles (**α, β**, and **ɣ**) between them as shown in Figure 3.4. Moreover, the unit cell is not just defined by the crystallographic axes but can also be defined by the entire point lattice which can be generated by a repeated vector action, depending on the relation of the lattice parameters.

Table 3.4: Description of the fourteen Bravais lattices.

Crystal Systems	**Axial length and angles**	**Bravais lattice**
Cubic	Three equal axis at right angles a a= b = c, α = β = γ = 90°	Simple Body-centred Face-centred
Tetragonal	Three angles at right angles, two equal a = b = c, α = β = γ = 90°	Simple Body-centred
Orthorhombic	Three unequal axis at right angles a ≠ b ≠ c, α = β = γ = 90°	Simple Body-centred Face-centred Base-centred
Rhombohedral	Three equal axes, equally Inclined a = b = c, α = β = γ ≠ 90°	Simple
Hexagonal	Two equal co-planar axes at 120°, third axis at right angles a = b ≠ c, α = β = 90°, γ = 120°	Simple
Monoclinic	Three unequal axes, one pair not at right angles a ≠ b ≠ c, α = γ= 90°≠ β	Simple Base-centred
Triclinic	Three unequal axes, unequally inclined and none at right angles a ≠ b ≠ c, α ≠ β ≠ γ ≠ 90°	Simple

There are fourteen different types of points also called Bravais lattices as shown in Table 3.4 (Cullity, 1978). It is worth noted that in a Bravais lattice, the direction of any vector can be defined using a linear combination of the three crystallographic axes such that:

$$\vec{x} = u\vec{a} + v\vec{b} + w\vec{c} \qquad Eq.3.1$$

Where **a**, **b**, and **c** are vectors in the Bravais lattice, and (***u, v, w***) are the coordinates of a point on the vector.

3.5.1.2 BRAGG'S LAW AND THE CRYSTALLITE SIZE

The x-ray diffraction is described by the Bragg equation, which is defined by the reflection of the incident beam from the lattice planes.

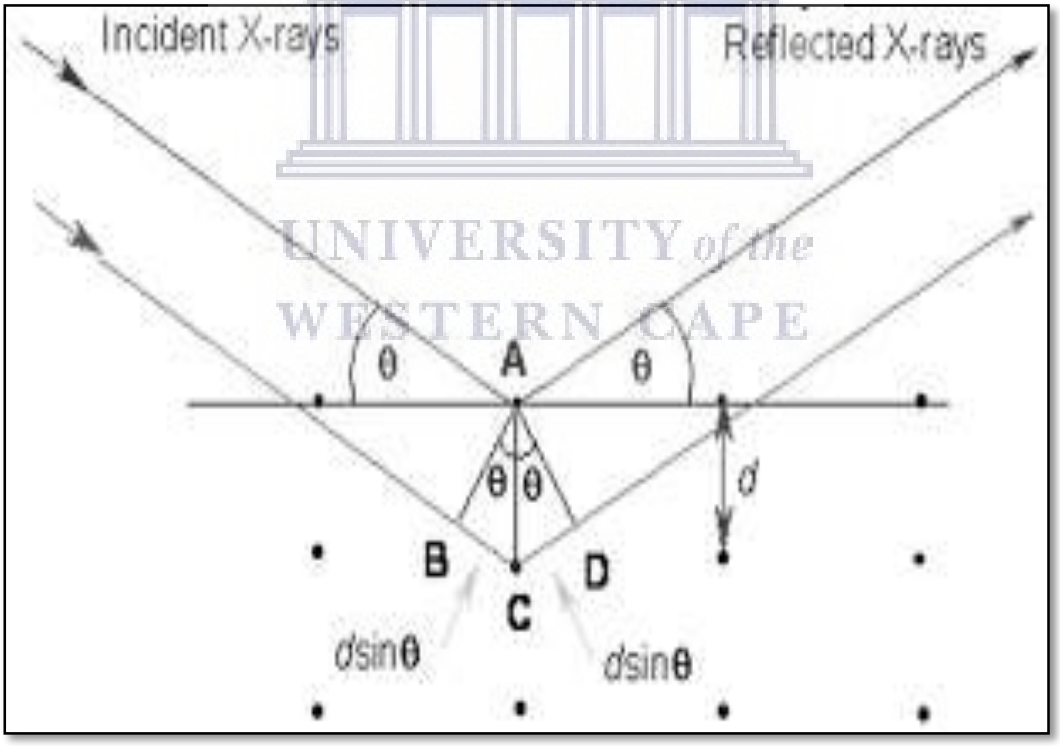

Figure 3. 5: Schematic depiction of the condition of reflection for Bragg's law (Lufaso Michael, 2019).

The Braggs equation is developed as a mathematical equation for the condition of reflection, which is equivalent to simultaneously solving Laue equations. This provides for a simpler and

more workable expression of diffraction (Ron Jenkins, 2012), stated as follows: The wavelength of the incident light has to be on the same order as the spacing of the atoms, and the reflection of X-rays only occurs when the conditions for constructive interference are fulfilled. Figure 3.5 depicts the condition of reflection for Bragg's angle.

The difference in path length$= BC + CD$, with $BC = CD =$ d sin θ

Thus, the difference in path length: $\boldsymbol{l = 2d\sin\theta}$ $\boldsymbol{Eq.3.2}$

Therefore, it must be an integral number of wavelengths: $\boldsymbol{n\lambda = 2\,d\sin\theta}$ $\boldsymbol{Eq.3.3}$

and n = 1, 2, 3, etc.

Hence Bragg's law:

$$\boldsymbol{2\,d_{hkl}\sin\theta = n\lambda} \qquad \boldsymbol{Eq.3.4}$$

The equation gives the angle θ, whereby a set of planes of d-spacing constructively reflects x-radiation of wavelength λ in the n^{th} order. The inter-planar d-spacing is defined by dimensions of the crystal unit cell. Additionally, in any given crystalline lattice there is an infinite number of families of parallel planes, and each family is associated with a Bragg angle θ. These planes are characterized by the three Miller indices ***(hkl)***, and the resultant diffracted beam is termed the ***(hkl)*** miller indices (Thinavhuyo Ramashia, 2015). Similarly, this law relates the X-rays wavelength to the diffraction angle and the d-spacing lattice in a crystalline sample. The diffracted X-rays are then detected, processed, and counted. When scanning the sample at a range of 2θ angles, the random orientation of the powdered material would ensure that all possible diffraction directions of the lattice are achieved. The conversion of the diffraction peaks to d-spacing allows identification of the phases because each material has a set of unique d-spacing. The other feature to consider is how diffraction peaks are affected by different defects, such as a small number of dislocations in crystals. The diffraction peaks are noted to be influenced by the presence of several different defect forms such as small numbers of crystal dislocations with micro-metre sizes. The grain size can be regarded as a different type of defect and the peak diffraction width may be altered. And thus, the crystallite size is determined by the peak width— full-width at half-maximum peak intensity (FWHM), peak position, and wavelength, using the well-known Scherer's equation (Soussi et al., 2020):

$$D = \frac{K\lambda}{\beta(2\theta)\cos\theta} \qquad Eq.\ 3.5$$

Where β is the FWHM; θ angle; λ a wavelength, and k is a constant dependent of the shape of the crystallite.

3.5.1.3 EXPERIMENTAL SET-UP

X-ray diffractometers consist of three basic elements: An X-ray tube, a sample holder, and an X-ray detector. X-rays are generated in a cathode ray tube by heating a filament to produce electrons, accelerating the electrons toward a target by applying a voltage, and bombarding the target material with electrons. The X-ray spectra produced, consist of several components, the most common being Kα and Kβ. K consists of K 1 (slightly shorter wavelength and twice the intensity) and K 2. The specific wavelengths are characteristic of the target material (Cu, Fe, Mo, Cr) (Cullity, 1978). K 1 and K 2 are sufficiently close in wavelength such that a weighted average of the two is used. Copper is the most common target material for single-crystal diffraction, with CuK radiation = 1.5418Å. These X-rays are collimated and directed onto the sample. As the sample and detector are rotated, the intensity of the reflected X-rays is recorded. A detector records and processes this X-ray signal and converts the signal to a count rate which is then output to a device such as a printer or a computer monitor. The geometry of an X-ray diffractometer is such that the sample rotates in the path of the collimated X-ray beam at an angle θ while the X-ray detector is mounted on an arm to collect the diffracted X-rays and rotates at an angle of 2θ (see Fig 3.6). The instrument used to maintain the angle and rotate the sample is termed a goniometer (Madiba, 2012).

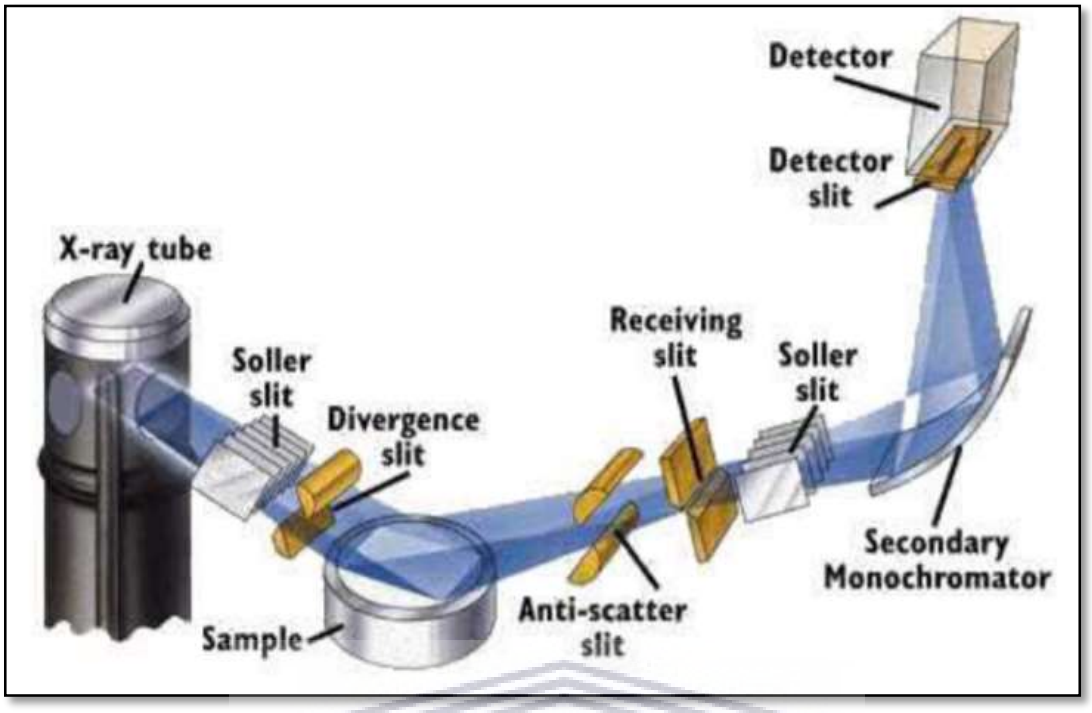

Figure 3. 6: Schematic illustration of an x-ray diffractometer of an x-ray diffractometer (Lufaso Micheal, 2019).

3.5.2 RUTHERFORD BACKSCATTERING SPECTROMETRY

Rutherford backscattering spectrometry (RBS) is generally referred to as high-energy ion scattering (HEIS) spectrometry and is used to probe the structure and composition of materials by evaluating the backscattering of a beam of high energy ions that hit on a sample.

3.5.2.1 THEORY OF RBS

During RBS mono-energetic ions of high kinetic energy (0.5-4MeV) collide with the sample, after hitting it the incident ions are elastically scattered in the sample. Both scattered ions and their energy are collected. The information about the composition, the distribution of the components, and the thickness of the sample are all given by the data retrieved from the spectrum. The incident ions from a tandetron accelerator are positively charged He+ atoms or protons. The signal of the detector is processed by nuclear electronics and a computer-based multichannel analyser stores all energy spectra. The data evaluation is accomplished using standard procedures and computer codes. The advantage of the RBS analysis depends on the

quantitative analysis of major and minor constituents lying in the first 0.5 to 2.0 micrometres of a material. The detection limits vary from 10^{11} to 10^{15} at.cm^{-2} for heavy and light elements depending on the sample structure and composition. The solution to the detection limits of certain light elements may be improved using resonant scattering. The same as the depth distribution of constituents can be reconstructed with a good depth resolution. Moreover, RBS is dependent on the following factors: the kinematic factor, the differential scattering cross-section, and the energy loss of the particle.

3.5.2.2 KINEMATIC FACTOR

The interaction between the projectile ion of mass M_1 and energy E_O and the target atom of mass M_2 and energy E_1 can be properly described by an elastic collision of two isolated particles. After the elastic collision, a part of the projectile energy is transferred to the target. The kinematic factor is calculated by the principles of conservation of energy and momentum. The ratio K of the scattering energy to the incident energy can be defined as follows:

$$\boldsymbol{K = \frac{E_1}{E_0} = \left[\frac{\left(M_2^2 - M_1^2\ sin^2\theta\right)^{\frac{1}{2}} + M_1\ cos\theta}{M_1 + M_2}\right]^2} \qquad \boldsymbol{Eq.3.6}$$

Where K is the kinematic factor; θ the angle between the projectile incident direction and the scattered angle.

3.5.2.3 SCATTERING CROSS SECTION

The differential scattering cross-section dσ/dΩ is used to estimate the frequency of a collision and ultimately the scattering yield at a certain angle θ. This leads to the capability of quantitative analysis of atomic composition. Backscattering takes place with a known cross-section given by the following equation:

$$\boldsymbol{\frac{d\sigma}{d\Omega} = \left[\frac{z_1\ z_2\ \ e^2}{4E}\right]^2 \times \left(\frac{4}{sin^4\theta}\right) \times \frac{\left(\left[1 - \left(\frac{M_1}{M_2} \times sin\theta\right)^2\right]^{1/2} + cos\theta\right)^2}{\left[1 - \left(\frac{M_1}{M_2} \times sin\theta\right)^2\right]^{1/2}}} \qquad \boldsymbol{Eq.3.7}$$

With Z_1 and Z_2 the nuclear charge of the incident particle and target atom, respectively.

For a target of a thin film with thickness D, the scattering yield Y(θ), detected by a finite acceptance solid angle Ω at scattering angle θ, given by:

$$\boldsymbol{Y(\theta) = N \times D \frac{d\sigma}{d\Omega} \times \frac{\Delta\Omega \times Q}{cos\theta}} \qquad \boldsymbol{Eq.3.8}$$

Where Q represents the number of incident ions impinging into the target, N is the atomic density of the target, and θ is the incident angle.

3.5.2.4 ENERGY LOSS OR STOPPING POWER

Generally, an energetic particle that strikes a target, penetrates through. And in a case where the particle is pushed away from the target, its kinetic energy decreases as it loses the speed. Thus, two mechanisms are responsible for this loss of energy: Nuclear stopping, deriving from several collisions of the projectile with the atomic nuclei of the target and, the Electronic stopping, produced by the friction resistance of the projectile in coming across with the electron clouds of each target. Hence, the stopping power is nothing else but the energy loss per unit length dE/dx. The stopping section S [eV/ (atoms/cm2)] is related to stopping power and the atomic density N by the equation:

$$\boldsymbol{S = \frac{1}{N} \times \frac{dE}{dx}} \qquad \boldsymbol{Eq.3.9}$$

Where [S] is the energy loss factor for the determination of pf thickness. Signal heights are used to identify the phase in terms of atomic density and the number of counts at a specific energy.

3.5.3 MECHANICAL PROFILE-METRE

A simple way of measuring the thickness and the surface roughness of a thin film is by using a mechanical profile-meter, also called stylus profile-meter. The instrument uses a stylus that is swept across the surface while in contact. The changes in height caused by the surface morphology are recorded. The system was specifically designed for Si samples but, hard and soft materials can be profiled according to the stylus power selected. Moreover, the software offers useful processing of profiles, such as profile elevation, zero referencing, and magnification (Magubane, 2018).

3.5.3.1 PRINCIPLE OF OPERATION

A stylus profilometer's basic principle uses a small stylus diameter and moves along the surface. This stylus usually has a diamond tip. During a scan, the stylus is in direct contact with the surface. It records the data, meaning all the peaks and the valleys present on the surface, with high precision, but its precision is limited by the stylus tip diameter (Muhammad Amirzada, 2014). The basic principle of operation of the stylus profilometer is shown in Figure 3.7. While scanning, the stylus is translated in a vertical direction due to surface variation of the sample, as it is attached to a linear variable differential transformer. Consequently, the linear variable differential transformer senses and generates electrical signals by comparing the alternating current (AC) with the direction of the transition relative to the stylus movement (Magubane, 2018). The analogue signal is then transformed and processed to a digital format and stored in the computer memory. Furthermore, the Dektak 6 M profilometer can reach a maximum of 30 000 points per scan and each second can record a fixed number of 300 data points. This implies that the horizontal resolution of the profilometer depends on its scanning range of approximately 5μm to 30 mm and its period of 3 to 100 seconds (Magubane, 2018). Hence, the length of the scan increases the number of processed data points which guarantees improved resolution.

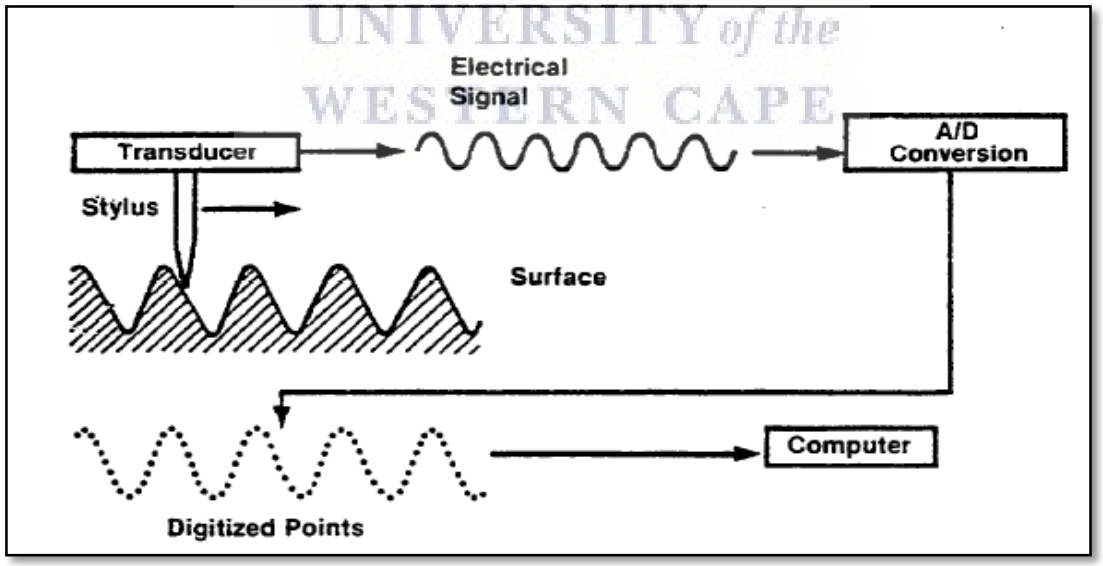

Figure 3. 7: Schematic representation of a working principle of a stylus profilometer (Muhammad Amirzada, 2014).

3.5.4 SCANNING ELECTRON MICROSCOPE

The scanning electron microscope (SEM) is an instrument used for the examination and analysis of microstructure morphology and chemical composition characterizations (Zhou and Wang, 2006). Inside the SEM, electrons are thermionically emitted from a cathode or a field emission gun (FEG), situated at the top of its electron-optical column. These emitted electrons form an electron cloud, and the beam of electrons is accelerated by high voltages towards a specimen containing anode. As the beam of electrons is accelerated down the SEM column, a series of electromagnetic lens coils and apertures are used to focus the electron beam (e-beam) into a fine probe that systematically scans over the specimen surface, to produce an image. This image formation in the SEM is dependent on the acquisition of signals produced from the beam and the specimen interactions. The interactions can be divided into two major categories: elastic interactions and inelastic interactions. Elastic scattering results from the deflection of the incident electron by the specimen atomic nucleus or by outer shell electrons of similar energy. This interaction is characterized by energy loss during the collision and by a wide-angle change of the scattered electrons. These scattered electrons are called back-scattered electrons (BSE) and yield a signal for imaging the sample (Zhou and Wang, 2006). The inelastic scattering then occurs through a variety of interactions between the incident electrons and the electrons/atoms of the sample and results in a primary beam electron transferring to that atoms. The amount of energy loss depends on whether the specimen electrons are excited and on the binding energy of the electron to the beam. As a result, the excitation of the specimen electrons leads to the generation of the secondary electron (SE), which is defined as possessing energy of less than 50eV and can be used to analyse the sample (Zhou and Wang, 2006). Furthermore, the SEM schematic in Figure 3.5, shows the two condenser lenses situated below the electron gun and are used to focus the emerging beam into a smaller diameter size, which is further aligned and focused by apertures and coils within the column until it reaches the objective lens near the specimen chamber. The objective lens then demagnifies the beam into a small spot of about 1μm in diameter and moves it in space until it reaches the specimen surface. Additionally, the objective lens also determines the intensity of the incident e-beam and controls the image brightness (Sfiso zwelisha khanyile, 2015).

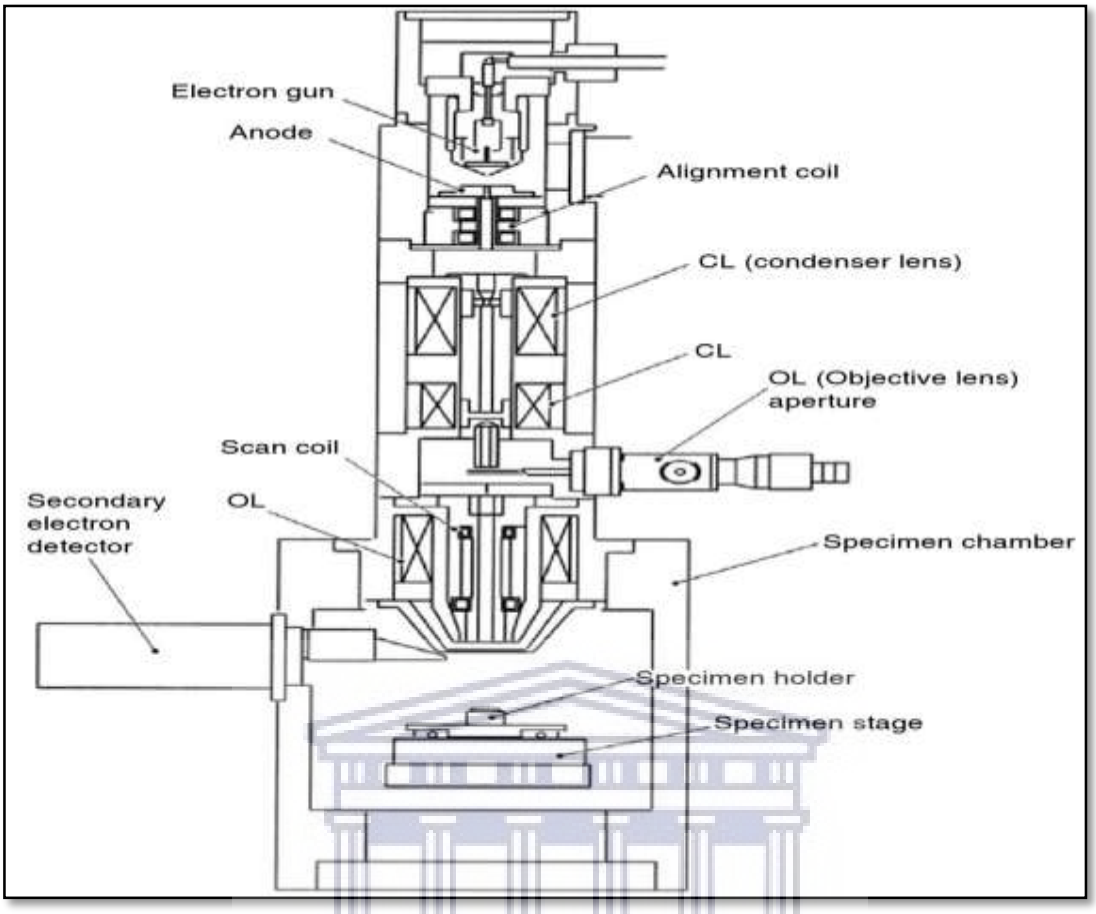

Figure 3. 8: Schematic illustration of scanning electron microscopy (Zhou and Wang, 2006).

3.5.4.1 RESOLUTION AND ABBE'S EQUATION

The limits of resolution are defined as the minimum distance by which two structures can be separated and still appeared as two distinct objects (Zhou and Wang, 2006). It was proven by Ernst Abbe that the limit of the resolution depends on the wavelength of the illumination source. At a certain wavelength, when resolution exceeds the limit, the magnified image blurs. Because of the diffraction and interference, a point of light cannot be focused as a perfect dot. Instead, the image will have the appearance of a larger diameter than the source, consisting of a disk composed of concentric circles with diminishing intensity. This is known as an airy disk. Generally, the airy disk is defined as the distance between the order peak and the first order trough. Hence, in a perfect optical system, the resolution can be described mathematically by Abbe's equation:

$$d = \frac{0.61\lambda}{\mu sin\alpha} \qquad Eq.3.10$$

Where **d** is the limit of resolution, **λ** is the illumination wavelength, **μ** is the refractive index, and **α** is the aperture angle.

3.5.4.2 DEPTH OF FIELD, APERTURE, WORKING DISTANCE

The portion of the image that appears acceptably in focus is called "depth of field". An electron beam with a smaller convergence angle alpha provides a larger depth of field see Fig3.9,

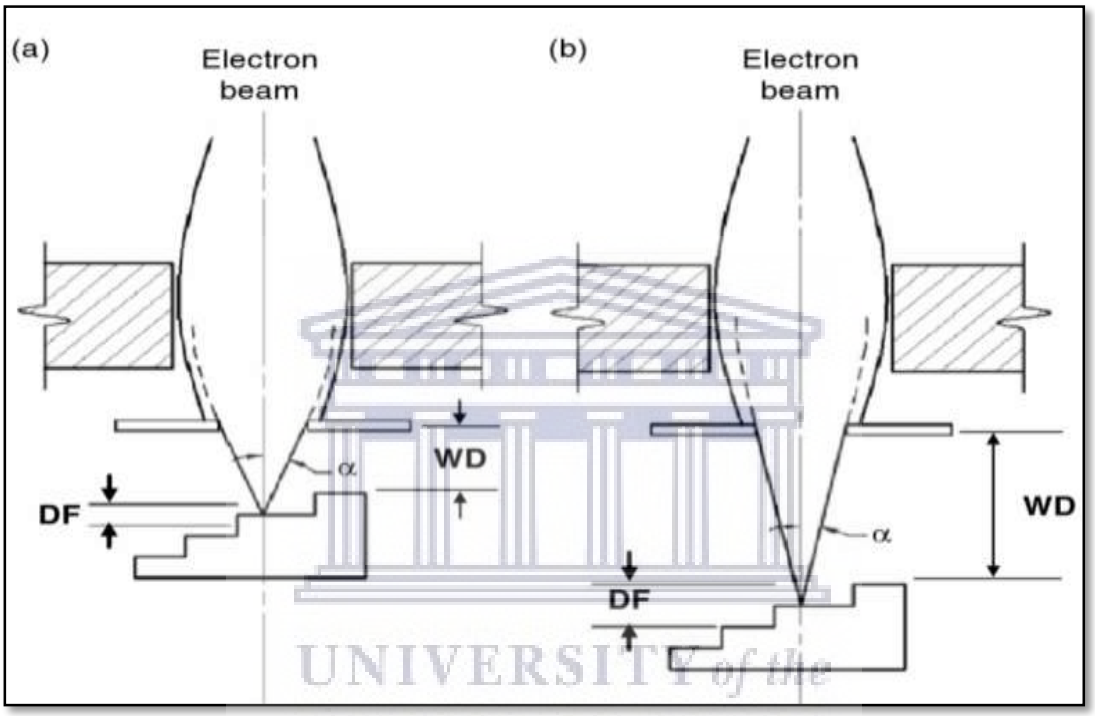

Figure 3. 9: Beam diagram showing the depth of field (DF) by increasing working distance (WD). a) Short working distance and b) long working distance (Zhou and Wang, 2006)

because the change of spot size is less significant along the beam direction for a sharper electron beam. Besides the aperture size, the working distance will also influence the depth of the field (Zhou and Wang, 2006). At a short working distance, the sample will be scanned with a cone of electrons resulting in an image with little depth of field. Conversely, at longer working distance, corresponding to a narrow cone of electron beam results in an enhanced depth of field. However, a long working distance does not mean a high resolution. The depth of field is important when it comes to observing the specimen with a large topographical variation. In this case, it is preferred to use a long working distance to bring as much of the image in focus as possible.

3.5.5 ENERGY DISPERSIVE SPECTROSCOPY

Energy-dispersive X-ray spectroscopy (EDS) is one of the most common spectroscopy techniques used by SEMs that have been commonly equipped with this chemical analytical device. It is used for completely qualitative analysis, that is, the identification of the elements presents at the point on the sample surface being struck by the electron beam (Russ, 2013). In this technique, electromagnetic radiation is bombarded into a material surface which in turn causes electrons from inner atomic shells to be ejected and subsequently filled with electrons from higher energy levels. Electromagnetic radiation used to excite the sample is usually a focused high energy stream of electrons, protons, or X-rays. In a typical SEM, a stream of electrons is used. Electron transition from the higher energy shells to lower energy shells causes X-rays to be emitted.

These X-rays can be generated from K, L, or M energy-level shells in a typical element, which corresponds to the principal quantum number, n = 1, 2, 3. Therefore overlapping of energy levels detected can occur (Russ, 2013). During electron beam – sample interaction, an inner electron from the K- shell may be dislodged leaving the atom in an excited state. The vacancy created in the K shell needs to be filled by an electron from the outer shells (L or M) for the atom to return to its normal ground state. When the recombination occurs, the outer electron undergoes a discrete energy transition and the energy difference between the two energy states is discrete and characteristic of that atom, which is then emitted as x-rays. After the vacancy is filled by an electron from the L shell, the emitted x-ray is referred to as the Kα x-ray. While if the vacancy is filled by M shell electron, Kβ x-rays are emitted, with α and β subscripts the first and second nearest neighbour shell, respectively. A similar nomenclature is adopted when an L shell electron is knocked off and the vacancy is filled by M shell electron. Figure 3.10 illustrates the schematic representation of the Bohr's atomic model and electronic transitions generating the x-ray radiation.

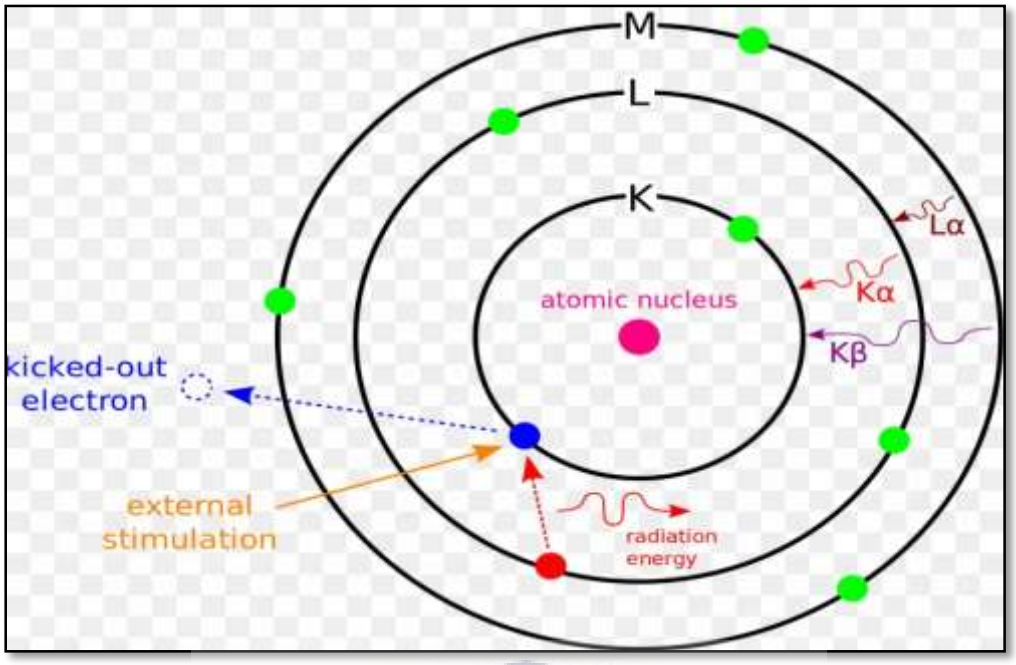

Figure 3. 10: Schematic representation of the generation of characteristic X-rays within an atom.

3.5.5.1 IMAGE DETECTION AND SAMPLE PREPARATION

The Signals produced in an EDS system are used in an image forming for morphological analysis as well as X-rays that are used for identification and quantification of chemicals present at detectable concentrations (Makhlouf and Aliofkhazraei, 2015). The EDS spectrometer contains the separation of the different characters according to their energies using a semiconductor detector. Inside the detector, the electrons of the semiconductor crystal are excited by absorbing energy from the coming x-ray. The number of electron-hole pairs generated determines the energy of the X-ray photon being detected which subsequently creates a charge pulse. This charge pulse is converted to a voltage pulse which remains proportional to X-ray energy by a charge sensitive preamplifier. This is then transmitted to a multichannel analyzer (MCA) which separates pulses according to their voltage**.** However, there is a detection limit in EDS depending on sample surface conditions, the smoother the surface the lower the detection limit. EDS can detect major and minor elements with concentrations higher than 10 wt% (major) and minor concentrations (concentrations between 1 and 10 wt %) (Makhlouf and Aliofkhazraei, 2015). The sample must, therefore, be clean, electrically conductive on the surface, and electrically grounded to get good images without degradation. Conversely, non-conductive samples present a problem of electrons building upon

the surface of the sample which is known as charging; therefore, it cannot be detected. Hence, samples are often coated with a thin layer of a conductive material such as Au or C (Magubane, 2018).

3.5.6 ULTRAVIOLET-VISIBLE (UV-vis) SPECTROSCOPY

UV-vis spectroscopy is the study of how a sample responds to light (Upstone Stephen, 2000). When a beam of light passes through a compound in solution or as a solid, some of the light may be absorbed and the remainder transmitted through the sample (Upstone Stephen, 2000). What is being observed spectroscopically is the absorbance of light energy or electromagnetic radiation, which excites electrons from the ground state to the first singlet excited state of the compound or material. The ratio of the intensity of the light entering the sample (I_0) to that exiting the sample (I) at a particular wavelength is defined as the transmittance (T) (Edinburgh Instruments, 2019). This is often expressed as the percentage transmittance (%T), which is the transmittance multiplied by 100 (Equation 1). Consider monochromatic light transmitted through the sample; with an incident intensity of I_0 and a transmitted intensity of I (Figure below).

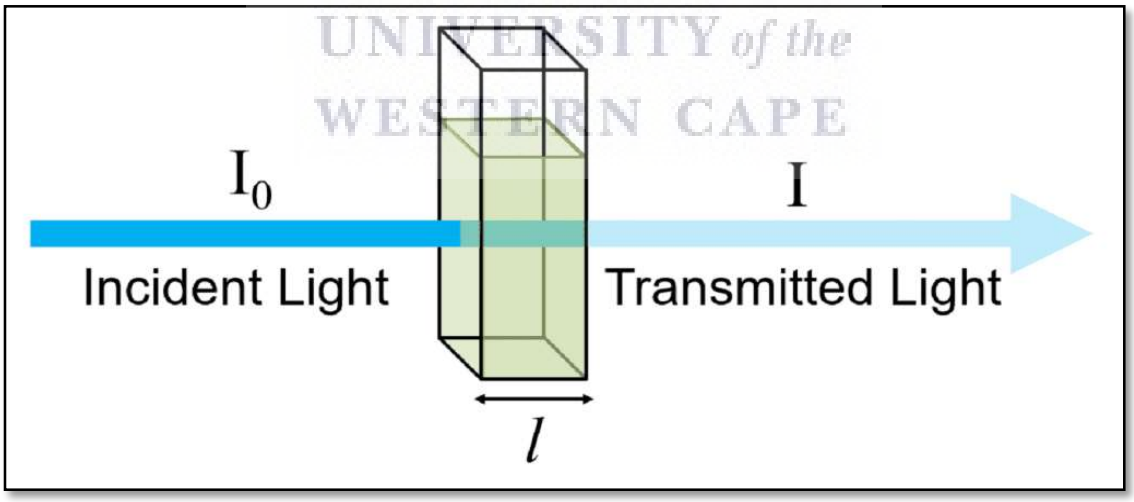

Figure 3. 11: A Beer-Lambert example (Edinburgh Instruments, 2019).

The percentage of transmittance (%T) is expressed as follows:

$$\%T = \frac{I}{I_0} \times 100 \qquad Eq.3.11$$

The absorbance (A) of a sample is the negative logarithm of the transmittance (Equation 9):

$$A = -logT \qquad Eq.3.12$$

The UV-Vis region of energy for the electromagnetic spectrum can cover a wavelength range of 800 nm-100 nm. The Beer-Lambert Law also known as Beer's Law Eq. 3.9, is the principle behind absorbance spectroscopy. This law states that, for a given substance, there is a linear relationship between concentration and absorbance provided that the path length is kept constant; the absorptivity (ε) is a constant for each molecule for each wavelength (Edinburgh Instruments, 2019; Upstone Stephen, 2000).

$$A = \varepsilon cl \qquad Eq.3.13$$

Where $\varepsilon =$ the absorptivity of the substance, $c =$ concentration, and $l =$ path length. Provided that the absorptivity and the path length are kept constant for a given set of experiments, a plot of the sample absorbance against the concentration of the absorbing substance should give a straight line.

3.5.6.1 RESOLUTION (BAND-PASS) AND SLIT WIDTH

UV-vis instruments have a specified band-pass. This term relates to the instrument's ability to resolve peaks that are very close together (small features on the side of a larger peak). The band-pass will either be fixed, usually between 1 and 2 nm, or, in the case of more sophisticated instruments, variable (either continuously or infinite steps). Photodiode-array instruments have a fixed optical band-pass as there is no physical slit aperture on these instruments, although the software may be able to simulate other slit conditions. The resolution is defined by the light dispersion, the polychromator, and the number of elements in the array. The band-pass will affect the instrument's ability to discriminate between sharp features. Most molecules possess a broad spectrum, so a small band-pass will not change the appearance of the spectrum apart from increased noise (Upstone Stephen, 2000).

3.5.6.2 EXPERIMENTAL SET- UP

A conventional spectrophotometer consists of a light source, a sample holder, a diffraction grating, or a monochromator for the separation of light wavelengths and a sensor. The radiation source used is often a Tungsten filament (300-2500 nm), a deuterium arc lamp that is continuous over the ultraviolet region (190-400 nm), or light-emitting diodes (LED) as well as Xenon arc lamps for the visible wavelengths (D. A. Skoog, F. J. Holler, and S. R. Crouch, 2006; Thinavhuyo Albert Ramashia, 2015).

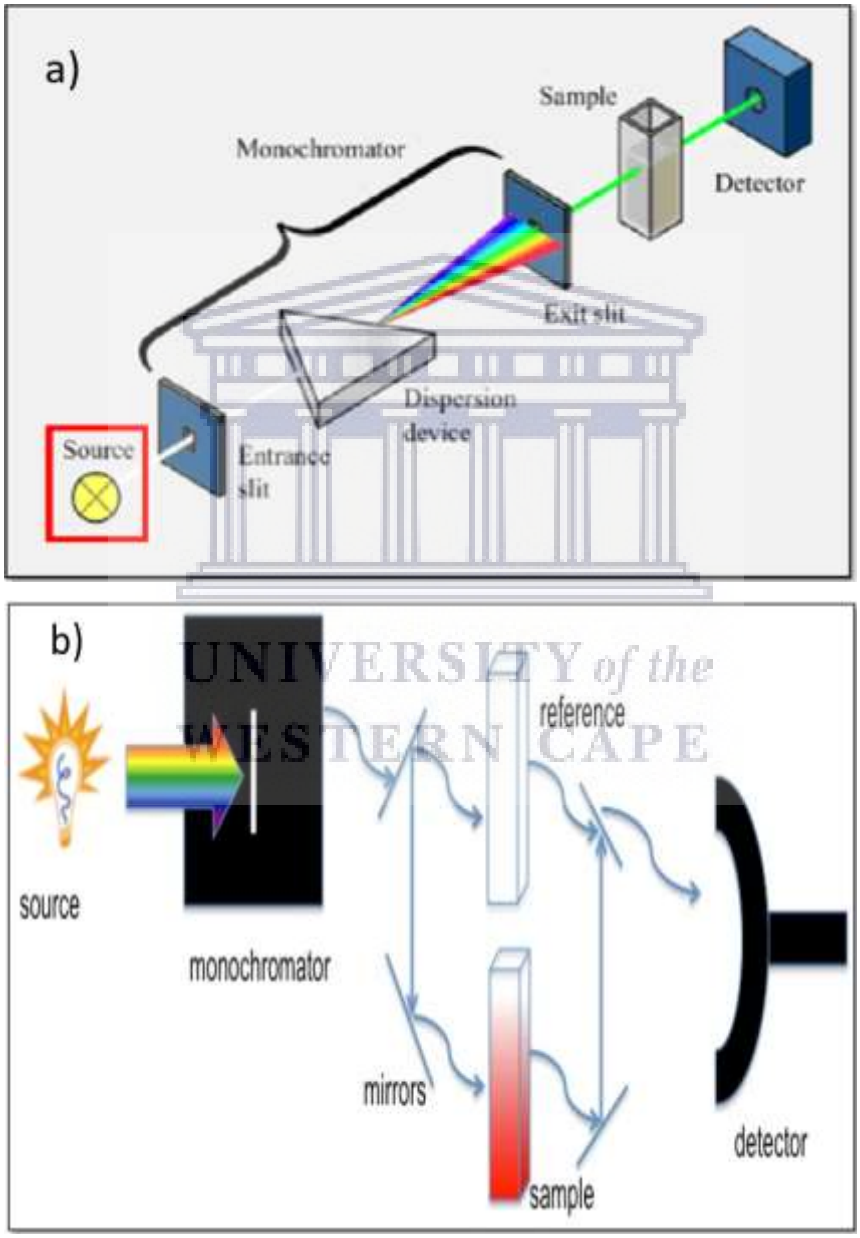

Figure 3. 12: A schematic diagram of a single beam (a) and a double beam (b) UV-Visible Spectrometer UV-Visible Spectrometer (Thinavhuyo Albert Ramashia. 2015)

Usually, the detector is a photodiode or a charged coupled device (CCD). Photodiodes are used with single-wavelength monochromators which filters the light to the detector. Diffraction gratings and the CCD are used to capture light from different wavelengths on different pixels. Generally, there are two types of UV-VIS instruments, namely the single and double beam spectrophotometer. On one hand, in a single beam, the light passes through the sample and the intensity of the incident light I_0 is measured by removing the sample. On the other hand, in the double beam, the light splits into two beams before reaching the sample. One beam is therefore used as a reference while the other beam goes through the sample. Both beams pass through both detectors simultaneously to be measured (D. A. Skoog, F. J. Holler, and S. R. Crouch, 2006; Thinavhuyo Albert Ramashia, 2015).

3.6 REFERENCES

B. D. Cullity, 1978 Book, “Elements of X-ray diffraction”, Addison-Wesley Publishing Company, Reading, Massachusetts.

Beer Lambert Law | Transmittance & Absorbance | Edinburgh Instruments <https://www.edinst.com/blog/the-beer-lambert-law/> (accessed 3.9.20).

Bunshah, R., 1994. Handbook of deposition technologies for films and coatings: science, technology, and applications.

D. A. Skoog, F. J. Holler, and S. R. Crouch, 2006, Book. Principles of Instrumental Analysis, 6th edition.

Hugh O. Pierson, 1999. Handbook of chemical vapor deposition (CVD) principles, Technology, and Applications William Andrew Publ. llc

I. G. Madiba, August 2012, Master Thesis, Thermochromic properties of VO2 nanocoatings by inverted cylindrical magnetron sputtering, University of Western Cape, South Africa.

Leijtens, T., Prasanna, R., Gold-Parker, A., Toney, M.F., McGehee, M.D., 2017. ACS Energy Lett. 2, 2159–2165.

Makhlouf, A., Aliofkhazraei, M., 2015. Handbook of Materials Failure Analysis with Case Studies from the Oil and Gas Industry.

Mattox, D., 2010. Handbook of physical vapor deposition (PVD) processing.

Muhammad Rizwan Amirzada, 2014. Dissertation for the acquisition of the academic degree Doktor der Ingenieurwissenschaften (Dr.-Ing.), University of Kassel.

Ron Jenkins, 2012. X-ray Techniques: Overview. Encyclopedia of Analytical Chemistry

R.A. Meyers (Ed.) pp. 13269–13288. John Wiley & Sons Ltd, Chichester, 2000.

Russ, J., 2013. Fundamentals of Energy Dispersive X-Ray Analysis: Butterworths Monographs in Materials.

Sfiso zwelisha khanyile, 2015, Master Thesis in deposition of silicon nanostructures by thermal chemical vapour deposition, University of the Western Cape.

Magubane S. S., November 2018, Master Thesis, Metal Assisted Chemically Etched

Silicon Nanowires For Application In A Hybrid Solar cell, University of Western

Cape, South Africa

Soussi, L., Garmim, T., Karzazi O, 2020 Effect of (Co, Fe, Ni) doping on structural,

optical and electrical properties of sprayed SnO2 thin film Elsevier

Tavakoli, M.M., Zakeeruddin, S.M., Grätzel, M., Fan, Z., 2018. 1705998, 1–9.

Thinavhuyo Albert Ramashia, 2015, Masters thesis, effect of the additional electron acceptor in hybrid zno:p3ht:pcbm spincoated films for photovoltaic application, university of western cape.

Upstone, S.L., 2012. Ultraviolet/Visible Light Absorption Spectrophotometry in Clinical Chemistry, Wiley Online Library.

Vinila, V.S., Jacob, R., Mony, A., Nair, H.G., Issac, S., Rajan, S., Nair, A.S., Satheesh, D.J., Isac, J., 2014. Cryst. Struct. Theory Appl. 03, 57–65.

Wagner, C.N.J., 1978. J. Non. Cryst. Solids 31, 1–40.

Zhou, W., Wang, Z.L., 2006. Scanning Microscopy for Nanotechnology.

<www.unf.edu/~michael.lufaso/chem4627/ch2_solid_state.pdf> (accessed 27.02.19)

CHAPTER 4

RESULTS AND DISCUSSION

4.1 INTRODUCTION

Halide perovskites have sparked huge interests in the fourth-generation photovoltaic field. They have also demonstrated a great potential for application in optoelectronic devices such as single-photon emitters and LEDs. A fundamental understanding of the halide perovskites property is essential for fabricating novel devices with better performances (Chen and Schu, 2018). Despite the power conversion efficiency (PCE) of organic-inorganic halide perovskite solar cells (PSCs) exceeding 22% (Saliba et al., 2016; Yang et al., 2015), toxicity related to lead content remains a major health concern, and one of a major drawback for large scale production of perovskite solar cells. Since 2014, several groups have reported on tin-based PSCs (Shao et al., 2018; Tavakoli et al., 2018a). However, the performance of tin-based PSCs is far below the lead counterpart because of two reasons: first, it is challenging for tin-based perovskite to form a homogeneous and continuous film due to the difficulty to control crystallization during processing (Ogomi et al., 2014; Xiao et al., 2018). Second, tin-based perovskite film shows significant instability due to Sn^{2+} oxidation states when exposed to air. This inevitability in tin-based PSCs instability will lead to p-type carrier doping, which will limit the carrier diffusion length (Xiao et al., 2018). Hence, a more viable solution may be in a Pb-Sn binary metal perovskite, which is less toxic but stable and efficient. In order to improve perovskite performance, microstructural factors should also be carefully controlled the during material preparation (Chen and Schu, 2018). The fabrication of perovskite with stable crystallographic structures can be achieved using synthesis techniques like Chemical Vapour Deposition (CVD), which enables the control of deposition parameters that can lead to the production of high-quality crystalline perovskite film, with fewer structural defects (Tavakoli et al., 2018b). Though there is a variety of CVD techniques that can be used for perovskite film synthesis depending on deposition parameters (operating pressure, precursor treatment), thermal CVD (TCVD) is a deposition method of choice. In this method, a powder source heated at high temperatures to produce a vapour was used for the growth of the film.

In this chapter, we report on the composition, the structure, and the optical properties of Pb-Sn perovskite film grown by thermal CVD. The alloying of the metal Pb by Sn grown by thermal evaporation facilitate the reduction of the lead content quantity in the perovskite film (Tavakoli et al., 2018b; Zuo et al., 2014). In a TCVD process, the reaction zone in the hot furnace is a crucial parameter, therefore the need to understand the influence of the substrate temperature and sample positioning in the chamber is vital. The relationship between the microstructural and optical properties was studied, this was followed by the investigation of the photons' response of the perovskite absorbing layer.

4.2 THIN FILMS ANALYSIS PROCEDURE

The discussion of the results is divided in two sections since the thin film of methyl-ammonium metal iodide $CH_3NH_3Pb_{1-x}Sn_xI_3$ perovskite was made in two sequential depositions.

- **Section one** deals with the results and discussion of Lead-tin iodide $(Pb\text{-}Sn)I_2$ and
- **Section two** deals with the results and discussion of the converted perovskite after the evaporation of methyl-ammonium iodide (CH_3NH_3I) on the metal iodide $(Pb\text{-}Sn)I_2$.

The conditions of thickness variation studied in this chapter of the grown metal iodide $(Pb\text{-}Sn)I_2$ and the converted perovskites thin films are summarized in Table 4.1.

The A1, A2 and A3 are $Pb_{1-x}Sn_xI_2$ samples representing 100 nm thickness of pure PbI_2 and different thickness of pure Sn thin film 20 nm, 35 nm, 85 nm, respectively. The samples were made through TCVD for the deposition of PbI_2, and thermal evaporation for the deposition of Sn film. The S1, S2 and S3 are $CH_3NH_3Pb_{1-x}Sn_xI_3$ converted binary perovskite samples with different thicknesses 240 nm, 255 nm, and 360 nm, respectively. The $CH_3NH_3PbI_3$ and $CH_3NH_3SnI_3$ are pure Pb, and Sn based perovskite samples with 300 nm 250 nm thickness.

Table 4. 1: Summary of the conditions: thickness variation

Materials	PbI_2	Sn	$CH_3NH_3Pb_{1-x}Sn_xI_3$	$CH_3NH_3PbI_3$	$CH_3NH_3SnI_3$
Thickness (nm)	100 + 20 **(A1)**		240 **(S1)**	300	250
	100 + 35 **(A2)**		255 **(S2)**		
	100 + 85 **(A3)**		360 **(S3)**		

4.3 SECTION ONE: LEAD-TIN IODIDE (Pb-Sn)I_2

As mentioned in Chapter 3, (Pb-Sn)I_2 was analysed using Rutherford backscattering spectroscopy (RBS) to determine the eutectic temperature, the stoichiometry, the chemical composition of the films, and the atomic depth profile. The structure of the films was characterized and confirmed by the X-ray diffraction technique using the D8 advance Bruker diffractometer, with $CuK_{\alpha 1}$ radiation of wavelength 1.54 Å. Then the morphology of the film was explored using a high-resolution Auriga FESEM, and the electron dispersion spectroscopy (EDS), was used to conduct the elemental composition of the film. Finally, the change in the bandgap was investigated to study the effect of the incorporation of Sn, this was done using UV-Vis spectrophotometry measurement.

4.3.1 RBS ANALYSIS AND STRUCTURAL STUDY OF (Pb-Sn)I_2

The measurement of the eutectic temperature between PbI_2—Sn, was conducted by real-time RBS, and the raw data analysed to determine the stoichiometry of the product. Thin films of PbI_2 were prepared from PbI_2 powder using a TCVD under N_2 atmosphere, the film was deposited on a glass substrate. A thin layer of Sn was then deposited onto the PbI_2 layer using thermal evaporation in a high vacuum. In this section (4.3.1) only sample A3 was considered for RBS studies.

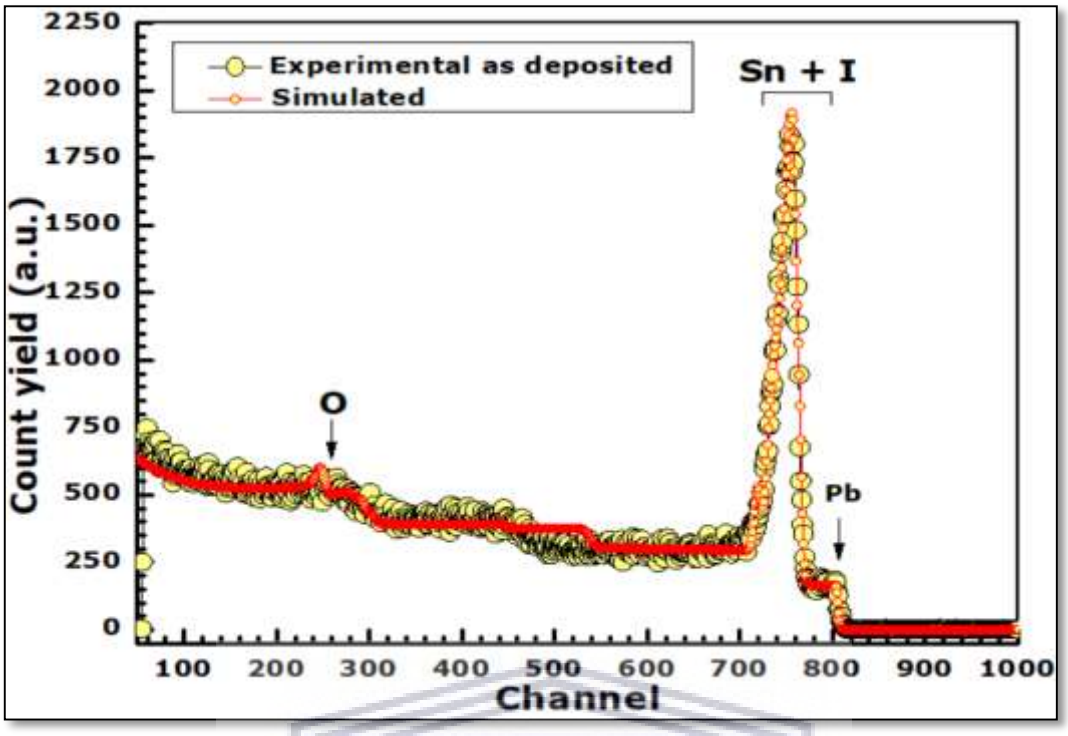

Figure 4. 1: SIMNRA software spectrum simulation of Sn/PbI_2 probed with 4 MeV alpha particles.

Moreover, to measure the eutectic temperature between PbI_2—Sn, real-time RBS was conducted, and the raw data was analysed to determine the stoichiometry of the product. Before, the quantitative RBS analysis was performed by simulating the RBS spectra of the as-deposited film (Fig4.1). The spectra above show RBS plot for **Sn**, **I,** and **Pb** elements. The peaks of Sn, and I, cannot be separated by RBS measurements since I and Sn, have close Z - values (Z=50 and Z=53 atomic number respectively). Therefore, the two peaks overlapped as shown in the Fig4.2. The overlapping peaks of I and Sn have high intensity, this might be the indication of a higher concentration of Sn. The small peak at channel approximately 800 belongs to Pb (Z=80). It has smaller counts, hence a smaller concentration compared to a higher peak which belongs to I and Sn. Furthermore, the stoichiometry of Pb-I-Sn was calculated from SIMNRA simulation software. The solid red line in the graph indicates the simulation fit to the raw data (Fig4.1). The results of the composition obtained from the complete simulation are illustrated in Table 4.2. The SIMNRA simulation indicates that Sn and I are dominant and composed of about 51% and 27% of atomic concentration per unit area, respectively. Moreover, the SIMNRA simulations indicate an atomic ratio of **Pb/Sn** close to **0.3:0.7** suggesting the formation of the $\mathbf{Pb_{0.3}Sn_{0.7}I_2}$ which confirmed that layers are Sn rich because

the sample was prepared with the excess of Sn. The depth profile illustrates, by comparison, a small amount of Pb in the composition, in which the thickness of PbI_2 needs to be preconsciously considered when compared to Sn which is 100 percent pure as opposed to PbI_2 (Pb and I). Therefore, the concentration of Sn needs to be balanced with Pb for equilibrium between the two elements. In addition to the three elements deposited Pb-I-Sn, there is a presence of elements such as calcium—Ca, potassium—K, silicon—Si, magnesium—Mg, and oxygen—O, in a small amount. It may be coming from the glass or it is due to the conditions of deposition and the environment, as Sn easily oxidizes and SnO/SnO_2 grows faster under humid conditions (Cho et al., 2005). Measurements for depth profile were performed and Table 4.2. illustrates the percentage of different elements present in the sample (IAEA, 2004).

Table 4.2: Components for $Pb_{(1-x)}Sn_xI_2$ films

Samples	**Layers**	**Thickness** x10^{15}**at./cm^2**	**Elements (at. %)**			**Substrate elements (at. %)**				
			Sn	I	Pb	O	Mg	Si	K	Ca
A	1	57.95	0.51	0.27	0.06	0.16				
	2	551.28	0.23	0.15	0.016	0.58				
	3	85.27	0.1			0.89				
	4	59102.47	0.04			0.84	0.03	0.033	0.038	0.036

Then, to ascertain the eutectic temperature of the reaction forming the metal iodide $Pb_{1-x}Sn_xI_2$ alloy and monitor the interdiffusion across the interface as well as the chemical reactions between PbI_2 and Sn on a glass substrate, the real-time RBS was performed.

Preliminary, the real-time annealing was conducted by a fast ramping of 20°C/min, up to 150°C and subsequently up to 300 ° C with a slower linear ramping rate of 2°C/min. This was performed to determine the temperature at which the reaction between PbI_2 and Sn occurred.

Upon annealing to 180 °C, no interdiffusion was observed. The RBS spectrum of the sample annealed up to 180 °C did not vary significantly from the as deposited one as observed in Figure 4.2 (a) and (b). The 3D RBS spectra and the contour 2D plot indicate that no intermixing at the

interface between PbI_2 and Sn until about 185 °C. In Figure 4.2 (a) and (b) two distinct growth regimes can be observed for the reaction between PbI_2 and Sn.

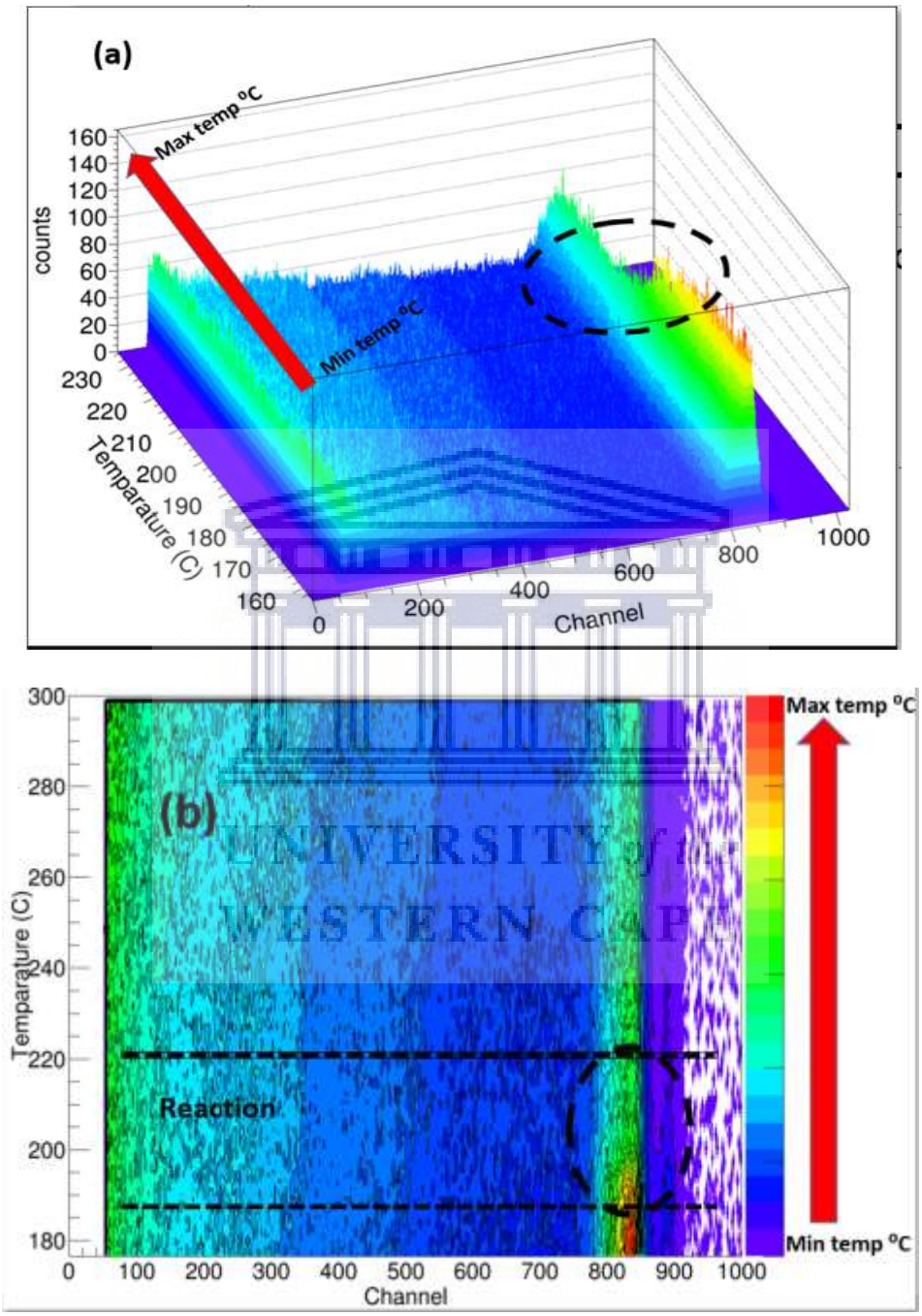

Figure 4. 2: Real-time RBS image showing the approximated mixing temperature of Pb-I-Sn elements on a glass. (a) is the 3D image, (b)- 2D is the image.

The area between the dashed circle in Fig 4.2 (a) and (b) in 3D and 2D respectively indicates the regions where the different stages of interface reactions occurred (Demeulemeester et al., 2010; Kun Chen, 2018). Two separate growth regimes for the reaction PbI_2-Sn could be observed in Fig 4.2 (a) and (b). From the temperature of 190°C interface diffusion began to take place with shifts in the spectrum peak of the Sn and I Fig4.2 (a). and the strong colour (red, yellow) between dashed lines suddenly disappeared in Fig4.2 (b) indicating the occurrence of the diffusion. The reaction rate for this region starts to decelerate after 220ºC, signifying that the reaction is complete, and the material has stopped diffusing. Similarly, in the 3D image from the top down between the dashed circle, it shows a slow drop of counts and the change in colour (red, yellow) indicating the diffusion of elements. Hence, it can be concluded that Pb, Sn and I elements that compose $Pb_{1-x}Sn_xI_2$ alloy started diffusing at 190ºC, and the diffusion caused the drop of count and the shift of the energy/channel. The end of the diffusion was observed at 220ºC (Fig4.2 b). In Fig4.3 we can see the clear difference between the as-deposited spectrum and after the reaction spectrum are compared.

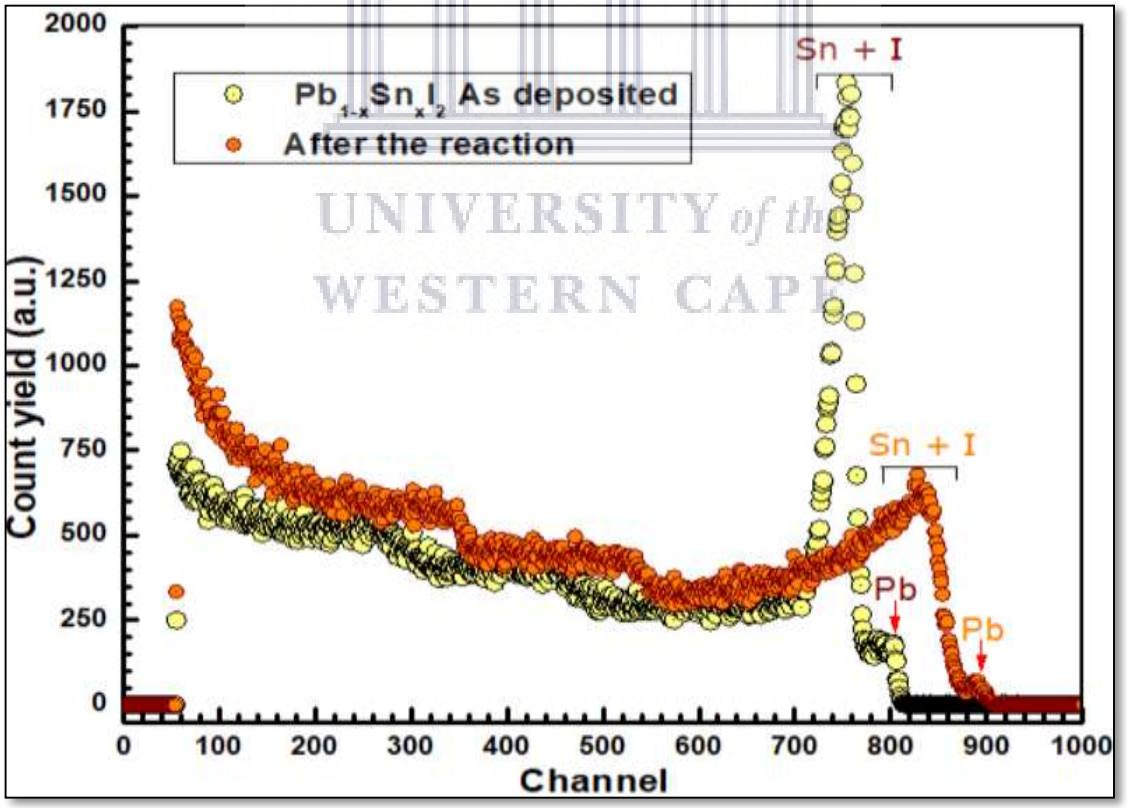

Figure 4. 3: Overlay of an as-deposited spectrum of Sn/PbI_2 sample and after the reaction.

4.3.2 XRD MICROSTRUCTURAL ANALYSIS

The samples on the glass substrate were annealed at 220 ºC for one hour in order to mix the two layers of PbI_2 and Sn to form a **$Pb_{1-x}Sn_xI_2$ alloy**, this temperature was chosen based on the results of the eutectic temperature as studied from real-time RBS analysis. The microstructure of the as-deposited and the annealed sample ($Pb_{1-x}Sn_xI_2$) were studied using an X-ray diffractometer. The study of the microstructural properties of pure PbI_2, pure Sn, and Sn alloyed PbI_2 thin films were measured over a 2θ range of 10º—65º as shown in Fig. 4.4. The X-ray patterns of the thin film of PbI_2, matched with the standard (JCPDS 00-007-0235) file indexed as phased PbI_2 with strong Bragg's peak observed at (001), (002), (003), and (004). The interplanar distance spacing **(d)** relative intensities are presented in Table 4.3. It can be deduced from the data that the strongest peak is observed at **d** = 6.875 Å and corresponds to the plane (001). An inspection of the data for the Sn-alloyed and unalloyed thin films of PbI_2 crystals indicates that the observed **d**-values and relative intensities closely match.

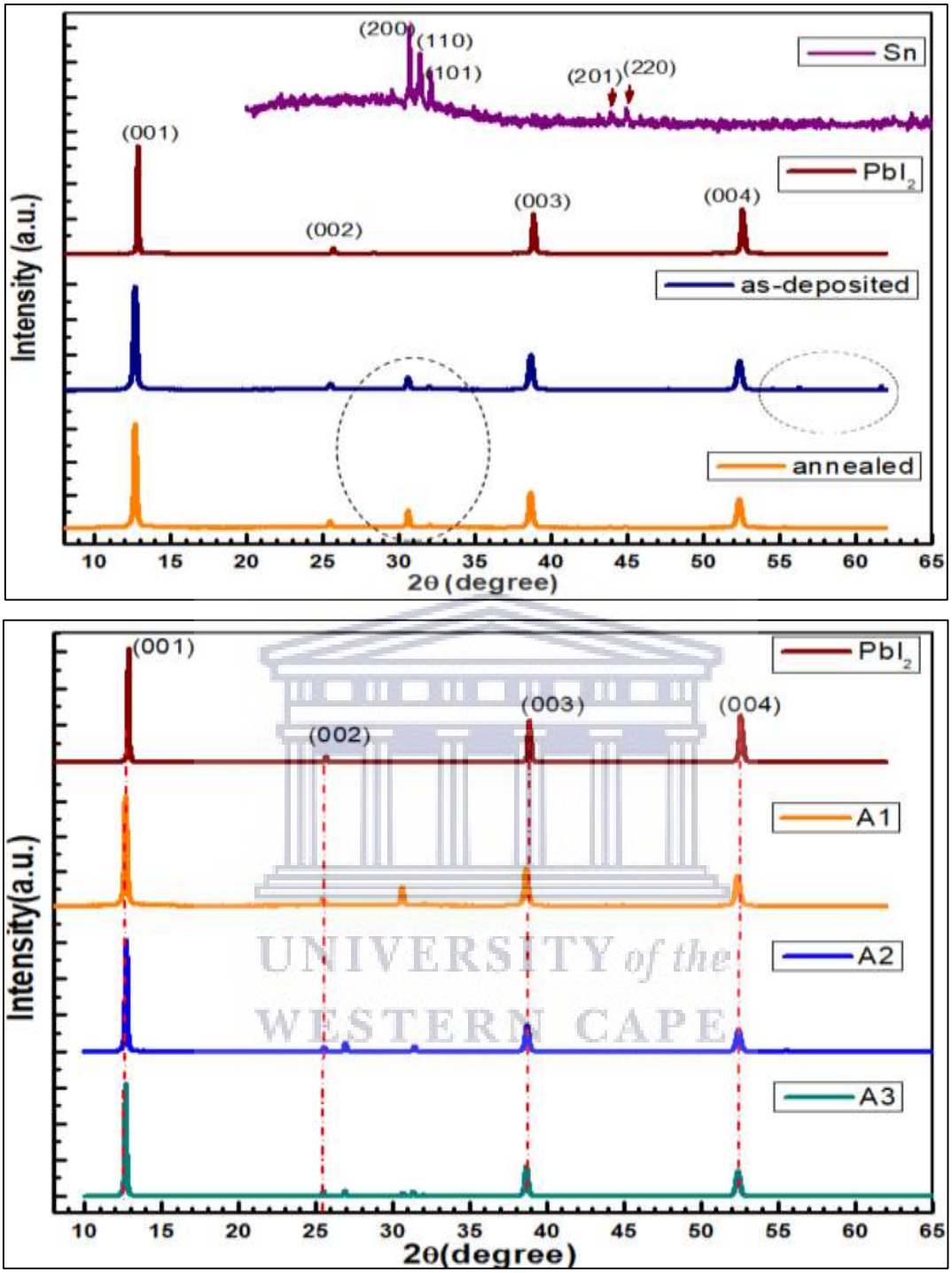

Figure 4. 4: X-ray diffraction pattern of pure Sn, pure PbI_2, and Sn-alloyed PbI_2 (A1, A2 & A3) synthesized nanocrystal with different thickness of Sn.

Table 4.3: Microstructural parameters of pure and Sn-alloyed PbI_2 thin films calculated from XRD patterns.

Samples	Thickness (nm)	Planes (hkl)	2θ	Calculated d-values (Å)	D_{hkl}	Relative intensities I/I_0 (%)
PbI_2	150	(001)	12.901	6.875	16.097	100
		(002)	25.754	3.460	11.464	5
		(003)	38.880	2.315	7.177	37
		(004)	52.6594	1.736	5.647	41
A1	120	(001)	12.697	6.968	10.673	100
		(002)	25.593	3.468	9.070	4
		-	27.02	3.296	-	8
		-	31.50	2.846	-	5
		(003)	38.734	2.322	5.504	24
		(004)	52.468	1.742	4.350	20
A2	135	(001)	12.740	6.371	11.637	100
		(002)	25.477	3.492	9.618	4
		-	27.02	3.296	-	5
		-	30.59	2.919	-	3
		-	31.39	2.846	-	4
		(003)	38.619	2.329	6.094	27
		(004)	52.428	1.743	4.849	23
A3	185	(001)	12.693	6.968	5.593	100
		(002)	25.591	3.484	5.953	7
		-	30.59	2.919	-	13
		-	32.09	2.789	-	5
		(003)	38.695	2.326	4.830	35
		(004)	52.448	1.742	4.475	29

However, it presents a difference with the JCPDS card whereby the highest peak is observed at **d**=3.460 Å corresponding to the plane (002) for hexagonal structures**.** This difference could be attributed to the method used to prepare our samples (Wang et al., 2017; Zhu et al., 2010). Nevertheless, the XRD pattern of pure PbI_2 shows no presence of other peaks, this

demonstrates that the sample is well crystallized. But, the incorporation of Sn impurity into PbI_2 leads to the evolution of new peaks shown in the dashed lines area of the as-deposited film, around 27.02°, 30.5°, 32.03° (Fig4.4) in the XRD pattern of **A1, A2,** and **A3** which may be ascribed to the reflection of SnI_4 (00-006-0232) and PbO phase (Nanorod and Menggunakan, 2015). These peaks grow in intensity with increasing Sn concentration and evolve as clear peaks in the XRD patterns of A1, A2, and A3.

Furthermore, in Fig.4.5, the XRD patterns of all samples were analysed in the range 10–15º, this was done to compare the XRD peaks of pristine PbI_2 and PbI_2: Sn.

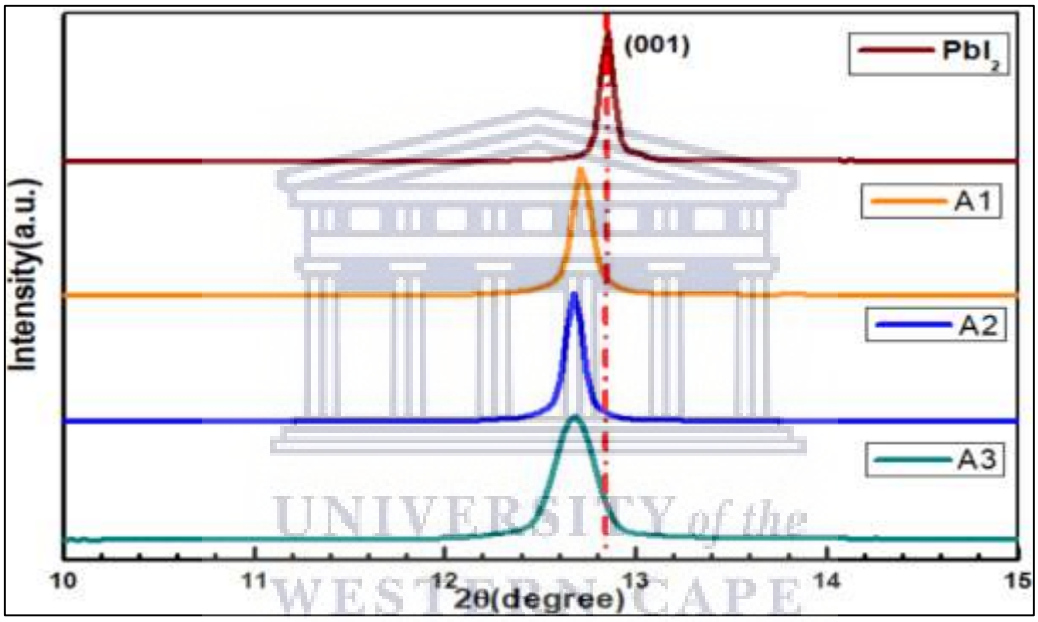

Figure 4. 5: X-ray diffraction patterns of PbI_2, A1, A2 and A3 in the range of 10–15º showing (001) plane.

The result shows a maximum shift of 0.18º in the Bragg angle of the (001) peak toward smaller values of 2 theta in the XRD patterns of the alloyed samples effect of dopant concentration on lattice parameters and the shift may be explained in the following way. (i) Sn-alloyed in the form of Sn-stannous ion presumably dissociates into Sn^{2+} to replace Pb^{2+}, where overall charge neutrality is obtained, thereby reducing the grain size. As the radii of the substituted and the replaced ions are comparable, the lattice parameters and the unit cell volume remain almost unaltered at lower concentrations of Sn-stannous in lead iodide. (ii) At higher Sn-stannous concentrations, the non-isoelectronic substitution may result in the creation of vacancies. The substitution of Sn^{2+} cation sites lead to the creation of cation vacancies. The vacancies created

in the lattice might be responsible for the increase in the lattice parameters as lead iodide being a layered compound, leading to an increase in the volume. Similar results were observed for Zn-doped PbI_2, Au-doped ZnO thick films (Bhavsar and Saraf, 2003; Sahu et al., 2014).

The average nanocrystalline size was calculated using Debye-Scherrer's (Mote et al., 2012; Zak et al., 2011) (Fig. 4.6) formula:

$$\boldsymbol{D = \frac{k\lambda}{\beta_{hkl}\, cos\theta}} \qquad \boldsymbol{Eq.4.1}$$

And it was plotted as:

$$\boldsymbol{\beta_{hkl} cos\theta = \frac{k\lambda}{D}} \qquad \boldsymbol{Eq.4.2}$$

Where β_{hkl}= FWHM**,** D = crystalline size, K = shape factor (0.9), and λ = wavelength of Cuk_{α} radiation. The size is also calculated to using the Williamson–Hall (W–H) plot (see Fig.4.6) for comparison:

$$\boldsymbol{\beta_{hkl} = \frac{k\lambda}{Dcos\theta} + 4\varepsilon tan\theta} \qquad \boldsymbol{Eq.4.3}$$

And to plot as:

$$\boldsymbol{\beta_{hkl} cos\theta = \frac{k\lambda}{D} + 4\varepsilon tan\theta} \qquad \boldsymbol{Eq.4.4}$$

With $\boldsymbol{\varepsilon}$ = the strain.

The XRD data is analysed further to calculate the lattice micro-strain ($\boldsymbol{\varepsilon}$) and other crystallographic parameters. These parameters are presented in Table 4.3. It may be seen from this table that the lattice parameters and hence the unit cell volume are sensitively affected by doping. The lattice parameter in Table 4.4 is almost constant for all the films, which indicates that there is no dilation of the unit cell along a or c direction. Moreover, as the doping concentration increases, the average crystallite size is found to decrease for PbI_2: Sn in both calculations (D-S and W-H).

Table 4.4: The calculated lattice parameters and unit cell volume for pure PbI_2 and Sn-doped PbI_2 films.

Samples (nm)	**a (Å)**	**c (Å)**	**Cell volume V(Å)^3**	**Scherrer method D(nm)**	**Williamson-Hall method (UDM)**	
					D (nm)	ε no unit x10^{-3}
PbI_2 (150)	4.216	6.914	122.893	853	231	1.55
A1 (120)	4.229	6.957	125.129	439	118	1.17
A2 (135)	4.255	6.980	126.373	660	216	1.95
A3 (185)	4.493	6.971	140.723	231	40	---

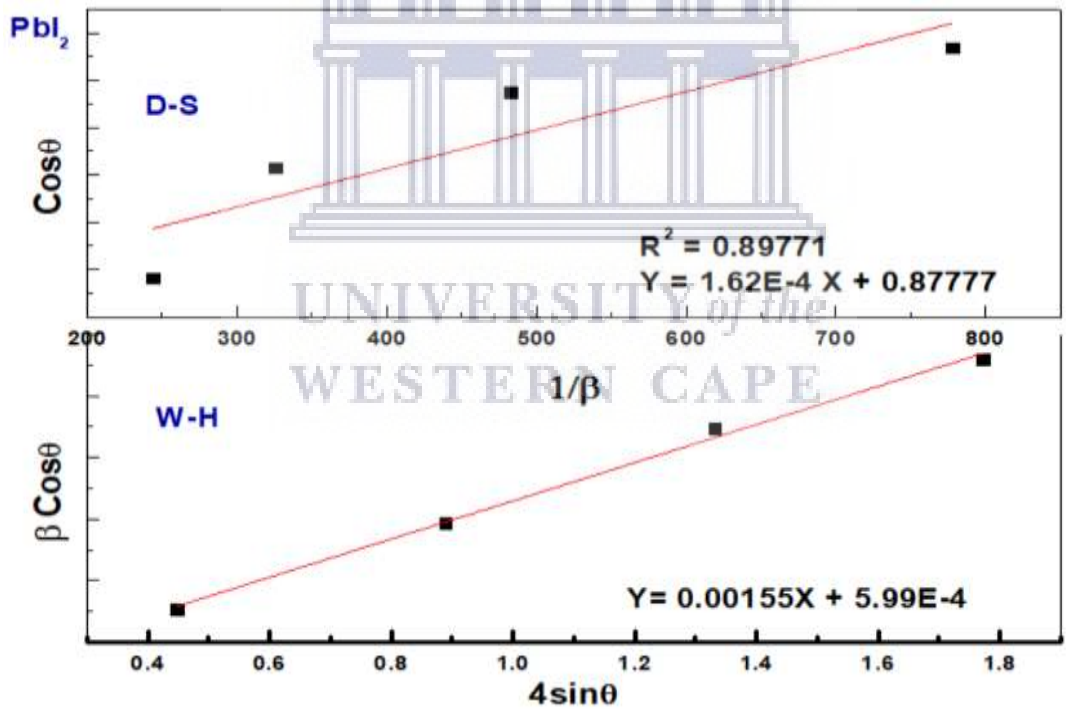

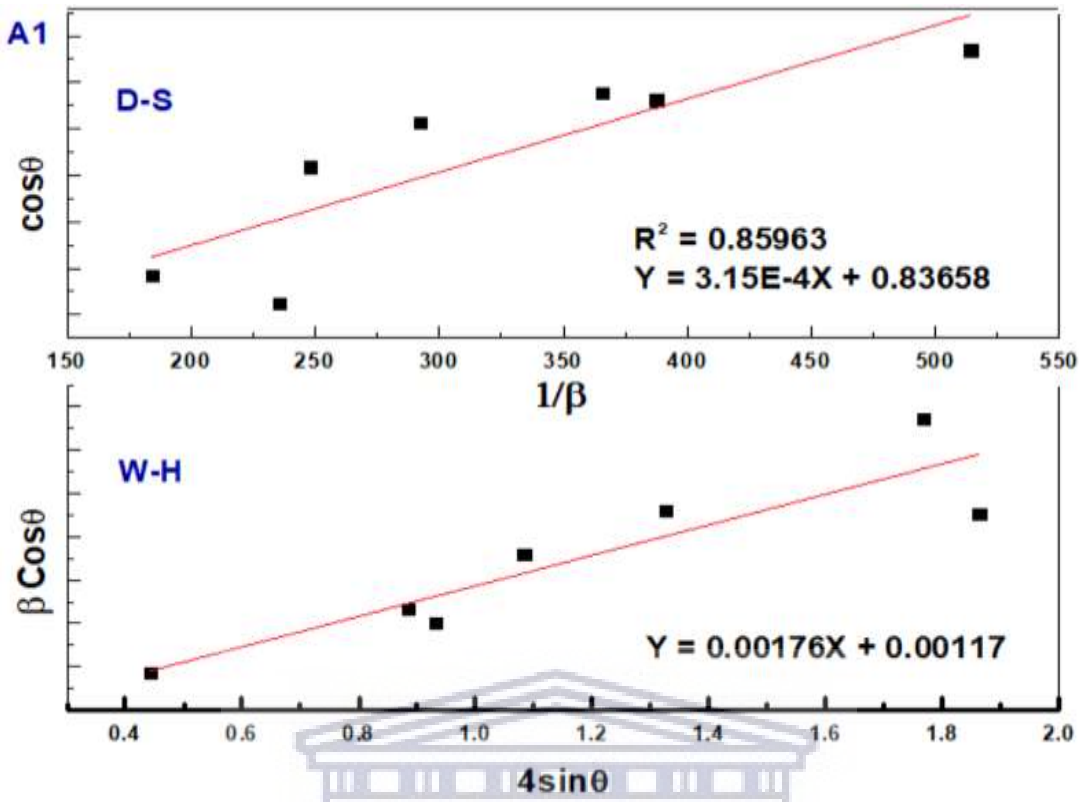

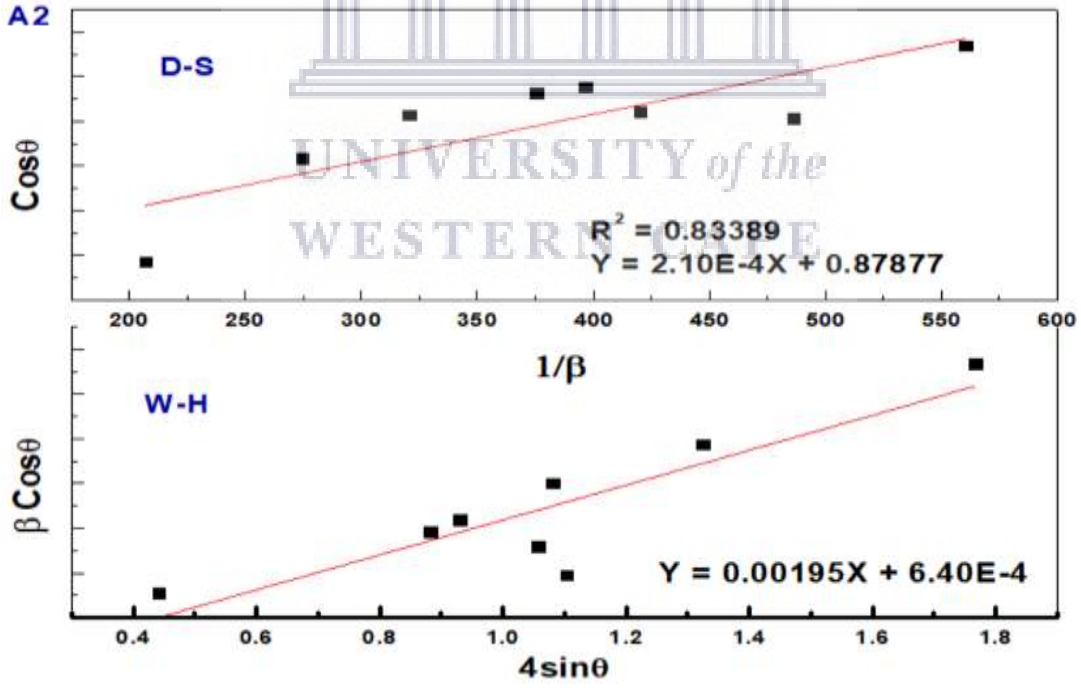

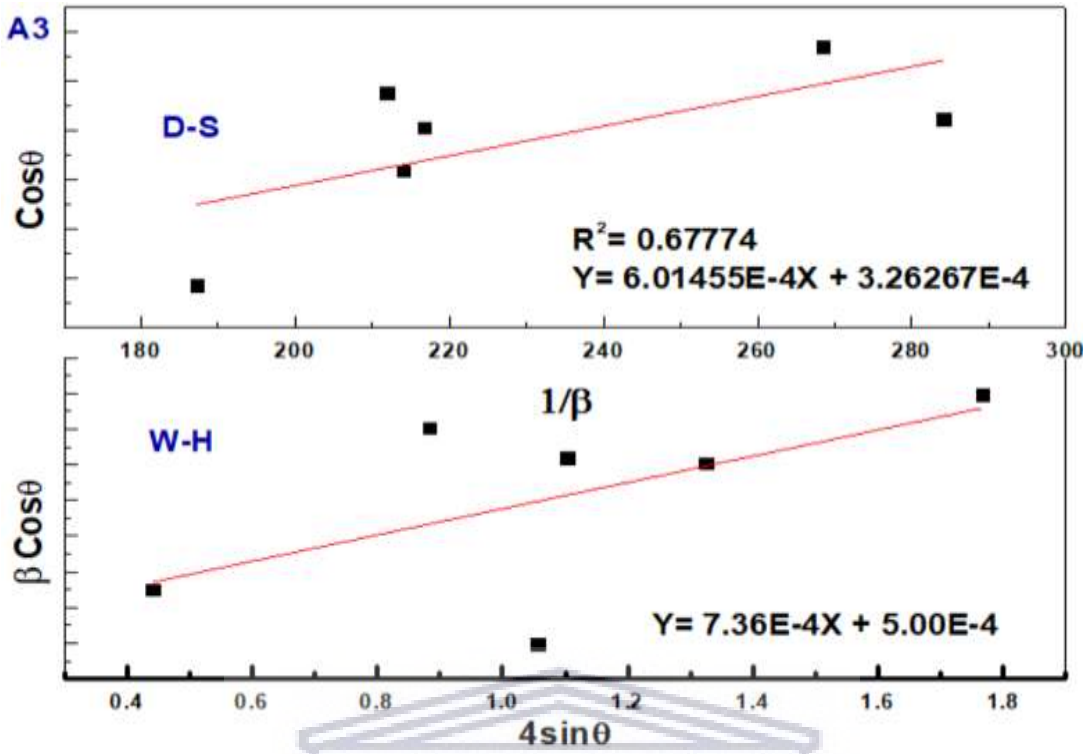

Figure 4. 6: The Debye-Sherrer (D-S) analysis and Williamson-Hall (W-H) UDM-method of PbI_2, A1, A2 and A3 nanoparticles. Fit to the data, the strain is extracted from the slope and the crystalline size is extracted from the y-intercept of the fit.

4.3.3 MORPHOLOGICAL AND ELEMENTAL STUDY

The high-resolution scanning electron microscope (SEM) images and energy dispersive spectrometry (EDS) plots are shown in Fig4.7 and Fig4.8, respectively. The information about the morphology, particle shape, and size of Sn-PbI_2 can be obtained from the plots. Figure 4.7. depicts top-view scanning SEM of PbI_2, Sn, and as-deposited as well as annealed Sn-PbI_2 films. The micrographs (d), (e), (f) represent different thicknesses of Sn to form $(PbSn)I_2$. PbI_2 was the first to be deposited at the bottom which layer acts as a scaffold—see Fig4.7**. a)**. This layer, therefore, needs to be controlled in terms of grain size and smoothness. After it was followed by the deposition of pure Sn on top of the PbI_2 film. We intentionally showed the micrograph of as grown pure Sn on glass in Fig4.7 b) to trace the difference that happened in the mixed film. The deposited film of pure Sn shows small grains on the surface with black gaps from each other.

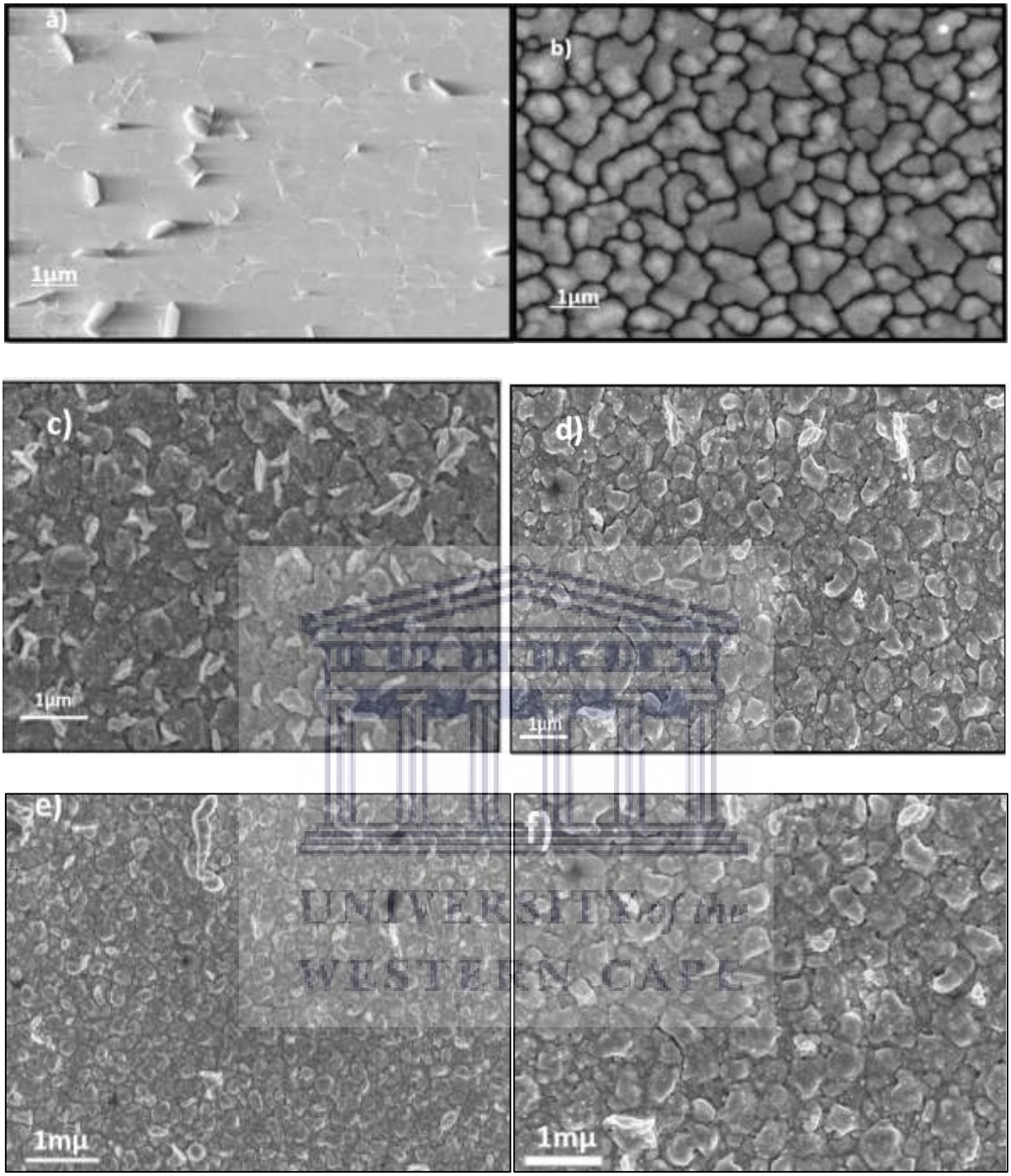

Figure 4. 7: a) Photographs of glass substrates after deposition of a) PbI_2, b) pure Sn, c) alloy (Pb/SnI_2) as deposited and d) alloy formed after 1h reaction time and d), e) and f) different concentration A1, A2, and A3, respectively.

By depositing pure Sn on PbI_2 layer, we noticed the change that occurred between them (PbI_2, Sn) see the as-deposited film Fig4.7 **c)**. This image shows an isolated and short crystal-like structure with a sharper tip surrounded by a very small cluster of fewer and shorter similar structures. In Figure 4.**7 d)**, the image shows morphological evolution due to annealing (Fig4.**7.**

d). After annealing, there is a clear difference between as grown Sn-PbI_2 and the alloy Pb-Sn-I mixture obtained. When the alloy is formed, we can see the spaces between the grains of Sn start filling up with lead iodide underneath. Consequently, the grains on top start changing structures and sizes. However, there is a little difference between the varied concentrations d), e) and f), the film gets much rougher with the excess of Sn.

The qualitative elemental composition of the material acquired from EDX analysis is shown in Fig 4.8, and the elemental composition is presented in table 4.4. The EDS analysis was done not only to ascertain the chemical composition of the surface morphology but also as a comparison to the RBS findings discussed above. The analysed film was about the same thickness as the RBS samples. The EDS results show the signals of Pb, Sn, and I, and the presence of C, O, Na, Si, Mg, and Al in various concentrations as shown in Table 4.5, which come from the glass substrate or may be due to the exposure of samples and it is consistent with the RBS results presented in the previous section. The sample is predominantly Sn (27.93, 26.38 wt. %) with the atomic percentage metal ratio of **Pb/Sn: 0.17:0.83** and **0.12:0.88** for two different spectra, suggesting the formation of the $\mathbf{Pb_{0.17}Sn_{0.83}I_2}$ and $\mathbf{Pb_{0.12}Sn_{0.88}I_2}$.

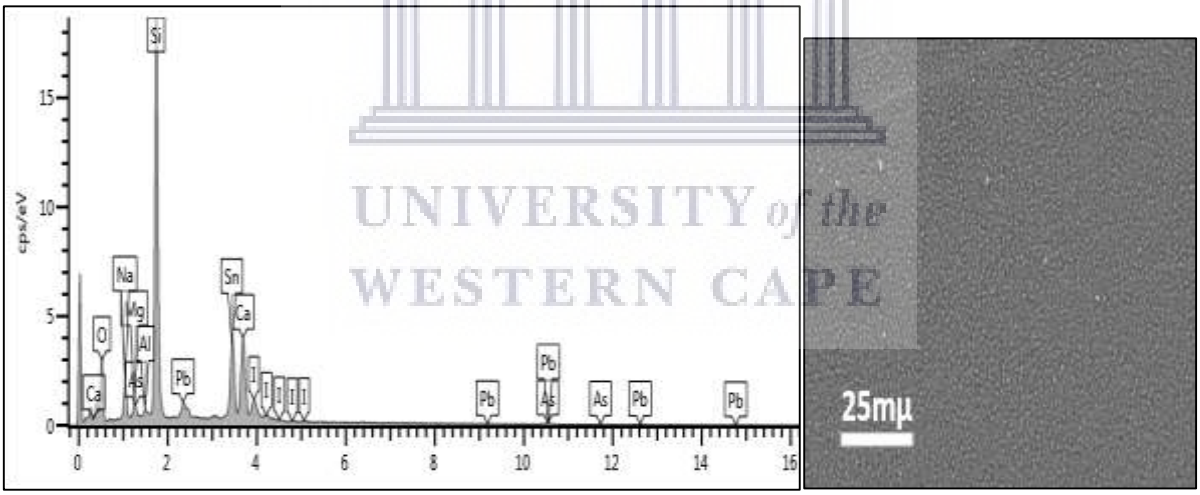

Figure 4. 8: Energy-dispersive X-ray spectroscopy (EDS) elemental analysis of (Sn-Pb)I_2

Table 4.5: Elemental composition **Sn-PbI_2 of A3** on a glass substrate

Elements	Atomic (. %)		Weight (. %)	
	Spectrum 1	Spectrum 2	Spectrum 1	Spectrum 2
Pb	1.89	0.77	10.2	4.92
Sn	9.04	7.18	27.93	26.38
I	3.18	1.17	10.51	4.61
Si	34.53	34.49	25.25	29.98
O	38.41	41.8	16	20.07
Ca	5.17	5.46	5.39	6.78
Al	--	0.55	--	0.46
Mg	1.91	1.96	1.21	1.48
Na	5.88	6.61	3.52	4.7
Total	100	100	100	100

4.3.4 UV-VIS SPECTROSCOPY ANALYSIS

The study of the optical properties of PbI_2 and the alloys was performed in the range of 350 nm–900 nm wavelengths see Fig4.9. The absorbance capacity of PbI_2 was investigated while incorporating various thicknesses of Sn nanoparticles such as 20 nm, 35 nm, and 85 nm, attributed to A1, A2, and A3 respectively. The absorption coefficient is high for all the samples, indicating the direct type of transition (Bhavsar and Saraf, 2003). The absorption edge for lead iodide is small and clear (Fig4.9). For higher-doping levels of Sn, the change is noticed. Therefore, the broadening of the absorption edge can be due to the grain boundary discontinuity effect and the lack of stoichiometry generally observed in crystalline materials (Bhavsar and Saraf, 2003).

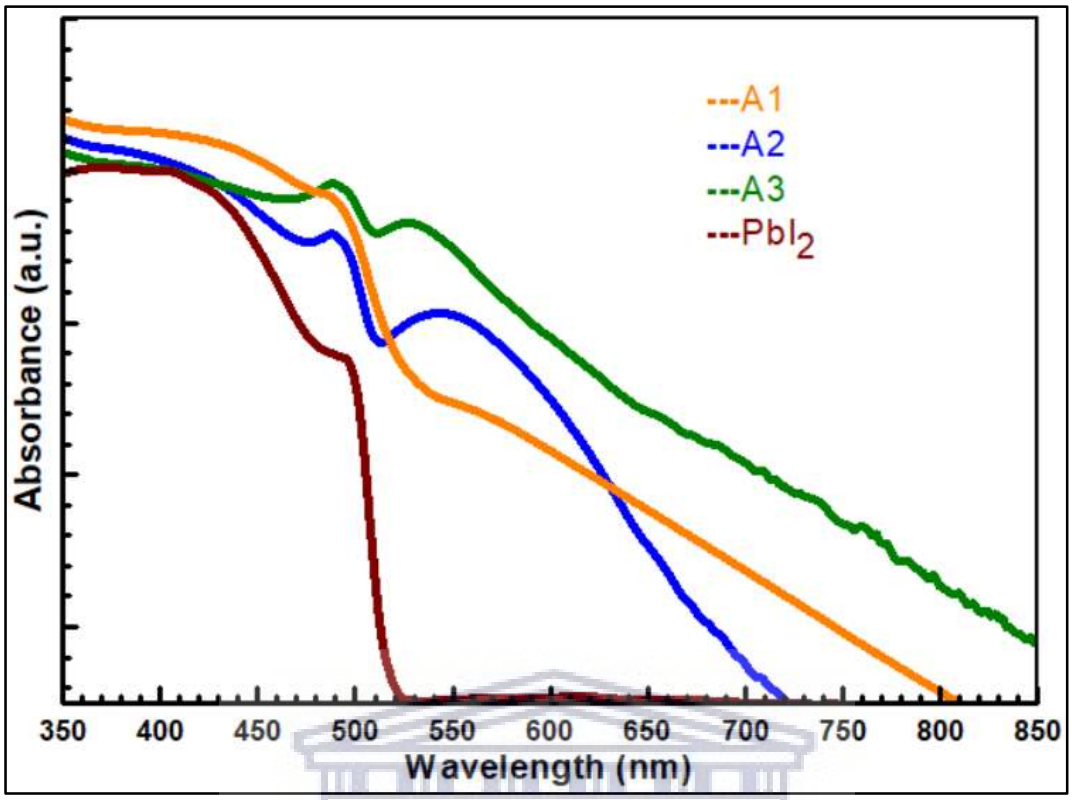

Figure 4. 9: Shows compared absorption spectra of PbI_2 and Sn-alloyed PbI_2 normalised. The spectrum of PbI_2 shows a slight shift from 500 to 550 nm in the excitonic absorption band when increasing the concentration of Sn, A1, A2, and A3.

Thus, one can distinguish the weak absorption region, extending over a considerable magnitude, and the high absorption region. Plots of absorbance versus wavelength (λ) for these thin films are shown in Fig. 4.10. A high absorption coefficient is achieved by the increasing Sn in lead iodide, which leads to a decrease in the bandgap. The variation of energies (Eg=2.39eV; Eg=2.0 eV; Eg=1.91 eV Eg=1.78 eV) given in Fig. 4.10 shows the bang gaps difference for lead iodide and Sn-alloyed thin film samples. The optical band gaps were determined from Tauc's model equation (Soussi et al., 2020) by the plots of $(\alpha h\nu)^2$ versus hν using the following formula:

$$\boldsymbol{\alpha h\nu = A(h\nu - Eg)^{1/2}} \qquad \boldsymbol{Eq.4.5}$$

Where **hν** is the photon energy, **A** is a constant, thus, a plot of $\boldsymbol{(\alpha h\nu)^2}$ against **hν** is a curve line whose intercept on the energy axis gives the bandgap energy.

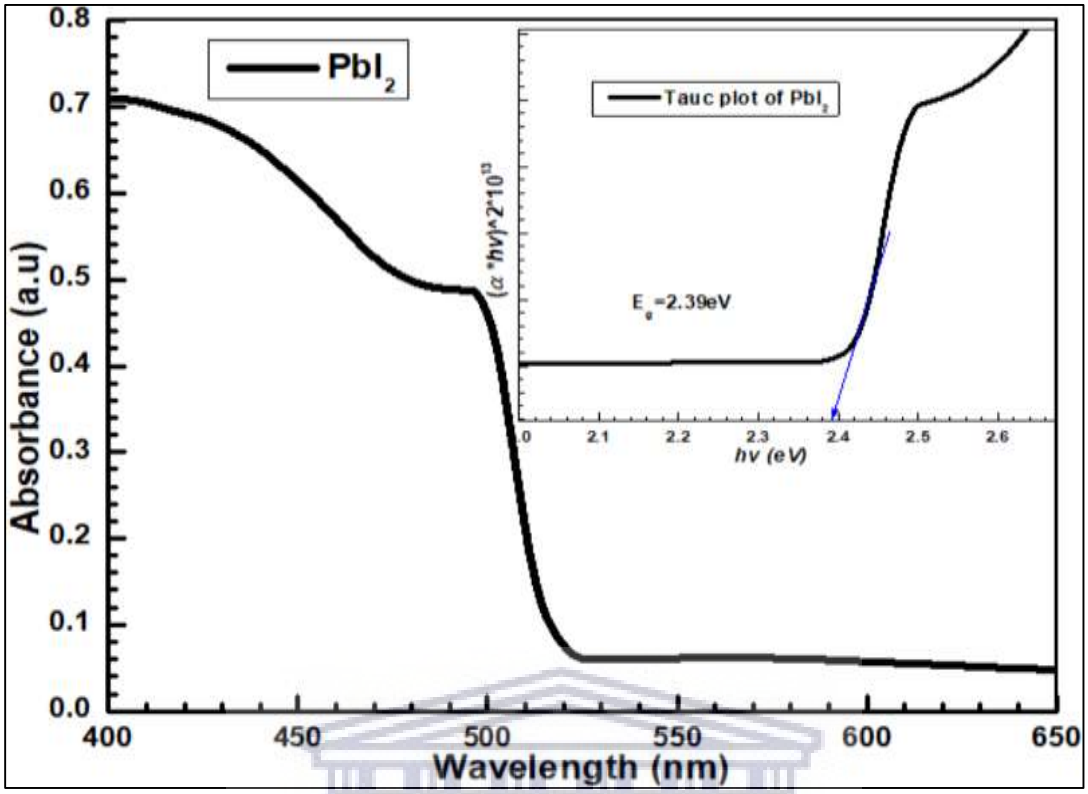

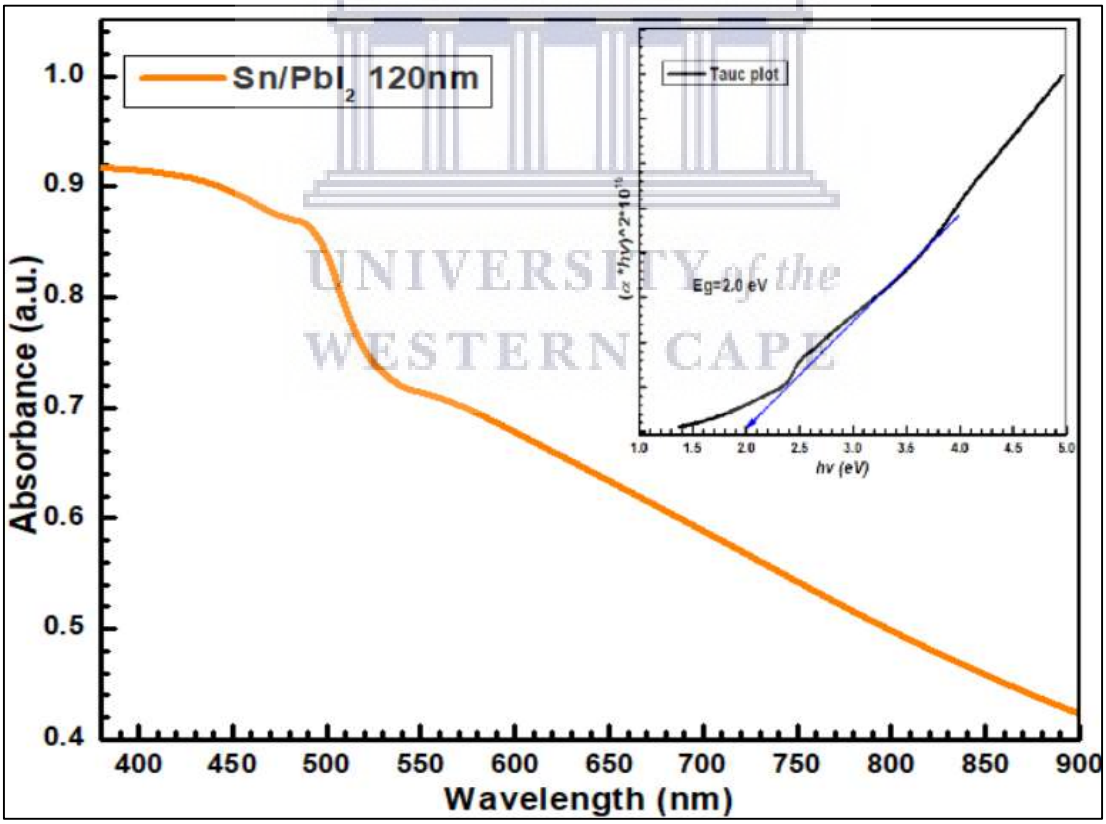

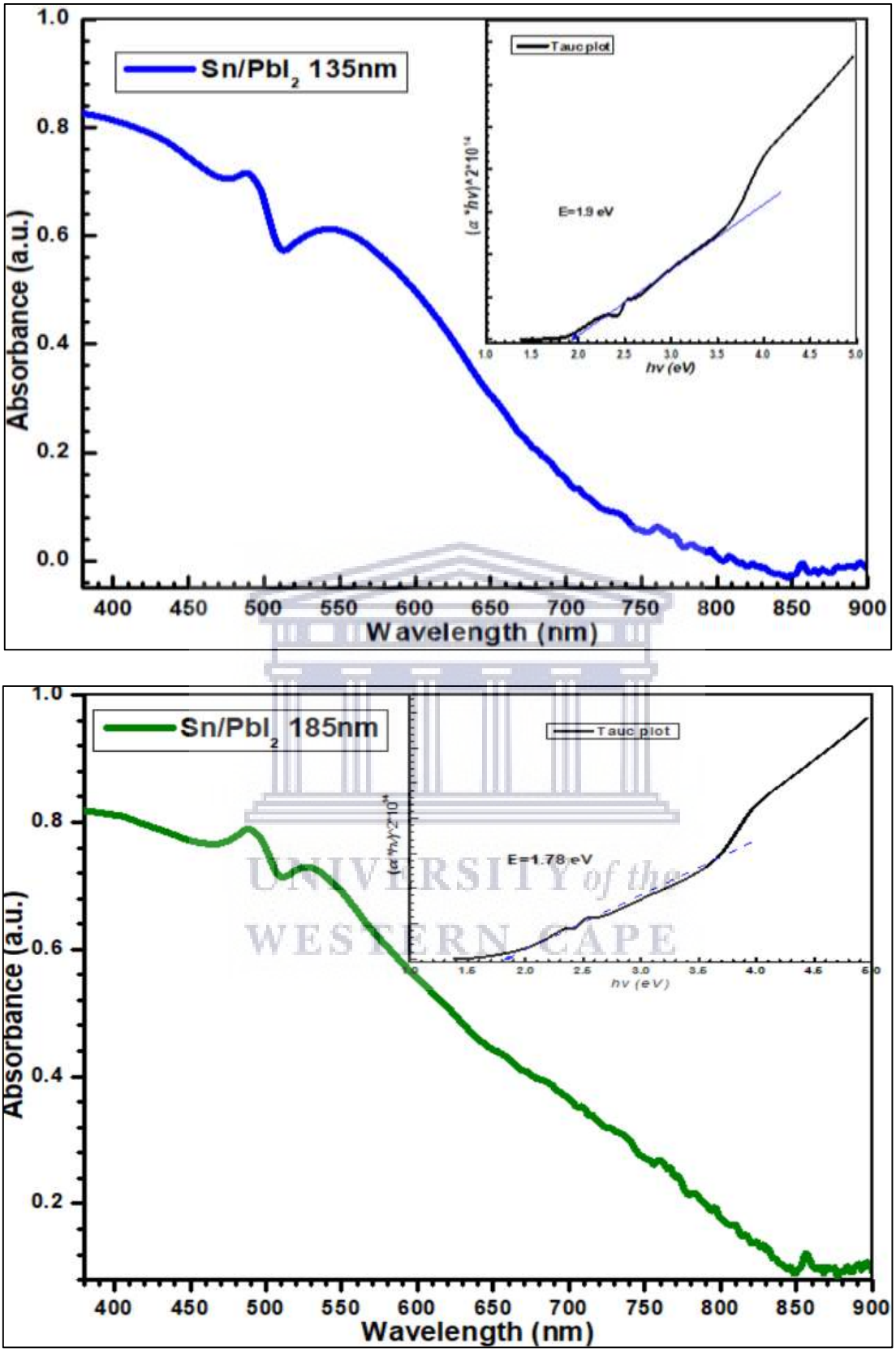

Figure 4. 10: Absorption spectra of PbI_2 and Sn- doped PbI_2 with different concentrations. And the Tauc plot for their respective band gaps, the variation of $(\alpha h\nu)^2$ versus hν, for pure PbI_2 and Sn-doped PbI_2 A1, A2, and A3 thin films.

PbI_2 is a compound with the energy bandgap of about 2.4 eV (Wang et al., 2017; Zhu et al., 2014), and during the deposition process, there may occur the formation of defects, such as voids and dangling bonds due to the presence of impurity concentration. As found in the XRD results, the grain size shrinking may give rise to localised states in the bandgap of the material. Furthermore, the incorporation of Sn^{2+} impurity helps to tie up the dangling bonds and thus effectively removing localised states in the bandgap of lead iodide, (see Fig4.10). Hence, the bandgap decreases with the increase of Sn dopant (20 nm, 35 nm, and 85 nm) as shown in Table 4.6. The thickness of PbI_2 was kept constant (at 100 nm).

Table 4.6: Band gap values of pure PbI_2 and Sn-alloyed PbI_2 (Sn: PbI_2)

Sample	PbI_2(100)	**A1** (120nm)	**A2** (135nm)	**A3** (185nm)
Eg (eV)	2.39	2.0	1.90	1.78

4.4 SECTION TWO: ANALYSIS OF THE CONVERTED PEROVSKITE AFTER EVAPORATION OF METHYL-AMMONIUM IODIDE

The perovskite film $\mathbf{CH_3NH_3Pb_{(1-x)}Sn_xI_3}$ (Eq.3) was formed as a result of a direct reaction between an (Sn-Pb)I_2 metal iodide and methylammonium iodide CH_3NH_3I inside a furnace under nitrogen atmosphere, *reaction:*

- $PbI_2 + CH_3NH_3I \rightarrow CH_3NH_3PbI_3$ (1)
- $Sn + 3CH_3NH_3I \rightarrow CH_3NH_3SnI_3 + 2CH_3NH_2 + H_2$ (Tavakoli et al., 2018b). (2)
- $Pb_{(1-x)}Sn_xI_2 + CH_3NH_3I \rightarrow CH_3NH_3Pb_{(1-x)}Sn_xI_3$ (3)

Again, as discussed in chapter three, the structure of these perovskites thin films can be characterized and confirmed by the X-ray diffraction technique. Measurements were taken using a 2θ range of 10˚ to 65˚, at an increment of 0.01 deg/step. Scanning electron microscopy was used to study the morphological properties of the grown perovskite film and EDS analysis was for the elemental composition of the grown samples. The optical properties of the perovskite thin films such as the absorbance capability and the bandgap were analysed by the UV-Vis between 400 to 900 nm.

4.4.1 X-RAY DIFFRACTION ANALYSIS OF PEROVSKITE FILMS

The XRD patterns of the perovskite samples (Pb-based, Sn-based, and Pb-Sn alloy S1, S2, S3) are shown in figure 4.11. The observed diffraction peaks at 14.11°, 24.52°, 28.43°, 31.89°, 38.5° 50.22°, and 52.35° were assigned to the (110), (202), (220), (310), (322), (404) and (431) planes of the tetragonal perovskite structure of Pb-based $CH_3NH_3PbI_3$. The assigned (110) and (220) peaks are indicative of the perovskite phase. Diffraction peaks are in good agreement with the previous reports (Alidaei et al., 2018; Tran et al., 2018). The unconverted PbI_2 peak can also be observed at 12.6° in the patterns of pure Pb-based see Fig 4.11. Its intensity should decrease when the amount of MAI is increased (Alidaei et al., 2018). Furthermore, in comparison with those previously reported in the literature, $CH_3NH_3SnI_3$ adopts the cubic structure, and the peaks are located at 14.1°,24.7°,28.6° corresponding to planes (100),(110),(111), respectively (Zhao et al., 2016; Takahashi et al., 2013).

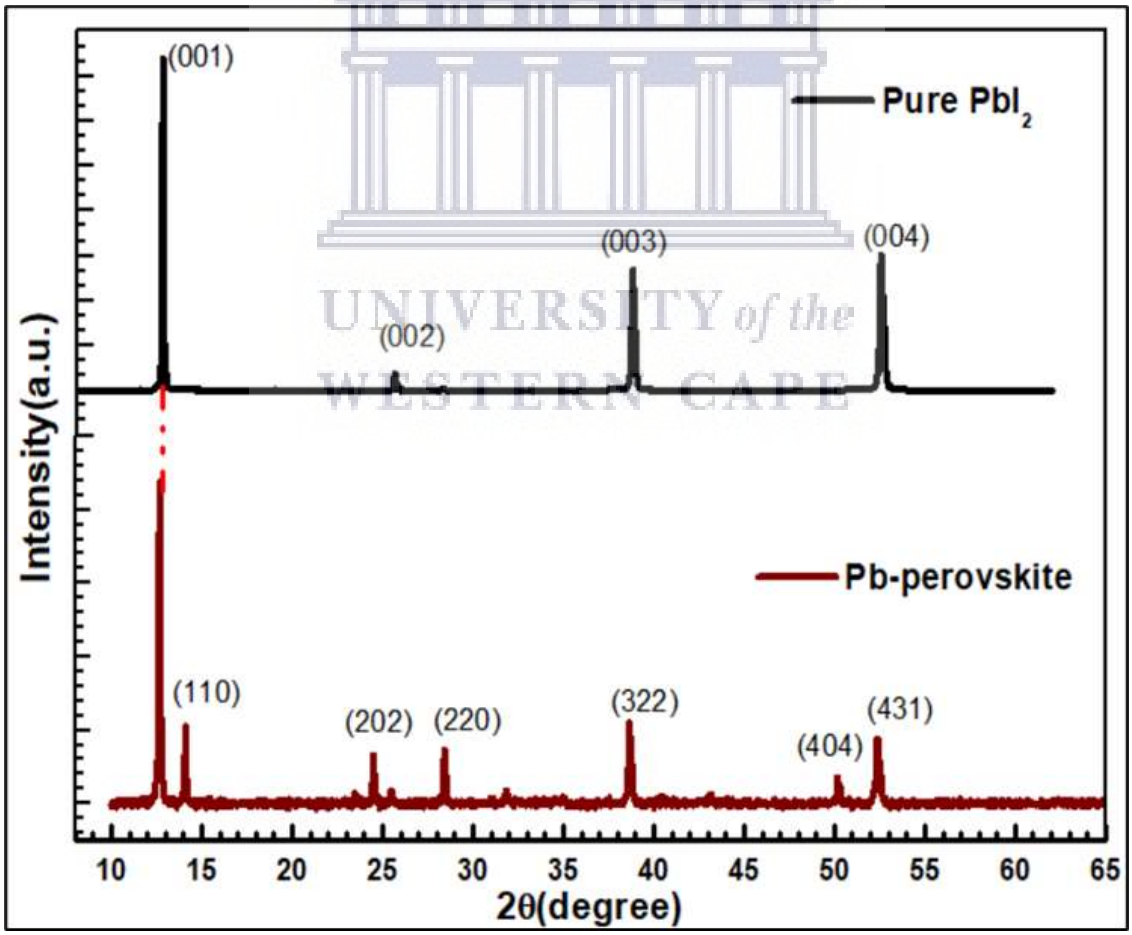

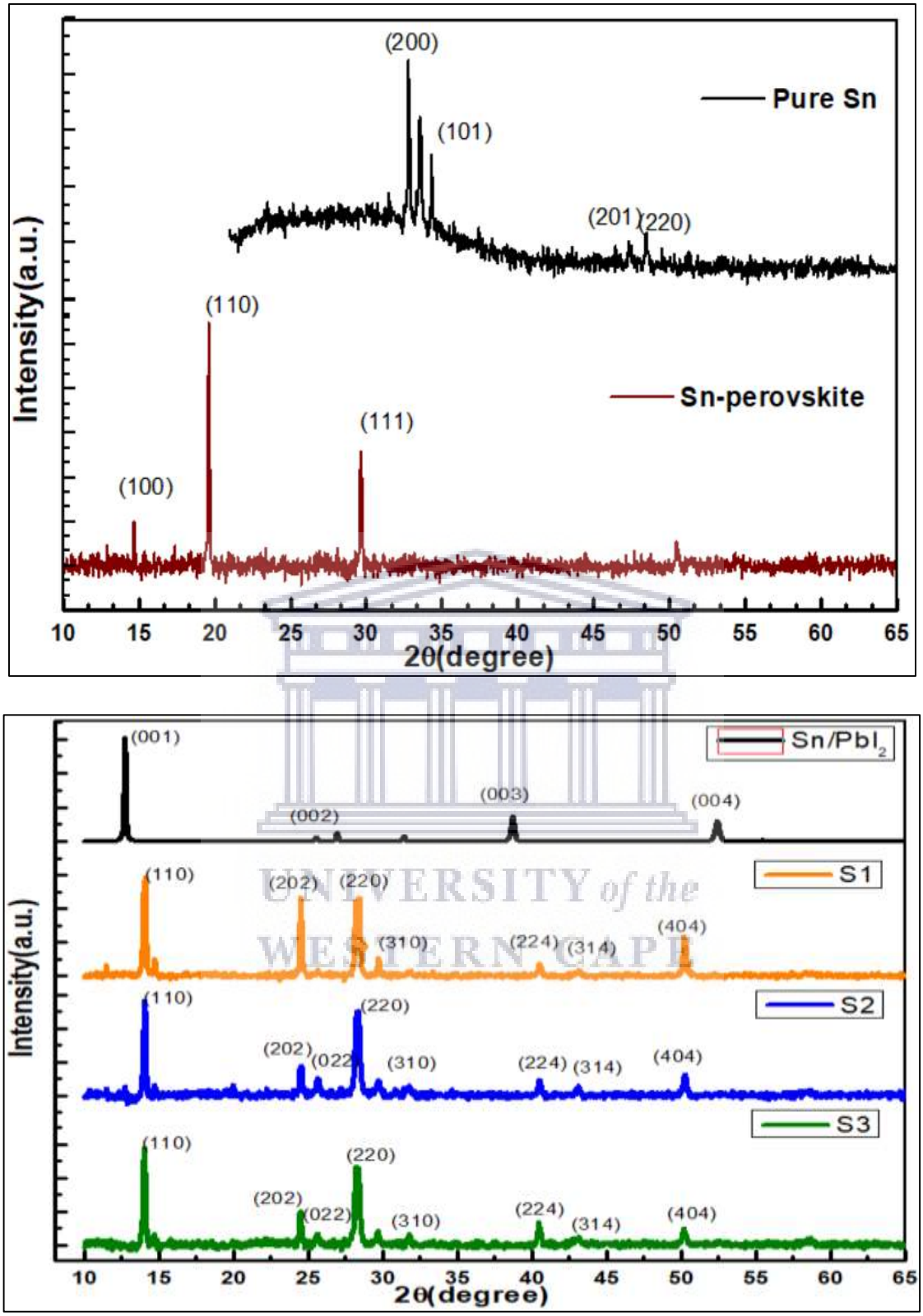

Figure 4. 11: X-ray diffraction patterns of PbI_2, Sn films, and their corresponding perovskite films formed from the reaction between metal precursor and MAI, (S1), (S2), and (S3) are Pb-Sn iodide alloy perovskite $CH_3NH_3Pb_{1-x}Sn_xI_3$ with different concentration of Sn.

However, the results from the literature suggest that the crystalline structure of $CH_3NH_3Pb_{(1-x)}Sn_xI_3$ perovskite would change from cubic to tetragonal when the ratio of Sn: Pb (or the parameter x) decreases from 1 to 0 (Nguyen-tran et al., 2018). In our Pb-Sn alloy perovskite samples (S1, S2, S3), the observed PbI_2 peak disappeared, which indicated that almost all the PbI_2 were converted to the $CH_3NH_3Pb_{(1-x)}Sn_xI_3$ perovskite (see Fig4.11). Thus, the alloyed perovskite $CH_3NH_3Pb_{(1-x)}Sn_xI_3$ shows X-ray diffraction patterns at 14.04, 24.52°, 25.65°, 28.34°, 40.51°, 43.13°, and 50.34 and can be indexed to (110), (202), (022), (220), (224), (314) and (440) crystal plane of perovskite, respectively, clearly observed for all $CH_3NH_3Pb_{(1-x)}Sn_xI_3$ compositions samples (Tavakoli et al., 2018a; Zhao et al., 2018). There are no critical differences in the XRD peaks between the alloy samples (S1, S2, S3), except for a slight shift in the positions of the peaks shown in Fig4.12. The peaks at 14.1°, 28.3°, and 43.13° are assigned to (110), (220), and (440) planes of $CH_3NH_3Pb_{(1-x)}Sn_xI_3$ perovskite layer which is in a good agreement with the literature (Tavakoli et al., 2018a). Additionally, the diffraction patterns display two peaks within the range between 22°−25° 2θ (x < 0.5), indexed to (202) and (022) planes confirming the tetragonal structure (I4cm space group), which gradually merge to a single peak (113) when the variable x becomes greater than half (x>0.5) (Zhao et al., 2017). The XRD data indicates a complete reaction of precursors during the CVD process. From the most intense (110) and (220) diffraction peaks, the average crystallite size of the layers(D) was estimated (tables 4.6) using the Sherrer equation (equation (1)):

$$D = \frac{k\lambda}{\beta_{hkl}\, cos\theta} \qquad Eq.4.6$$

Based on these equations the grain size and **d**–spacing, the lattice parameters, and unit cell volume of the perovskite layers were calculated using the (110) and (220) diffraction peaks:

$$n\lambda = 2dsin\theta \qquad Eq4.7$$

in which **n** is the order of diffraction, **λ** is the x-ray wavelength, **d** is the lattice inter-planar spacing of the crystal, and **θ** is the Bragg's angle:

$$\frac{1}{d_{hkl}^2} = \frac{h^2 + k^2}{a^2} + \frac{l^2}{c^2} \qquad Eq.4.8$$

$$V = a^2 \times c \qquad Eq.4.9$$

In equation (3), **h, k,** and **l** are the miller indices of the peaks, and a and c are the lattice parameters of the unit cell. The calculated results were summarized in Table 4.7.

Table 4.7: The calculated lattice parameters and unit cell volume for pure Pb-Sn alloy perovskite compared with Pb-based and Sn-based perovskite films.

Samples	**a=b (Å)**	**c (Å)**	**Cell volume V(Å)^3**	**Scherrer method D(nm)**	**Williamson-Hall method (UDM)**	
					D (nm)	***ε no unit x10^{-4}***
Pb-based	8.867	11.952	939.710	704	247	5.59
S3	8.861	11.918	935.791	882	51	9.64
S4	8.906	12.101	959.733	787	46	5.82
S5	8.886	12.100	954.138	1226	45	3.89
Sn-based	6.039	6.039	220.239	---	---	---

All the thin films with various Sn content have a tetragonal structure and leading to the conclusion that all compositions have similar crystal units. Table 4.7. exhibits the lattice parameter of perovskite and crystalline size. The lattice parameters of the alloy $CH_3NH_3Pb_{(1-x)}Sn_xI_3$ perovskite as a function of Sn content x, vary slightly. Since the crystal radii of Sn^{2+} (0.83 Å) are smaller than those of Pb^{2+} (1.33 Å) and I− (2.1Å). However, according to Vegard's law the lattice parameter, **a** and **c** are supposed to decrease with increasing Sn content x, for the relationship between them in the alloy is linear with the composition in the absence of strong electronic effects (Takahashi et al., 2013; Yuan et al., 2017). But, with the increasing of Sn content, the peaks slightly shift, causing a lattice distortion and the broadening of the full width at half maximum (FWHM) of (110) and (220) plane (see Fig.4.12). The Sn^{2+} at cation sites leads to the creation of cation vacancies. The creation of vacancies in the lattice might be responsible for the increase in the lattice parameters. Besides, the distortion in the lattice also affects the grain sizes. That probably explained the change in the crystal sizes, this means that we expanded the crystal size when incorporating Sn impurities. It was confirmed by the calculation of the crystal size which vary in the range from 700 nm to 900 nm for Debye-

Scherrer method and from 45nm-51nm for Williamson-Hall (UDM) method, at high content of Sn. Consequently, there is a correlation between the ionic radii, the grain size, and the shift of peak toward the small degree. The higher is the content of Sn, the further is the shift of the peaks and directed toward the smaller value of θ, therefore the smaller is the grain size, for the grain size is inversely proportional to the width of the peak. Noted that the W-H grain size value of Pb-perovskite is affected by the unconverted peak at 12.6 of pure PbI_2. The Fig.4.12 shows the **a** shift in the Bragg's angle of our different studied perovskite films.

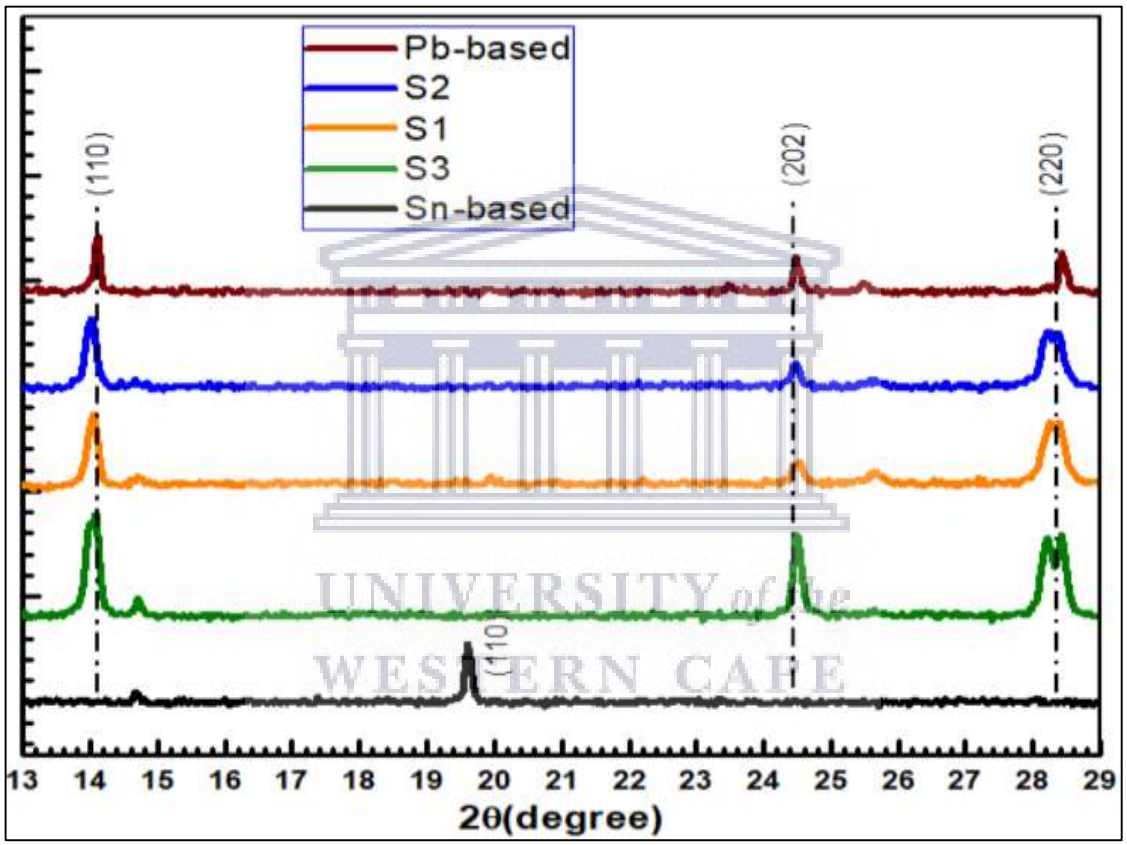

Figure 4. 12: X-ray diffraction patterns of $CH_3NH_3Pb_{1-x}Sn_xI_3$ perovskite films in the range of 13–29º showing (110), (202), and (220) plane.

4.4.2 MICROGRAPHS STUDY OF THE CONVERSION PEROVSKITE

To study the micrographs of perovskite thin films, scanning electron microscopy (SEM) analysis was used. The surface morphologies of theses perovskites film are highly uniform and completely covers the substrate. The Pb-based, Sn-based and the Pb-Sn alloy-based perovskites thin films show highly reflective surfaces, a representative photo of which is shown in Fig 4.13.

The top-view SEM images of Pb and Sn-based perovskite thin-film show densely packed grains over a large area, as seen in Fig. 4.13 (a) and (b). No apparent pinholes are observed in the films (a) and (b). However, the as-deposited films exhibited hierarchical morphology showing island formation with large grain size and pinholes. But the annealing of the film improved the coverage of the Pb-Sn alloy-based perovskite films and breaking grains in small ones (see Fig.4.13 d–f).

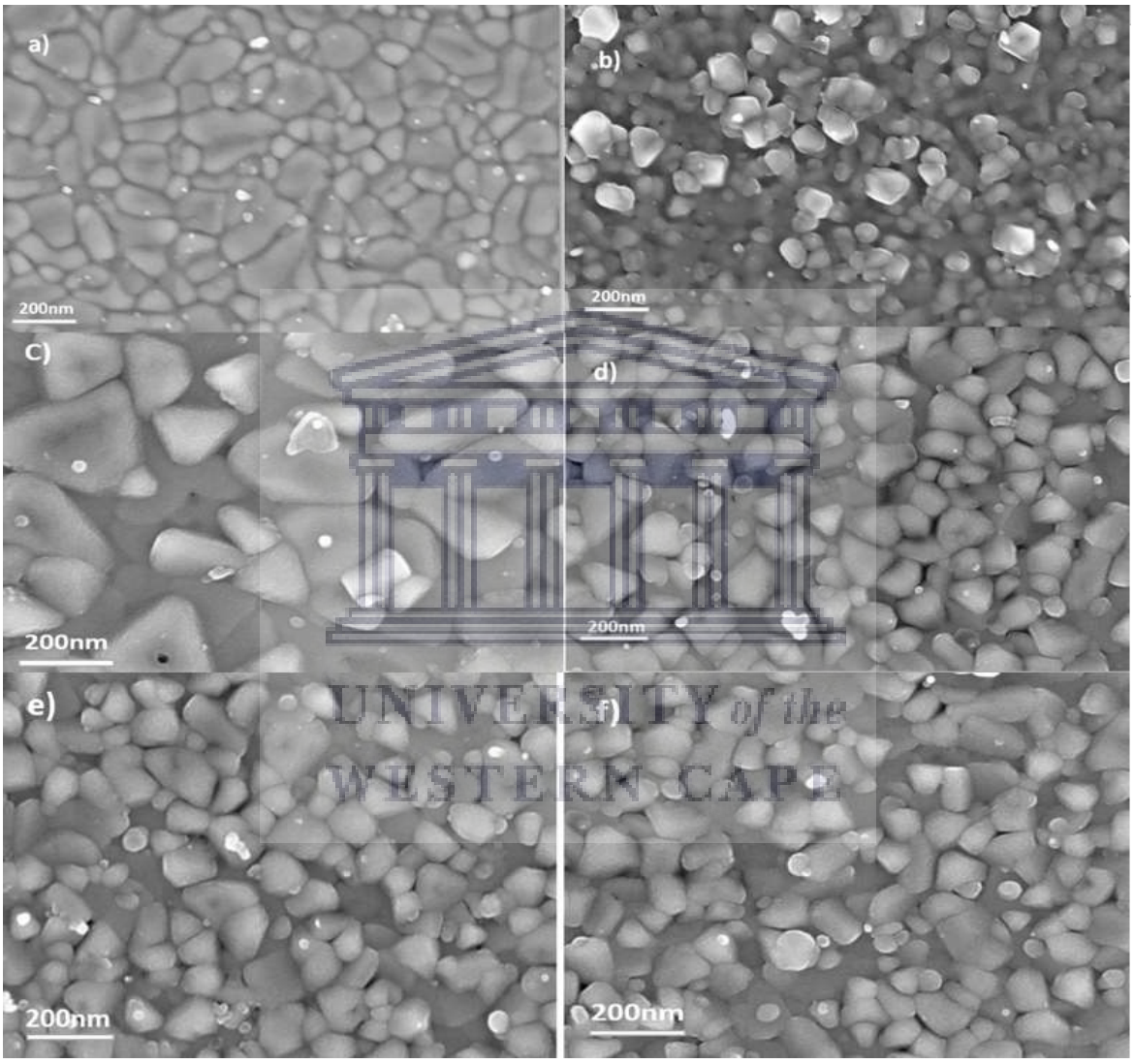

Figure 4. 13: Micrographs of perovskite layer on glass substrates: (a) Pb-based, (b) Sn-based and (c) Pb-Sn alloy-based as-deposited and (d), (e) (f) alloy-based formed after annealing of (PbI_2 -Sn) with different concentration of Sn.

Moreover, from top view SEM images (see Fig.4.13 d–f), it can be observed that crystalline of Pb-Sn alloy-based grains is packed forming continuous films, presenting no degradation at room temperature. This proves that the prior annealing of the metal Pb-Sn iodide affects the

material as studied previously. The images in Fig.4.13 of (d), (e), and (f) show the typical top-view SEM images of the alloy perovskite films fabricated with different thicknesses. There is no apparent difference between them. Quantitative EDS analysis was performed on Pb-Sn perovskite on a glass substrate to determine the chemical composition of the films as observed in Fig 4.14. The EDS spectrum obtained indicates signals for I, Pb, Sn, and C.

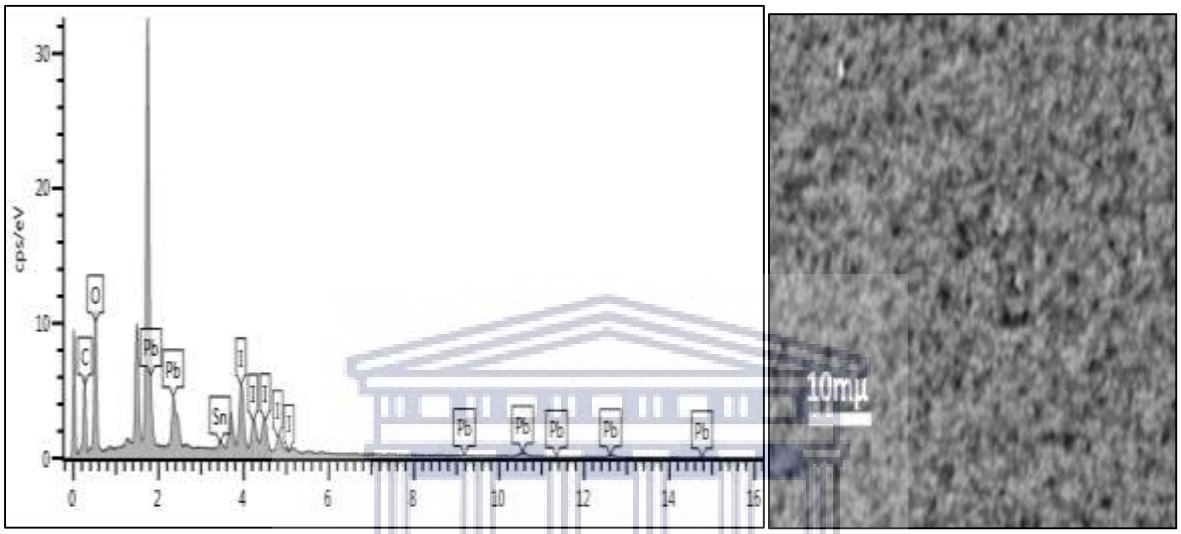

Figure 4. 14: EDS spectrum of Pb-Sn alloyed perovskite on a glass substrate.

The data show predominantly elements I, C for our deposited material with a weight percentage of 76.5 % and 22.3 % respectively, see Table 4.8. However, an additional signal of oxygen (O) is also observed. The O signal is due to the oxidation of the sample, which is generally caused by moisture and affects most perovskite materials (Zhao D. et al., 2016)**.** A high weight percentage of carbon (C) is certainly due to an additional carbon that is added before the insertion into the SEM as it is a requirement that a sample to be analysed must be conductive. Furthermore, the atomic percentage from Table 4.8 gives the ratio **Pb/Sn** close to **0.56:0.44** and **0.62:0.38** spectrum 1 and 2 respectively, suggesting the formation of $\mathbf{CH_3NH_3Pb_{0.56}Sn_{0.44}I_3}$ and $\mathbf{CH_3NH_3Pb_{0.62}Sn_{0.38}I_3}$**.** The H and N signals did not appear, either because the system is not sensitive, or the elements evaporated by the time of the analysis.

Table 4.8: Elemental composition Pb-Sn alloyed perovskite S1 on a glass substrate

Elements	Atomic (. %)		Weight (. %)	
	Spectrum 1	Spectrum 2	Spectrum 1	Spectrum 2
Pb	1.45	1.57	12.37	13.33
Sn	1.12	0.97	5.49	4.7
I	5.69	5.66	29.69	29.45
O	43.68	44.72	28.72	29.33
C	48.06	47.09	23.73	23.19
Total	100	100	100	100

4.4.3 UV-VIS ANALYSIS of PEROVSKITE FILMS

To study the optical properties of the graph displayed in Fig4,15 of Pb-based, Sn-based, and Pb-Sn alloy-based $CH_3NH_3(Pb_xSn_{1-x})I_3$ $[0 \leq x \leq 1]$ perovskite thin films, UV-vis analysis was conducted by measuring the absorbance capacity as shown in Figure 4.15.

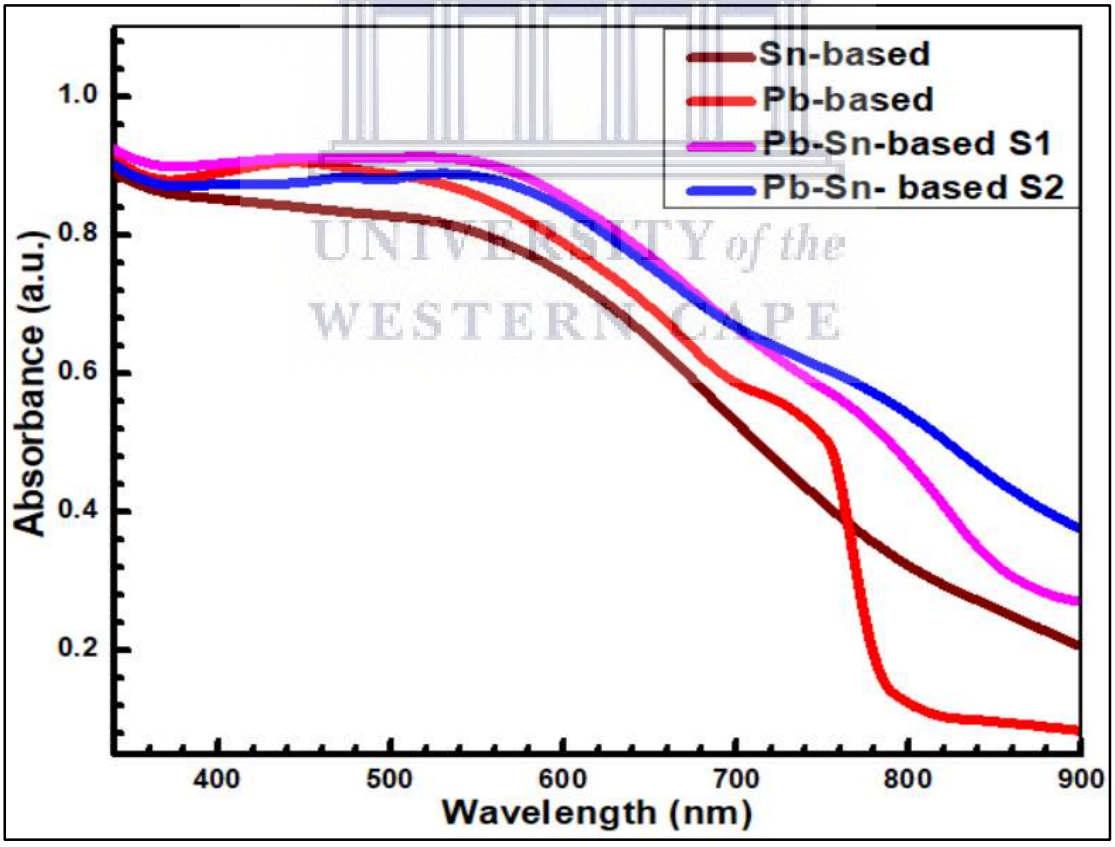

Figure 4. 15: UV-vis absorption spectrum of Sn-based $CH_3NH_3Sn_xI_3$, Pb-based $CH_3NH_3PbI_3$, and Pb-Sn alloy based $CH_3NH_3Pb_{(1-x)}Sn_xI_3$ perovskite S1 and S2 films.

We compared the absorbance of Pb-based, Sn-based, and both Pb-Sn alloy perovskite S1 and S2. The perovskite film absorbs throughout the visible range with a sharp reduction at about 750 nm for Pb-based perovskite. The Sn-based perovskite in comparison goes beyond 900nm, which further illustrates the decrease in the bandgap. The wide absorption confirms the high quality of vapor grown perovskite films. With the incorporation of Sn-dopant, it shows that the absorption edge shifts towards the higher-wavelength side comparative to Pb-based (Fig.4.15) and becomes broader for higher-doping levels of Sn in the alloyed perovskite. More importantly, the absorption is greatly enhanced from 600 nm to 800 nm, demonstrating the binary-metal system's potential for expanding the light-harvesting capacity of current perovskites. Similar results were given by previous researches namely Fan Zuo et al., Mohammad M. Tavakoli, Yuhei Ogomi, etc (Ogomi et al., 2014; Tavakoli et al., 2018a; Zhao et al., 2017b, 2018b; Zuo et al., 2014). It can be observed in Figure 4.16 that the bandgap bows as we substitute Sn^{2+} in place of Pb^{2+} (until 40% Sn^{2+} ions are replaced by Pb^{2+}) and results in a non-monotonic bandgap lowering similar to what was observed by Hao et al.(Zhao et al., 2018b). Briefly, the bandgap of the 60% and 80% Sn content films may exhibit a lower bandgap than the 100% Sn-substituted films (Zhao et al., 2017b). Too much of Sn content is detrimental to the absorption capacity. A similar trend was confirmed in the PL spectra by Baodan Zhao et al.(Zhao et al., 2017b) where the PL spectra of 80% and 60% Sn content thin-film samples are red-shifted compared to the 100% Sn content thin film sample, which is consistent with the absorption spectra. These anomalous bandgaps abasement and lack of conformity with Vegard's law (Tavakoli et al., 2018a; Zhao et al., 2017b) are due to competition in the perovskite lattice between the spin-orbit coupling of Pb and Sn ions. The alteration in their ion radii causes distortions of the lattice that affect the band gap depending on the mixed-phase composition (Tavakoli et al., 2018b; Zhao et al., 2018b). The bandgap decreases with increasing-doping concentration (Table 4.9).

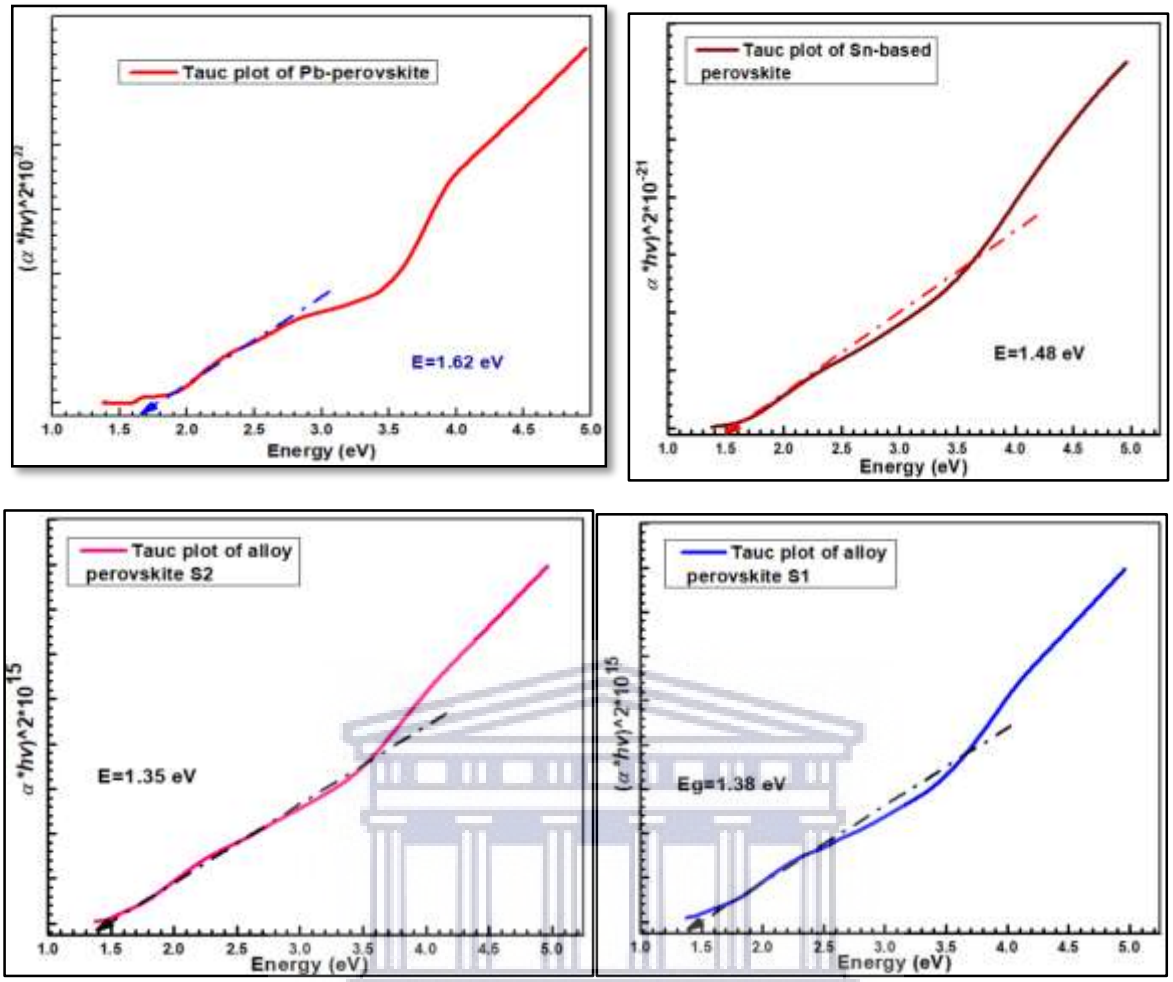

Figure 4. 16: Shows the variation of $(\alpha h\nu)^2$ versus hν, for Pb-based, Sn-based, and Pb-Sn alloy perovskite thin films.

Table 4.9: Energy bang of the characterized samples

Samples	Pb-perovskite	Sn-perovskite	Pb-Sn perovskite S2	Pb-Sn perovskite S1
Band gap (eV)	1.6	1.48	1.35	1.38

4.5 REFERENCES

Alidaei, M., Izadifard, M., Ghazi, M.E., Ahmadi, V., 2018. Materials Research Express 5 (1), 016412.

Bhavsar, D.S., Saraf, K.B., 2003. Materials Chemistry and Physics 78, 630–636.

Chen, K., Schu, S., 2018. Chem. Soc. Rev. 47, 7045–7077.

Cho, S., Yu, J., Kang, S.K., Shih, D.Y., 2005. J. Electron. Mater. 34, 635–642.

Demeulemeester, J., Smeets, D., Comrie, C.M., Bockstael, C. Van, Knaepen, W., Detavernier, C., Temst, K., Vantomme, A., 2010. Journal of Applied Physics 108, 043505.

Mote, V.D., Purushotham, Y., Dole, B.N., 2012. J Theor Appl Phys 6, 6.

Yousefi, R., Sheini, F.J., Saaedi, A., Cheraghizade, M., 2015. Sains Malaysiana 44, 291–294.

Nguyen-tran, T., Mai, N., Duyen, K., Duyen, T., 2018. J. Sci. Adv. Mater. Devices 3, 471–477.

Ogomi, Y., Morita, A., Tsukamoto, S., Saitho, T., Fujikawa, N., Shen, Q., Toyoda, T., Yoshino, K., Pandey, S.S., Ma, T., Hayase, S., 2014. J. Phys. Chem. Lett. 5, 1004–1011.

Zhao, D., Meng, W., Wang, C., Liao, W., Cimaroli, A., Zhu, K., Yan, Y., 2016. RSC Adv. 6, 90248-90254.

Sahu, D., Panda, N.R., Acharya, B.S., Panda, A.K., 2014. Opt. Mater. (Amst). 36, 1402–1407.

Saliba, M., Matsui, T., Seo, J., K.D.-E.&, 2016. Energy Environ. Sci. 9, 1989-1997

Shao, S., Liu, J., Portale, G., Fang, H., Blake, G.R., Brink, G.H., Koster, L.J.A., Loi, M.A., 2018. Advanced Energy Materials 8,1702019.

Soussi, L., Garmim, T., Karzazi, 2020. Surfaces and Interfaces 19, 100467

Takahashi, Yukari, Hasegawa, H., Takahashi, Yukihiro, Inabe, T., 2013. J. Solid State Chem. 205, 39–43.

Tavakoli, M.M., Zakeeruddin, S.M., Grätzel, M., Fan, Z., 2018. Adv. Mater. 30, 1–9.

Tran, V.D., Pammi, S.V.N., Dao, V.D., Choi, H.S., Yoon, S.G., 2018. J. Alloys Compd. 747, 703–711.

Wang, Y., Gan, L., Chen, J., Yang, R., Zhai, T., 2017. Sci. Bull. 62, 1654–1662.

Xiao, M., Gu, S., Zhu, P., Tang, M., Zhu, W., Lin, R., Chen, C., Xu, W., Yu, T., Zhu, J., 2018. Adv. Opt. Mater. 6, 1700615.

Yang, W.S., Noh, J.H., Jeon, N.J., Kim, Y.C., Ryu, S., Seo, J., Seok, S. Il, 2015. Science 348, 1234-1237.

Yuan, J., Li, B., Hao, C., 2017. Materials Science in Semiconductor Processing 57, 95-98.

Zak, A.K., Majid, W.H.A., Abrishami, M.E., Youse, R., 2011. Solid State Sciences 13, 251-256.

Zhao, B., Abdi-Jalebi, M., Tabachnyk, M., Glass, H., Kamboj, V.S., Nie, W., Pearson, A.J., Puttisong, Y., Gödel, K.C., Beere, H.E., Ritchie, D.A., Mohite, A.D., Dutton, S.E., Friend,

R.H., Sadhanala, A., 2017. Adv. Mater. 29, 1604744.

Zhao, J., Wei, L., Jia, C., Tang, H., Su, X., Ou, Y., Liu, Z., Wang, C., Zhao, X., Jin, H., Wang, P., Yu, G., Zhang, G., Liu, J., 2018a. J. Mater. Chem. A 6, 20224-20232.

Zhu, X., Sun, H., Yang, D., 2014. J Mater Sci: Mater Electron 25, 3337–3343.

Zhu, X., Zhang, H., Yang, D., Wei, Z., Gao, X., Yang, J., 2010. J. Alloys Compd. 505, 34–36.

Zuo, F., Williams, S.T., Liang, P.W., Chueh, C.C., Liao, C.Y., Jen, A.K.Y., 2014. Adv. Mater. 26, 6454–6460.

CHAPTER 5

CONCLUSIONS AND OUTLOOK

5.1 CONCLUSION

The goal of this thesis is to minimize lead content in perovskite—$CH_3NH_3Pb_{1-x}Sn_xI_3$, through the investigation and understanding of the photo-physical mechanisms of the organic-inorganic perovskite materials, including the effects of photo-activated ion motion. The synthesis of the organic-inorganic perovskite was successfully conducted by the thermal chemical vapour deposition (TCVD) system. The optimization of the system was done by exploring the effects of several deposition parameters on the growth, morphology, and structural properties of the grown materials.

All these experiments were based on spectral UV-vis techniques, analysing the absorption capability as well as the RBS investigation on the diffusion between Sn and PbI_2. The absorption spectrum was used to evaluate the absorption coefficient and calculate the bang gap. And real-time RBS spectrum was analysed to evaluate the occurrence of the diffusion. Other complementary characterization techniques, such as Scan Electron Microscope (SEM), Xray diffraction (XRD), and Energy Scattering Spectroscopy (EDS), were also used to facilitate the analysis and the discussion of the results. To establish a comprehensive system for the study, two step-depositions were conducted. First, from the precursor PbI_2, a thin film of pure Sn was subsequently added to form a lead-tin binary iodide alloy—$Pb_{1-x}Sn_xI_2$, while reducing incrementally lead content. Secondly, it was followed by the evaporation of MAI (CH_3NH_3I) to form $CH_3NH_3Pb_{1-x}Sn_xI_3$ perovskite. The $CH_3NH_3PbI_3$ and $CH_3NH_3SnI_3$ samples with the incorporation of a single metals Pb/Sn were also prepared. The characteristics of perovskites depend heavily on their composition and structure. It is, therefore, necessary, to study different kinds of perovskite materials. We primarily decided to investigate the metal alloy iodide, which is the foundation of this perovskite. The results of the study are as follows:

PbI_2: Sn alloy films were synthesized by thermal evaporation route and the characteristic properties were studied. To confirm the presence of Sn ions, more investigations like RBS and

EDS spectroscopy are carried out and its signature is recorded. XRD result shows the evolution of the $PbSnI_2$ phase with Sn doping in the XRD pattern of PbI_2. The absorbance capability is evaluated by UV-vis spectroscopy. The obtained results indicated that $PbSnI_2$ thin films were successfully synthesized using thermal evaporation. The study of the effect of temperature which was measured by real time RBS showed that the ideal annealing temperature for $PbSnI_2$ in our system was between 200-220 ℃ in the presence of nitrogen. RBS and EDS evaluated the composition Pb: Sn, a balanced ratio which is necessary to obtain a photo-response characteristic of a metal iodide needed. SEM revealed the crystallinity change from pure PbI_2 to $PbSnI_2$. Moreover, the incorporation of Sn ions leads to a slight expansion in PbI_2 lattice, yet with a decrease in average crystallite size and bond length with the increase in Sn content. The crystal phase analysis also revealed that PbI_2: Sn alloy films crystallized in a hexagonal structure, which was evaluated by XRD. Subsequently, the absorbance spectrum of PbI_2: Sn thin films show high absorption of UV light, as well as a sharp band around 500 nm in the UV-Vis spectra. Thus, decreasing the band gaps of the alloyed samples determined from Tauc's model equation, which is confirmed with other researchers.

Then, it proceeded with the investigation of the converted perovskite films after the evaporation of CH_3NH_3I. As the second step, perovskite films were formed by applying again, a TCVD process under a nitrogen atmosphere. The morphology, composition, the internal structure (crystallography), and optical properties were characterized using several techniques including XRD, SEM, EDS, and UV-VIS. The results of the study are as follows:

The change in XRD patterns from a hexagonal (PbI_2, and $Pb_{(1-x)}Sn_xI_2$) to a tetragonal structure and a cubic (pure Sn) structure, is convincing evidence for the existence of a converted perovskite. As per Pb-Sn alloy, the results showed the absence of peaks at 12.6°, characteristic of $PbSnI_2$-- now located at 14.1°, is an achievement for this new route of synthesizing a less toxic perovskite. Moreover, the peaks located at 14.1°, 28.3°, and 43.13° assigned to (110), (220), and (440) planes obtained from $CH_3NH_3Pb_{(1-x)}Sn_xI_3$ perovskite samples are in a good agreement with the literature. In addition, the optical studies confirmed the potential of a binary-metal system to expand the light-harvesting capacity of the current perovskites. As a result, the incorporation of Sn-dopant shows that the absorption edge shifts towards the higher-wavelength and becomes broader for higher-doping levels of Sn compared to pure (Pb or Sn) perovskites.

In summary, we have successfully managed to dope PbI_2 with Sn. The compound $Pb_{(1-x)}Sn_xI_2$ obtained serves as a scaffold for perovskite. Then we have demonstrated the exchange of the B-site metal cation in iodide perovskite thin films and nanocrystals, converting between Sn- and Pb-based perovskites. We observed the formation of crystalline alloys rather than bilayer or phase-segregated regions. This process helps to control the amount of metal (Pb or Sn) needed and minimize the toxicity. It also points to new opportunities for controlling composition as a synthetic process, detached from the complex processes of crystallization, and could enable more precise control over solution processing. By conducting a systematic study on the optical absorption, we have explored the ways through which the photovoltaic performance of Pb and Sn-Pb binary perovskite solar cells can be improved.

5.2 FUTURE WORK

The work presented in this thesis from the optical measurements that allowed quantitative analysis of the photo-induced carrier dynamics in the perovskite system. It shows the evidence of absorption capability in perovskite. Further photo-induced instability research will be focused on two aspects: (1) the study of ionic dynamics includes physical parameters (conductivity, diffusion coefficient, etc) and the interaction with phonons; (2) study of solar cell performance and the influence of carrier dynamics.